PREDICTION AND MEASUREMENT OF

HEAT TRANSFER RATES FOR THE SHOCK-INDUCED UNSTEADY LAMINAR BOUNDARY LAYER

ON A FLAT PLATE

By

WILLIAM J. COOK, ASSOCIATE PROFESSOR

DEPARTMENT OF MECHANICAL ENGINEERING

AND THE ENGINEERING RESEARCH INSTITUTE

IOWA STATE UNIVERSITY

AMES, IOWA

OCTOBER, 1972

FOREWORD

SUMMARY

The unsteady laminar boundary layer induced by the flow-initiating shock wave passing over a flat plate mounted in a shock tube is theoretically and experimentally studied in terms of heat transfer rates to the plate for shock speeds ranging from 1.695 to 7.34 km/sec. The theory presented by Cook and Chapman for the shock-induced unsteady boundary layer on a plate is reviewed with emphasis on unsteady heat transfer. A method of measuring time-dependent heat-transfer rates using thin-film heat-flux gages and an associated data reduction technique are outlined in detail. Particular consideration is given to heat-flux measurement in short-duration ionized shock-tube flows. Experimental unsteady plate heat transfer rates obtained in both air and nitrogen using thin-film heat-flux gages generally agree well with theoretical predictions However, some difficulties were encountered in resolving time dependent heat transfer rates for very early times after shock wave arrival at the gages. The experimental results indicate that the theory continues to predict the unsteady boundary layer behavior after the shock wave leaves the trailing edge of the plate even though the theory is strictly applicable only for the time interval in which the shock remains on the plate. In addition, the experimental results confirm that under certain conditions steady flow can readily be attained over models in short-duration shock-tube flows.

TABLE OF CONTENTS

SYMBOLS

A   Shock strength parameter, $(\rho_o/\rho_1)/((\rho_o/\rho_1) - 1) = U_s/u_o$

a   speed of sound

C $\rho\mu/\rho_o\mu_o$

c   specific heat

cf   correction factor in Eq. (59)

E_o initial voltage drop across thin-film heat flux gage

ΔE_F time dependent voltage change across thin-film heat flux gage

h   enthalpy

H   dimensionless enthalpy, $(h - h_o)/h_o$

I_o electrical current in thin film ballast circuit

k   thermal conductivity

L   plate length, Fig. 1a

M_s shock Mach number, U_s/a_1

P   pressure

q   heat transfer rate per unit area, (heat flux)

q_n numerically computed heat flux, Eq. (61)

q_v heat flux computed using variable substrate properties, Fig. 11

Q   heat transfer variable given by Eqs. (25) and (52)

Q_x heat transfer variable for fixed x view point, Eq. (53)

R   gas constant, Eq. (62), also electrical resistance

Re   free-stream Reynolds number, $\rho_o u_o x/\mu_o$

R_M ratio, Fig. 4, defined by Eq. (55)

R_{ss} ratio, Fig. 4, defined by Eq. (54).

R_B resistance of ballast resistor, Fig. 6

ΔR_F change in thin film resistance

R_o initial resistance of thin film

t	time, t = 0 when shock wave arrives at plate leading edge; also general time in section on Heat Flux Measurement
t'	time, t' = 0 when shock wave arrives at thin film heat flux gage
T	temperature change $\theta - \theta_1$; also absolute temperature when subscripted as T_1
u	velocity in the x direction
U_s	shock speed
v	velocity in the y direction
W	width of thin film element, Fig. 6
x	distance from plate leading edge
x'	distance measured from the shock, Fig. 2(c)
x_g	gage position, Fig. 12
y	distance perpendicular to plate surface
y'	distance perpendicular to wall, Fig. 2(c)
α	dimensionless distance-time variable, $x/u_o t$
α_C	thermal diffusivity of coating material
α_F	thermal diffusivity of film
β	dimensionless velocity, u/u_o
β^*	dimensionless velocity expression, Eq. (14)
γ	dimensionless time $u_o^2 t/\nu$; also a Reynolds number based on $x = u_o t$
Γ	resistance-temperature parameter, $\Delta R / \Delta\theta R_o$
δ_C	coating thickness, Fig. 6
δ_F	film thickness, Fig. 6
η	general x in Eqs. (6), (7), and (8)
θ	absolute temperature
$\bar{\theta}$	$\alpha_F t/ \delta_F^2$, Fig. 7
μ	coefficient of viscosity
ν	coefficient of kinematic viscosity, μ /ρ

ρ density

σ effective Prandtl number

τ dimensionless shear stress $\mu(\partial u/\partial y)/\rho_o u_o^2$

τ^* shear stress, $\mu(\partial u/\partial y)$

Φ $\int_0^{T(0,t)} (k/k_p)\,dT$

ϕ shear stress variable, Eqs. (17) and (44)

ψ $\sqrt{(k\rho c)_s/(k\rho c)_F}$, Fig. 7

ω plate leading edge angle, Fig. 12

Subscripts

o   free stream conditions relative to the plate

1   conditions in stationary gas ahead of shock wave

2   conditions behind shock in Fig. 2(b)

∞ free stream conditions in Figs. 2(a) and 2(c); also surface condition in heat transfer measurement section

c   heat flux computed from corrected gage response, Fig. 9(b)

F   film

gr   heat flux computed from uncorrected gage response, Fig. 9(b)

I   interface between film (or coating) and substrate; also summation index, Eq. (61)

L   the condition $U_s t = L$

m   number of time intervals, Eq. (61)

M   M region

Msf   M region in shock-fixed coordinates

p   constant substrate properties

s   substrate

ss   steady state

w   quantity evaluated at the wall

INTRODUCTION

Shock tubes have been developed that have the capability of driving flow-initiating shock waves at speeds in the neighborhood of 10 km/sec. The high-temperature high-speed flow behind the incident shock is of interest in a number of areas. Experimental studies in many of these areas are influenced by or are involved with the boundary layers induced by the shock wave on either the shock tube side wall or on models or test apparatus such as splitter plates placed in the flow. A difficulty encountered in shock tube testing, however, is the short duration of the high temperature flow. This is especially pronounced at high shock speeds. In view of the short testing times available, an important consideration is the transient development of the shock-induced boundary layers since, in cases where steady-state boundary layers might be desired, the testing time may be insufficient for steady state conditions to be reached.

An unsteady shock-induced boundary layer of considerable interest is that developed on a flat plate with a sharp leading edge mounted with zero angle of attack in a shock tube. The present study is concerned with this boundary layer. Considerations here are restricted to laminar boundary layer flow. The development of the laminar boundary layer on the plate has been the subject of several investigations, the most recent one being that of Cook and Chapman[1] in which a complete theoretical description of the unsteady boundary layer is presented for shock speeds ranging to 9 km/sec. However, experimental vertification of the theory is lacking for a large part of the range of shock speeds considered. The present investigation was initiated for the purpose of experimentally verifying the theory of Ref. 1. A quantity associated with the transient nature of the boundary layer that can be measured is the plate surface heat flux. As a result,

this investigation   focuses primarily on experimental verification of
theoretically predicted heat transfer rates for the unsteady laminar flat plate
boundary layer.   The experiments reported here cover shock speeds ranging
from 1.695 to 7.34 km/sec and were performed using air and nitrogen as the
test gas.

THEORY OF THE UNSTEADY SHOCK INDUCED LAMINAR BOUNDARY LAYER ON A FLAT PLATE

In view of the complexity of the theoretical analysis of the shock induced unsteady laminar boundary layer on a flat plate, the theory presented in previous papers on this subject will be summarized here in some detail. Lam and Crocco[2-4] originated the study of the shock induced boundary layer on a flat plate. Felderman[5,6] extended the work of Lam and Crocco by obtaining an extended range of theoretical solutions to the governing equations to predict unsteady heat transfer rates to the flat plate. He also experimentally verified the theory for a range of relatively low speed flows. More recently the basic approach of Lam and Crocco was used by Cook and Chapman[1] in the study of laminar boundary layers induced by shocks with speeds ranging from 1.12 to 9 km/sec. A complete description of the boundary layer development is presented for this range of shock speeds for equilibrium air at a pressure of one atmosphere behind the shock. Results describe the unsteady nature of the boundary layer in terms of friction coefficients, heat transfer quantities, and velocity, displacement, and momentum thicknesses as a function of a single position-time variable. The following sections present a review of the considerations that served as the basis for the analysis presented in Ref. 1.

Boundary Layer Description

The boundary layer of interest is that shown schematically in Fig. 1(a). The shock wave is assumed to propagate into region 1 with constant velocity U_s. At zero time the shock is at the leading edge of the stationary plate and by time t the shock wave has traveled a distance $U_s t$ in the positive x direction, and an unsteady boundary layer has developed on the plate between the leading edge and the shock. The free-stream velocity behind the shock relative to the plate is u_o, and in time t the free-stream fluid particles initially over the plate leading edge have moved a distance $x = u_o t$. The region between $U_s t$ and $u_o t$ contains only fluid particles that initially occupied positions downstream of the leading edge. Thus the boundary layer developed in this region (denoted as the M region) is identical to that induced by the moving shock on the shock tube side wall since the plate leading edge does not influence M region particles. Near the leading edge of the plate the boundary layer is that for steady flow over the plate. As will be seen, these two regions play an important role in the solution of the governing boundary layer equations.

A key factor in the physical interpretation of the boundary layer development and the solution of the governing equations is selection of a coordinate system in which to view the problem. The variables of Lam and Crocco[2-4] form a "natural" set of independent variables that readily permits interpretation of certain important features of the problem. First, a transformation is made to change from the variables of Fig. 1(a), (x,y,t), to (x,u,t) where u is the x component of velocity. Next, dimensionless variables are defined as $\alpha = x/u_o t$, $\beta = u/u_o$, and $\gamma = u_o^2 t/\nu_o$, where ν_o is the kinematic viscosity. An interpretation of the problem in terms of these variables is presented in Fig. 1(b). $\beta = 0$ and $\beta = 1$ correspond to the wall and

free-stream respectively. The region of interest on the α axis ranges

from zero to A. $\alpha = U_s t/u_o$ $= U_s/u_o$ = A defines the shock position. The

region $1 \leq \alpha \leq$ A, $\gamma > 0$, is the M region and $\alpha = 1$ delineates the dividing

line in the free-stream that separates the fluid particles initially upstream

and downstream of the leading edge. The region $0 \leq \alpha \leq 1$, $0 \leq \beta \leq 1$, $\gamma > 0$,

is denoted as the interaction region after Lam[2]. Small values of α correspond

to steady state conditions. This can be seen by considering the problem

from two points of view. For any fixed x position, increasing time corresponds

to decreasing values of α and approach to the steady state condition for

that x. $\alpha = 0$ corresponds to infinite time. Alternately, when time is

fixed and small values of x compared to $u_o t$ are considered (i.e., at small α),

steady state would be expected. Thus the dual role of the α variable

becomes evident. As noted schematically in Fig. 1(b), the region of interest

in α, β, γ space is $0 \leq \beta \leq 1$, $0 \leq \alpha \leq$ A, $\gamma > 0$. Prior to considering

the governing equations for the unsteady problem, solutions for the bounding

M and steady state regions will be discussed.

Solution of the Steady State and M Region Boundary Layer Equations

A unique similarity exists between the steady flat plate boundary layer

and that for the M region when the M region is considered in shock fixed

coordinates in that the governing equations and the boundary conditions for

these seemingly different cases are nearly identical. The governing equations for

for these boundary layers have been combined into a single set of equations in

Ref. 7 which is summarized as follows.

Consider the steady boundary layer on a stationary flat plate as shown

in Fig. 2(a). The wall velocity u_w is zero and the free-stream velocity is

denoted by u_{∞}. A typical velocity profile is shown. Fig. 2(b) shows a

shock wave moving with velocity U_s into region 1 along and perpendicular to a flat wall of infinite extent. The velocity of the fluid behind the shock is u_2. The shock wave may be fixed by subtracting U_s from every part of the flow field, including the wall. The resulting flow is illustrated in Figure 2(c). Note that the wall velocity u_w is greater than the free-stream velocity u_∞. Also, the transformation to shock-fixed coordinates removes the unsteadiness which is present in the wall-fixed reference frame. The similarity between the M region and steady-state boundary layers is now evident. The only difference is that the wall velocity is finite for the M region case and zero for the steady-state case.

The analysis may continue now by treating the steady-state boundary layer, Fig. 2(a), and the M region boundary layer, Fig. 2(c), as the same problem except for the wall velocities. The continuity, momentum, and energy equations for steady, thin two-dimensional, compressible, laminar boundary-layer in thermochemical equilibrium with zero pressure gradient are:

Continuity:

$$\frac{\partial(\rho u)}{\partial x} + \frac{\partial(\rho v)}{\partial y} = 0 \tag{1}$$

Momentum

$$\rho u \frac{\partial u}{\partial x} + \rho v \frac{\partial u}{\partial y} = \frac{\partial}{\partial y}\left(\mu \frac{\partial u}{\partial y}\right) \tag{2}$$

Energy

$$\rho u \frac{\partial h}{\partial x} + \rho v \frac{\partial h}{\partial y} = \frac{\partial}{\partial y}\left(k \frac{\partial T}{\partial y}\right) + \mu \left(\frac{\partial u}{\partial y}\right)^2 \tag{3}$$

In these equations x is either x in Fig. 2(a) or x' in Fig. 2(c). In Eq. (3) k is the total thermal conductivity[8].

The boundary conditions, referring to Figs. 2(a) and 2(c), are:

$$u(x,0) = \begin{cases} 0 & \text{for steady-state case} \\ u_W & \text{for M region case} \end{cases} \tag{4a}$$

$$v(x,0) = 0 \tag{4b}$$

$$h(x,0) = h_w \tag{4c}$$

$$h(x,\infty) = h_\infty \tag{4d}$$

$$u(x,\infty) = u_\infty \tag{4e}$$

In Eq. (4c) h_w is assumed constant. Using boundary conditions (4a) and (4b), evaluation of Eq. (2) at the wall (y = 0) yields

$$\frac{\partial}{\partial y}\left(\mu \frac{\partial u}{\partial y}\right)\Big|_{y=0} = \frac{\partial \tau^*}{\partial y}\Big|_{y=0} = 0 \tag{5}$$

where τ^* is the shear stress. Thus boundary condition (4b) may be replaced by Eq. (5). The independent variables are now changed from (x,y) to ($\eta = x$, u) and the boundary layer equations becomes:

continuity

$$(\rho u)_\eta - \frac{y_\eta}{y_u}(\rho u)_u + \frac{1}{y_u}(\rho v)_u = 0 \tag{6}$$

momentum

$$\tau^*_{uu} + u\left(\frac{\rho\mu}{\tau^*}\right)_\eta = 0 \tag{7}$$

energy

$$\rho\mu u h_\eta + \frac{1}{2}\left(1 - \frac{1}{\sigma}\right)h_u(\tau^*_u)^2 = (\tau^*)^2\left[1 + \left(\frac{h_u}{\sigma}\right)_u\right] \tag{8}$$

where σ is the effective Prandtl number[8] which implicitly incorporates the influence of dissociation and ionization. The transformed boundary conditions are:

at $\quad u = u_w \ (y = 0)$

$$h = h_w \tag{9a}$$

$$\gamma_u^* = 0 \tag{9b}$$

at $\quad u = u_\infty \ (y = \infty)$

$$h = h_\infty \tag{9c}$$

$$\gamma^* = 0 \tag{9d}$$

The following dimensionless variables are now introduced:

$$\gamma = \frac{\gamma^*}{\rho_\infty u_\infty^2} \tag{10}$$

$$\beta = \frac{u_w - u}{u_w - u_\infty} \tag{11}$$

$$H = \frac{h - h_\infty}{h_\infty} \tag{12}$$

The momentum equation then becomes

$$\frac{1}{\left(1 - \frac{u_w}{u_\infty}\right)^2} \gamma_{\beta\beta} + \beta^* \left(\frac{\rho u}{\rho_\infty^2 u_\infty \gamma}\right)_\gamma = 0 \tag{13}$$

where

$$\beta^* = \frac{u_w}{u_\infty} + \left(1 - \frac{u_w}{u_\infty}\right)\beta \tag{14}$$

Note that for the steady state case $\beta^* = \beta$ since $u_w = 0$.

The energy equation becomes

$$\tau \tau_\beta H_\beta = \tau^2 \frac{(u_\infty - u_w)^2}{h_\infty} + \tau\left(\frac{\tau}{\sigma} H_\beta\right)_\beta - \frac{\rho \mu (u_\infty - u_w)^2 \beta^* H_\eta}{\rho_\infty^2 u_\infty^3}\eta$$

The boundary conditions become

at $\beta = 0$ and all η

$$\tau_\beta = 0 \tag{16a}$$

$$H = H_w \tag{16b}$$

at $\beta = 1$ and all η

$$\tau = 0 \tag{16c}$$

$$H = 0 \tag{16d}$$

Note that the difference between the M region and the steady state boundary layers is incorporated in the equations in terms of u_w. The boundary conditions are now the same for both cases.

The solution of the momentum equation is found by separation of variables. The solution for the shear stress is:

$$\tau(\eta, \beta) = \left(1 - \frac{u_w}{u_\infty}\right)\sqrt{\frac{\mu_\infty}{\rho_\infty u_\infty \eta}} \; \phi(\beta) \tag{17}$$

where $\phi\,(\beta)$ is the solution of:

$$\phi\,\phi_{\beta\beta} + \frac{\beta^* C}{2} = 0 \tag{18}$$

and $\quad C = \rho\mu/\rho_\infty\mu_\infty.$ $\tag{19}$

Substituting Eq. (17) into Eq. (15), the energy equation becomes:

$$\phi\,\phi_\beta\,H_\beta = \phi^2\,\frac{(U_\infty - U_w)^2}{h_\infty} + \phi\left(\frac{\phi}{\sigma}\,H_\beta\right)_\beta + \frac{\rho\mu}{\rho_\infty}\,\beta^{\ast}\eta\,H_\eta \tag{20}$$

It is noted that the form of Eq. (20) does not change with increasing η, and that the boundary conditions on H, Eqs. (16b) and (16d), are the same for all η. Thus the solution does not depend on η, and the last term may be dropped from Eq. (20). The energy equation can then be written as:

$$\left(\frac{\phi^{1-\sigma}}{\sigma}\,H_\beta\right)_\beta = -\phi^{1-\sigma}\,\frac{(U_\infty - U_w)^2}{h_\infty} - \frac{\phi^{1-\sigma}}{\sigma}\,H_\beta\,\sigma_\beta\,\ell n\,\phi \tag{21}$$

The boundary conditions are now

$\phi_\beta = 0,\ H = H_w\quad$ at $\beta = 0,$

$\phi = 0,\ H = 0\quad$ at $\beta = 1.$

Thus Eqs. (18) and (21) may be written in integral form as:

$$\phi\,(\beta) = \left[\int_\beta^1 \phi\,(P) \int_0^P \frac{C(\beta)}{\phi(\beta)}\,\beta^{\ast}\,d\beta\,dP\right]^{\frac{1}{2}} \tag{22}$$

$$H(\beta) = -H_{\beta}(0) \frac{\bar{\phi}(0)}{\sigma(0)} \int_{\beta}^{1} \frac{\sigma(P)}{\bar{\phi}(P)} dP$$

$$+ \frac{(U_{\infty} - U_{w})^2}{h_{\infty}} \int_{\beta}^{1} \frac{\sigma(P)}{\bar{\phi}(P)} \int_{0}^{P} \phi(N) dN dP$$

$$+ \int_{\beta}^{1} \frac{\sigma(P)}{\bar{\phi}(P)} \int_{0}^{P} \frac{\bar{\phi}(N)}{\sigma(N)} H_{N} \ln[\phi(N)] \sigma_{N} dN dP \qquad (23)$$

where

$$\bar{\phi}(\beta) = [\phi(\beta)]^{(1-\sigma(\beta))}$$

and P and N are dummy variables for β. Coupling exists between Eqs. (22) and (23) since C, Eq. (19), appears in Eq. (22) and is a function of H.

Of particular interest here is the wall heat flux $q_{w} = -k(\partial T/\partial y)_{w}$, which, when written in terms of the present variables, becomes:

$$q_{w} = - \frac{\tau_{w} \rho_{\infty} u_{\infty}^2 h_{\infty}}{\sigma_{w}(U_{\infty} - U_{w})} (H_{\beta})_{w} \qquad (24)$$

where $(H_{\beta})_{w}$ is the enthalpy gradient at the wall ($\beta = 0$). Substituting for τ_{w} from Eq. (17) a dimensionless heat transfer quantity is obtained.

$$Q = \frac{-q_{w}\sqrt{\tau} \sigma_{w}}{h_{\infty}\sqrt{\rho_{\infty}\mu_{\infty} u_{\infty}}} = \phi_{w}(H_{\beta})_{w} \qquad (25)$$

Thus, specification of u_w in Eq. (22) (through Eq. (14)) and in Eq. (23) permits evaluation of the dimensionless shear stress, Eq. (17), and the dimensionless heat transfer, Eq. (25), for either the steady state boundary layer or the M region boundary layer viewed in shock-fixed coordinates.

At this point interpretation of the quantities obtained above can be made in term of the coordinates in Fig. 2. Consider first the steady boundary layer in Fig. 2(a). The profiles $\phi(\beta)$ and $H(\beta)$ obtained from Eqs. (22) and (23) with $u_w = 0$, denoted here as $\phi(\beta)_{ss}$ and $H(\beta)_{ss}$, apply to this boundary layer. In addition, the shear stress and heat transfer from Eqs. (17) and (25) are

$$\tau(x,\beta) = \sqrt{\frac{\mu_o}{\rho_o u_o x}} \; \phi(\beta)_{ss} \tag{26}$$

$$Q_{ss} = \frac{-g_w \sqrt{x} \; \sigma_w}{h_o \sqrt{\rho_o \mu_o u_o}} = \left[\phi_w \left(H_\beta \right)_w \right]_{ss} \tag{27}$$

where η in Eqs. (17) and (25) is replaced by x, the plate distance coordinate in both Figs. 1(a) and 2(a), and the subscript "o" is used to denote the free-stream quantities.

Next consider the M region boundary viewed in shock fixed coordinates, Fig. 2(c). The $\phi(\beta)$ and $H(\beta)$ profiles obtained from Eqs. (22) and (23) with $u_w = U_s$, which are denoted as $\phi(\beta)_{Msf}$ and $H(\beta)_{Msf}$, apply to the boundary layer in this figure. The expressions for shear stress and heat transfer from Eqs. (17) and (25) are:

$$\tau(x',\beta) = \left(1 - \frac{U_s}{u_\infty}\right)\sqrt{\frac{\mu_\infty}{\rho_\infty u_\infty x'}} \; \phi(\beta)_{Msf} \tag{28}$$

$$Q_{Msf} = \frac{-q_w \sqrt{x'} \; \sigma_w}{h_\infty \sqrt{\rho_\infty \mu_\infty u_\infty}} = \left[\phi_w (H_\beta)_w \right]_{Msf} \tag{29}$$

where x' is the distance coordinate measured in the downstream direction relative to the shock as shown in Fig. 2(c). It is also noted from Fig. 2(c) that $U_s/u_\infty = \rho_\infty / \rho_1$, the density ratio across the shock.

When a point on the moving wall is at the origin of the x', y' coordinate system of Fig. 2(c) at time t' = 0, the position of the point at time t' is x' = U_st'. Note that this is also the distance the moving shock travels past a point on the shock tube sidewall in time t'. Substitution of x' = U_st' into Eq. (29) yields

$$q_w \sqrt{t'} = \frac{h_\infty}{\sigma_w} \sqrt{\frac{\rho_\infty \mu_\infty u_\infty}{U_s}} \left[\phi_w (H_\beta)_w \right]_{Msf} \tag{30}$$

Thus, for a given sidewall boundary layer, $q \sqrt{t'}$ = const.

Eqs. (26) and (27) and Eqs. (28) and (29) provide the shear stress and heat transfer solutions in the coordinate systems noted for these equations. It is next of interest to transfer each of these solutions to the coordinate system of Fig. 1(b), i.e., to the coordinates $\alpha = x/u_o t$, $\beta = u/u_o$, and $\gamma = u_o^2 t / \nu_o$. For the steady state region this is readily accomplished and Eqs. (26) and (27) become:

$$T_{ss} (\alpha, \beta, \gamma) = \sqrt{\frac{1}{\alpha \gamma}} \; \phi(\beta)_{ss} \tag{31}$$

$$Q_{ss} (\alpha, 0, \gamma) = \frac{q_w \sqrt{\alpha \gamma} \; \sigma_w}{h_o \rho_o u_o} = \left[\phi_w (H_\beta)_w \right]_{ss} \tag{32}$$

For the M region of Fig. 1(b) it is noted that $x + x' = U_s t$, where x is the distance coordinate in Fig. 1(a) and x' is the distance coordinate in Fig. 2(c) in which u_∞ is the free stream velocity. Hence $u_o + u_\infty = U_s$. Substitution for x' and u_∞ in Eqs. (28) and (29) yields for the M region:

$$\tau_M(\alpha, \beta, \gamma) = \sqrt{\frac{A-1}{\gamma(A-\alpha)}} \quad \phi(\beta)_{Msf} \tag{33}$$

$$Q_M(\alpha, 0, \gamma) = \frac{g_w \sqrt{\alpha \gamma}\; \sigma_w}{h_o \rho_o u_o} = \sqrt{\frac{\alpha(A-1)}{A-\alpha}} \left[\phi_w (H_\beta)_w\right]_{Msf} \tag{34}$$

Further interpretation of Eqs. (31) to (34) will be made after the interaction region solutions are discussed.

Solution of the Boundary Layer Equations for the Interaction Region

The equations for the laminar boundary layer in the interaction region for real gas flows in thermochemical equilibrium are:

continuity

$$\frac{\partial \rho}{\partial t} + \frac{\partial (\rho u)}{\partial x} + \frac{\partial (\rho v)}{\partial y} = 0 \qquad (35)$$

momentum

$$\rho \frac{\partial u}{\partial t} + \rho u \frac{\partial u}{\partial x} + \rho v \frac{\partial u}{\partial y} = \frac{\partial}{\partial y}\left(\mu \frac{\partial u}{\partial y}\right) \qquad (36)$$

energy

$$\rho \frac{\partial h}{\partial t} + \rho u \frac{\partial h}{\partial x} + \rho v \frac{\partial h}{\partial y} = \frac{\partial}{\partial y}\left(k \frac{\partial T}{\partial y}\right) + \mu \left(\frac{\partial u}{\partial y}\right)^2 \qquad (37)$$

where k in Eq. (37) is the total thermal conductivity and the coordinate system is that of Fig. 1(a). From previous discussion it is noted that the following boundary conditions apply.

$$u(x,0,t) = 0 \qquad (38a)$$

$$v(x,0,t) = 0 \qquad (38b)$$

$$h(x,0,t) = h_w = \text{const.} \qquad (38c)$$

$$u(x,\infty,t) = u_o \qquad (38d)$$

$$h(x,\infty,t) = h_o \qquad (38e)$$

Evaluation of the momentum equation at the wall yields:

$$\frac{\partial}{\partial y}\left(\mu \frac{\partial u}{\partial y}\right)\bigg|_{y=0} = \frac{\partial \tau}{\partial y}\bigg|_{y=0} = 0 \qquad (39)$$

which replaces boundary condition (38b). Transforming the equations from the independent variables (x,y,t) to ($\eta = x$, u, $\xi = t$) and incorporating the continuity equations into the momentum and energy equations, Eqs. (35) to (37) become:

momentum

$$u\left(\frac{\rho\mu}{\gamma^{*}}\right)_{x} + \gamma_{uu}^{*} + \left(\frac{\rho\mu}{\gamma^{*}}\right)_{\xi} = 0 \tag{40}$$

energy

$$\rho\mu\left[h_{\xi} + u\,h_{x}\right] + \gamma^{*}\gamma_{u}^{*}h_{u} = \gamma_{*}^{2} + \gamma^{*}\left(\frac{\gamma^{*}}{\sigma}h_{u}\right)_{u} \tag{41}$$

σ^{*} in Eq. (41) is the effective Prandtl number[8]. Equations (40) and (41) written in terms of the independent variables of Fig. 1(b), $\alpha = x/u_{o}t$, $\beta = u/u_{o}$ and $\gamma = u_{o}^{2}t/\gamma_{o}^{*}$, with $H = (h - h_{o})/h_{o}$ and $\gamma = \gamma^{*}/\rho_{o}u_{o}^{2}$ as independent variables are:

$$\gamma^{2}\gamma_{\beta\beta} = C\left(\frac{\beta-\alpha}{\gamma}\right)\gamma_{\alpha} + C\gamma_{\gamma} - \gamma C_{\gamma} + \gamma\left(\frac{\alpha-\beta}{\gamma}\right)C_{\alpha} \tag{42}$$

$$C\left[H_{\gamma} - H_{\alpha}\left(\frac{\alpha-\beta}{\gamma}\right)\right] + \gamma\gamma_{\beta}H_{\beta} = \frac{u_{o}^{2}}{h_{o}}\gamma^{2} + \gamma\left(\frac{\gamma}{\sigma}H_{\beta}\right)_{\beta} \tag{43}$$

where $C = \rho\mu/\rho_{o}\mu_{o}$. A solution for the shear stress in terms of a new shear stress variable ϕ is defined as

$$\gamma(\alpha,\beta,\gamma) = \phi(\alpha,\beta,\gamma)/\sqrt{\alpha\gamma} \tag{44}$$

When this expression is substituted into Eqs. (42) and (43), these equations become:

$$\phi^{2}\phi_{\beta\beta} - C\alpha(\beta-\alpha)\phi_{\alpha} - \phi\alpha(\alpha-\beta)C_{\alpha} + C\beta\phi/2 = \alpha\gamma(C\phi_{\gamma} - \phi C_{\gamma}) \tag{45}$$

$$\left(\frac{H_{\beta}}{\sigma}\right)_{\beta} + \phi^{-1}\phi_{\beta}H_{\beta}\left(\frac{1}{\sigma}-1\right) - \frac{C\alpha(\beta-\alpha)}{\phi^{2}}H_{\alpha} + \frac{u_{o}^{2}}{h_{o}} = \frac{C\alpha\gamma}{\phi^{2}}H_{\gamma} \tag{46}$$

The region of interest for the above equations is the interaction region $0 \leq \alpha \leq 1$, $0 \leq \beta \leq 1$, $\gamma > 0$, in Fig. 1(b). Hence, boundary conditions must be supplied for this region. The boundary conditions on ϕ at $\alpha = 0$ are furnished by the previously discussed steady state solution of the momentum equation. Lam[2] has shown that the solution at $\alpha = 1$ is that for the M region at $\alpha = 1$. Combination of Eqs. (33) and (44) yields

$$\phi(\alpha, \beta) = \sqrt{\frac{\alpha(A-1)}{(A-\alpha)}} \; \phi(\beta)_{Msf} \tag{47}$$

which expresses ϕ for the M region of Fig. 1(b). The boundary conditions for $\beta = 0$ and $\beta = 1$ are obtained by transferring those listed in Eqs. (38) to the (α, β, γ) coordinate system. The boundary conditions for Eqs. (45) and (46) then become:

$$\phi(0, \beta, \gamma) = \phi(\beta)_{ss} \qquad H(0, \beta, \gamma) = H(\beta)_{ss} \tag{48a}$$

$$\phi(1, \beta, \gamma) = \phi(\beta)_{Msf} \qquad H(1, \beta, \gamma) = H(\beta)_{Msf} \tag{48b}$$

$$\phi(\alpha, 0, \gamma) = \phi_w \qquad H(\alpha, 0, \gamma) = H_w \tag{48c}$$

$$\phi(\alpha, 1, \gamma) = 0 \qquad H(\alpha, 1, \gamma) = 0 \tag{48d}$$

It is noted that these boundary conditions are independent of γ. Further, it is noted that Eqs. (45) and (46) do not change in form as γ changes, i.e., when $\gamma^* = B\gamma$ (where B is an arbitrary constant) is substituted into Eqs. (45) and (46), the expressions on the righthand side of these equations undergo no change in form. Hence ϕ and H are independent of γ and therefore the γ derivatives are zero. H and ϕ remain as functions of α and β only. Integration of Eqs. (45) and (46) along lines of constant α along with the

application of the boundary conditions[+] in Eqs. (48) yields:

$$\phi(\alpha,\beta) = \left\{ \int_{\beta}^{1} \phi(\alpha,\xi) \int_{0}^{\xi} \frac{C(\alpha,\lambda)}{\phi(\alpha,\lambda)} \left[\lambda - 2\alpha(\lambda-\alpha) \right. \right.$$

$$\left. \left. \left(\frac{\phi_{\alpha}(\alpha,\lambda)}{\phi(\alpha,\lambda)} - \frac{C_{\alpha}(\alpha,\lambda)}{C(\alpha,\lambda)} \right) \right] d\lambda\, d\xi \right\}^{1/2} \qquad (49)$$

$$H(\alpha,\beta) = -H_{\beta}(\alpha,0) \frac{\phi^{1-\sigma(\alpha,0)}(\alpha,0)}{\sigma(\alpha,0)} \int_{\beta}^{1} \frac{\sigma(\alpha,\xi)}{\phi^{1-\sigma(\alpha,\xi)}(\alpha,\xi)} d\xi$$

$$- \alpha \int_{\beta}^{1} \frac{\sigma(\alpha,\xi)}{\phi^{1-\sigma(\alpha,\xi)}(\alpha,\xi)} \int_{0}^{\xi} \frac{C(\alpha,\lambda)(\lambda-\alpha)\, H_{\alpha}(\alpha,\lambda)}{\phi^{1+\sigma(\alpha,\lambda)}(\alpha,\lambda)} d\lambda\, d\xi$$

$$+ \frac{u_{o}^{2}}{h_{o}} \int_{\beta}^{1} \frac{\sigma(\alpha,\xi)}{\phi^{1-\sigma(\alpha,\xi)}(\alpha,\xi)} \int_{0}^{\xi} \phi^{1-\sigma(\alpha,\lambda)}(\alpha,\lambda)\, d\lambda\, d\xi$$

$$+ \int_{\beta}^{1} \frac{\sigma(\alpha,\xi)}{\phi^{1-\sigma(\alpha,\xi)}(\alpha,\xi)} \int_{0}^{\xi} \frac{\phi^{1-\sigma(\alpha,\lambda)}(\alpha,\lambda)}{\sigma(\alpha,\lambda)} H_{\lambda}(\alpha,\lambda)\, \ell_{n}\phi(\alpha,\lambda)\, \sigma_{\lambda}(\alpha,\lambda)\, d\lambda\, d\xi \qquad (50)$$

[+]Ref. 1 lists four additional "derived" boundary conditions which aid in the numerical solutions of Eqs. (49) and (50). They are: $\phi_{\alpha}(0,\beta) = 0$, $H_{\alpha}(0,\beta) = 0$, $\phi_{\alpha}(1,\beta) = [\phi_{insf}(\beta)/2][A/(A-1)]$, $H_{\alpha}(1,\beta) = 0$.

As was the case for the energy and momentum equations for the steady state and M regions, Eqs. (49) and (50) are coupled since C in Eq. (49) is a function of H determined by Eq. (50) and ϕ in Eq. (49) also appears in Eq. (50).

Of concern here is the expression for the wall heat flux $q_w = -k(\partial T/\partial y)_w$ for the interaction region. In terms of the present variables,

$$q_w(\alpha, \gamma) = \frac{\tau(\alpha, 0, \gamma) \rho_o u_o h_o}{\sigma_w} H_\beta(\alpha, 0) \tag{51a}$$

$$= \frac{\rho_o u_o h_o}{\sigma_w \sqrt{\alpha \gamma}} \phi(\alpha, 0) H_\beta(\alpha, 0) \tag{51b}$$

where $\phi(\alpha, 0)$ and $H_\beta(\alpha, 0)$ are from the solutions of Eqs. (49) and (50) respectively and substitution for τ from Eq. (44) has been made. Equation (51b) can be written in dimensionless form as

$$Q(\alpha, 0) = \frac{q_w \sqrt{\alpha \gamma} \, \sigma_w}{\rho_o u_o h_o} = \phi(\alpha, 0) H_\beta(\alpha, 0) \tag{52}$$

Thus the heat transfer variable Q has been specified for the complete range of interest: referring to Fig. 1(b), Eq. (32) applies to the steady state portion of the interaction region, Eq. (52) is applicable to the entire interaction region, and Eq. (34) applies to the M region. It is noted that Q depends only on the time-position variable α.

Theoretical Heat Transfer Solutions

In order to obtain the desired solutions for a given flow condition, it is necessary to numerically integrate Eqs. (22) and (23) for the steady state and M regions and Eqs. (49) and (50) for the interaction region. The method of solution of these equations is outlined in Ref. 1 and 7 and need not be discussed. Of the several descriptive boundary layer characteristics, only the solutions for the heat transfer quantities will be presented, since heat transfer to the plate is the primary concern of the present study.

When real gases in equilibrium at high temperatures are considered, the dimensionless solutions to the boundary layer equations depends on pressure, since pressure influences the variation of the $\rho\mu$ product ratio $C = \rho\mu / \rho_d \mu_0$, the effective Prandtl number σ, and the density ratio ρ_s / ρ_1 across the incident shock. The solutions presented in Ref. 1 were obtained for air at a free-stream pressure p_o of 1 atm and $T_w = 300°K$. The relations for viscosity and density variation with enthalpy used in obtaining those solutions are those presented in equation form by Mirels[9] and Viegas and Howe[10]. Mirels' equations were used for values of h/h_w up to 4.53. The equations of Viegas and Howe, which are based on Ref. 8, were applied at higher values of h/h_w. The effective Prandtl number variation with enthalpy was taken from Ref. 8. Free-stream properties behind the incident shock were obtained using Refs. 11, 12, and 13. The solutions for heat transfer at $P_o = 1$ atm from Ref. 1 serve as a basis for the discussion in the following paragraphs.

As noted in Ref. 1, interpretation of the solutions in terms of the present variables for the boundary layer considered here can be made by taking two different points of view. Interpretation for fixed x positions is desired for the present study because measurement of the heat flux to the plate is made at fixed x values. Also of some interest is the nature and

configuration of the boundary layer at any point in time. However, for the reason noted, only the fixed x interpretation will be made here. It is noted that the quantity $(\alpha\gamma)^{\frac{1}{2}}$ appears in each of the equations, Eqs. (32), (34), and (52), that collectively predict the heat transfer quantity Q vs α. Substituting for α and γ, $(\alpha\gamma)^{\frac{1}{2}} = (u_o x/\gamma_o)^{\frac{1}{2}} = (Re)^{\frac{1}{2}}$. Thus for fixed x,

$$Q_x(\alpha) = Q_w (Re)^{\frac{1}{2}} \sigma_w /(\rho_o u_o h_o) = \frac{Q_w \sqrt{x} \ \sigma_w}{\sqrt{\rho_o \mu_o u_o} \ h_o} \tag{53}$$

where Re is the Reynolds number and x is the distance measured from the plate leading edge. A typical solution for Q_x vs α is presented in Fig. 3. When x is fixed, $\alpha = x/u_o t$ becomes a time variable and α decreases with increasing time. The time x/U_s corresponds to the shock arrival at the given x location and the corresponding value of α is A. Times less than x/U_s (values of $\alpha > A$) are of no interest. With increasing time the boundary layer develops and approaches the steady state condition for the given x location. This behavior is observed in terms of Q_x in the figure. Eq. (34) for the M region predicts the expected infinite value for Q_x at $\alpha = A$. With decreasing α (increasing time) Q_x decays to $(\phi_w (H_\beta)_w)_{Msf}$ at $\alpha = 1$ according to Eq. (34). Q_x continues to decay along the curve predicted by Eq. (52) and approaches the steady state solution, Eq. (32), asymtotically with decreasing α.

Several important observations can be made regarding the solutions for Q_x typified by Fig. 3. First, a given solution Q_x vs α is self similar in the sense that it applies at any fixed x provided the plate is at least of length $U_s t$. Next, as might be expected, the steady state Q_x is essentially reached at values of $\alpha > 0$, i.e., before infinite time. Further, the interaction region solution is asymtotic to both the steady state and M region solutions as is illustrated by the extended curves for these regions.

Use has been made of this fact to correlate the heat transfer results, (Ref. 1).

Fig. 4 presents such a correlation for air. This figure presents two ratios

defined as

$$R_{ss} = \frac{Q_x, \text{ Eq. (52)}}{Q_x, \text{ Eq. (32)}} \tag{54}$$

$$R_M = \frac{Q_x, \text{ Eq. (52)}}{Q_x, \text{ Eq. (34)}} \tag{55}$$

in terms of α and the shock speed U_s. This figure permits Q_x vs α to be

predicted provided the steady state and M region values for Q_x are available.

Quantities which permit the determination of Q_x for the steady state and M region

for air at a pressure of 1 atm are presented in Fig. 5. To construct a

solution Q_x vs α for a given U_s, the known steady state and M solutions are

extended in the manner shown in Fig. 3. Values of the ratios R_{ss} and R_M

and the corresponding α values are then determined from Fig. 4 at the given

U_s. Eqs. (54) and (55) are next used to predict values Q_x (at the several

α values corresponding to the ratio values in Fig. 4) for the interaction

region. The interaction region curve can then be drawn through these points

asymtotic to the steady state and M region extended curves. This method

eliminates the somewhat tedious and expensive procedure of solving Eqs. (49)

and (50) in order to compute Q_x for the interaction region by Eq. (52).

The influence of pressure on values for the dimensionless boundary layer

quantities is most pronounced for shock tube flows generated by incident

shocks at high speeds. For air with $T_w = T_1 = 300^\circ K$, the influence of pressure

on the dimensionless boundary layer quantities begins at about $U_s = 2$ km/sec.

and increases with increasing shock speed. Therefore, for cases for which

the incident shock speed is low, the solutions Q_x vs α determined using Figs.

4 and 5 would be satisfactory regardless of the value of p_o. For high shock

speeds where p_o differs significantly from 1 atm., the quantities in Fig. 5, especially those for the M region, are not satisfactory, and it is therefore necessary to obtain solutions to Eqs. (22) and (23) at the given pressure that lead to computation of Q_x for the steady state and M regions by Eqs. (32) and (34). For exact solutions in the interaction region at high shock speeds it is also necessary to solve Eqs. (49) and (50) at the given pressure in order to determine Q_x in the interaction region using Eq. (52). However, since it is not easy to obtain these solutions, a good approximation of the solution for Q_x in the interaction region can be obtained using the ratios in Fig. 4 provided the quantities for Eqs. (32) and (34) are obtained at the given pressure.

Fig. 4 is strictly applicable only to air. However, it is doubtful that the ratios R_{ss} and R_M would be significantly different for nitrogen.

HEAT FLUX MEASUREMENT IN SHOCK TUBE FLOWS

In order to measure transient heat transfer rates in shock tube flows it is necessary to use an instrument with very fast response; one with a response time of a few microseconds or less. This consideration is particularly important when the flow duration is of the order of tens of microseconds. In addition to fast response it is important that the instrument be reliable, easy to construct and use, and durable. The thin-film heat flux gage[14] is the only practical type heat flux gage that satisfies most of these requirements and was therefore chosen to measure heat transfer rates in this study. The central idea of the gage system is to measure the temperature on or near the surface of a semi-infinite solid initially at uniform temperature exposed to the shock tube flow and to deduce the heat flux to the solid using heat conduction theory and the measured temperature. The purpose of this section is to describe some of the important theoretical and practical considerations involved in heat flux measurement using thin-film heat flux gages.

The Thin-film Heat Flux Gage

Fig. 6 shows a schematic of the thin-film heat flux gage. A platinum film of thickness δ_F is deposited on the surface of a substrate that is of sufficient thickness to behave as a semi-infinite medium during the shock tube testing time. Code 7740 Pyrex is a commonly used substrate since its thermal properties are well known. A coating of thickness δ_C (usually silicon dioxide[15]) is deposited over the platinum film to eliminate electrical shorting of the gage if the gage is to be used in ionized flows. The platinum film serves as a resistance thermometer and is placed in a "ballast" circuit in which the electrical current is maintained essentially constant by making

R_B very large compared to the film resistance. An oscilloscope and camera is used to record the film voltage change vs time during testing. The gage voltage response may be related to temperature change as follows. Considering the current I_o in Fig. 6 to be constant, the voltage change across the film is given by

$$\Delta E_F = I_o \Delta R_F \tag{56}$$

where ΔR_F is the change in film resistance which is related to temperature change T to a high degree of accuracy in the range of temperature change of concern here by the linear relation

$$\Delta R_F = (\Delta R / \Delta \theta) T$$

where $\Delta R / \Delta \theta$ is the slope of the resistance vs temperature plot for the film. Substituting into Eq. (56),

$$\Delta E_F = I_o (\Delta R / \Delta \theta) T = I_o R_o (\Delta R / \Delta \theta R_o) T = E_o \, \Gamma \, T$$

or

$$T = \Delta E_F / E_o \, \Gamma \tag{57}$$

E_o is the initial voltage drop across the film which has an initial resistance R_o. Thus when I_o is constant* the temperature change T indicated by the film is related to E_o, the film voltage change ΔE_F (a function of time) recorded by the oscilloscope, and the resistance-temperature parameter Γ. The latter quantity is usually determined by static measurement of resistance vs temperature for the film.

---

*A more detailed analysis of the thin-film gage circuit which does not assume constant current yields the following expression for the temperature change

$$T = \left[1 + (R_o + \Delta R_F) / R_B \right] (\Delta E_F / E_o \, \Gamma)$$

Thus if $R_B \gtrsim 100 \, R_o$, Eq. (57) yields temperature change values that are correct within one percent.

Interpretation of Gage Response

In general it is a complex matter to interpret thin-film gage response to determine the surface heat flux, especially for times of the order of microseconds. This is due in part to the finite thickness of both the coating and the platinum film. It is noted that the film would, due to the presence of the coating, respond to a temperature change that is not that on the surface. A temperature gradient might exist through the film adding a further complication. No solution is readily available for this complex heat conduction problem. However certain special cases have been solved that permit insight into the influence of the factors mentioned above.

It should be noted that the characteristic heat diffusion depth (see Carslaw and Jaeger, Ref. 16) is much less than the gage width W shown in section A-A of Fig. 6 for the time intervals of concern here. Therefore heat conduction in the gage materials can reasonably be treated in one dimension.

Uncoated platinum film. - One special case of interest is that in which the coating thickness δ_C is zero, i.e., the case of an uncoated platinum film on pyrex. As a result of the fact that platinum thermal properties differ significantly from those of pyrex, the platinum film on the pyrex substrate will at very early times after heat flux application have a temperature different than the surface of the adjacent substrate not covered by the film. Hence at early times the film does not indicate the true substrate surface temperature denoted here as T_∞. Kurzrock[17] and Camac and Feinberg[18] have analyzed this problem for certain cases of surface heat flux variation with time and determined the temperature change T_I at the interface of the platinum and the substrate. Fig. 7, which is based on the work of these investigators, presents curves T_I/T_∞ vs the Fourier modulus $\bar{\theta}$ for two cases of surface heat flux. The case of the surface heat flux proportional to $t^{-\frac{1}{2}}$ is of particular interest here because this is the heat flux variation with time that would be expected

on the shock tube side wall as the shock wave passes any given location. This heat flux case has not been investigated as thoroughly as has the constant heat flux case. However, it is noted that the approximate curves for this case, which are based on computations for a small range of $\bar{\theta}_F$ in Ref. 18, are not significantly different from those for the constant heat flux case. It is noted in Fig. 7 that in addition to a dependence on $\bar{\theta} = \alpha_F t / \delta_F^2$ and a mild dependence on the nature of the surface heat flux, T_I/T_∞ also depends on the quantity $\psi = \sqrt{(k\rho c)_s/(k\rho c)_F}$. (The subscripts s and F indicate substrate and film respectively and α_F is the film thermal diffusivity. In this section t is time measured from the instant of application of the heat flux and is not the time in the distance-time variable α.) For platinum on pyrex, $\psi = 0.1$, as noted in the figure. The curves show that when $\bar{\theta}$ is very large (i.e., for large times or small δ_F) T_I/T_∞ is essentially unity regardless of the nature of the surface heat flux or the value of ψ. Under this condition substitution of gage response (voltage vs time) into Eq. (57) yields the true substrate surface temperature change. When substrate properties are considered to be constant and one dimensional heat conduction is assumed, the heat flux can be found by the expression[18,19]

$$q(o,t) = \frac{\sqrt{(k\rho c)_s}}{\pi^{1/2}} \left[\frac{T(0,t)}{t^{1/2}} + \frac{1}{2} \int_0^t \frac{T(0,t) - T(0,\lambda)}{(t-\lambda)^{3/2}} \, d\lambda \right] \tag{58}$$

where $T(0,t)$ is the substrate surface temperature change T_∞ that would exist in the absence of the film (or coating) and is an arbitrary function of time.

For the case where the modulus $\bar{\theta}_F$ is small, i.e., small times or a relatively thick film, it can be seen in Fig. 7 that T_I/T_∞ is less than unity. Fig. 8 presents for $\psi = 0.1$ and the two cases of surface heat flux the ratio T_I/T_∞ vs time computed for a range of $\bar{\theta}_F$ for film thicknesses of 250 A° and

1000 A^O. Due to the high thermal diffusivity of platinum, only a small

temperature gradient would be expected through the film regardless of the value

of $\overline{\theta}_F$. Therefore the temperature sensed by the film would be essentially T_I.

This is then the temperature vs time that would be computed from the gage

response (voltage vs time) using Eq. (57). Since T_I is not the true substrate

surface temperature, integration of Eq. (58) using this computed temperature

would yield an incorrect heat flux variation with time. However, Fig. 8 can

be used to estimate the true substrate temperature T_{∞} as follows:

$$T_{\infty} = T(0,t) = \frac{T(Eq. 57)}{cf} \tag{59}$$

where cf is a correction factor approximated by

$$cf = T_I/T_{\infty} \tag{60}$$

and T_I/T_{∞} is from a curve like those in Fig. 8 with $\psi = 0.1$ plotted for the

given film thickness and the approximate expected surface heat flux. Selection

of a curve corresponding to the expected surface heat flux is necessary because

the true heat flux is obviously not known a priori. Use of such a curve amounts

to assuming that the nature of the surface heat flux is of secondary importance

in determining $T(0,t)$. Support for the latter assumption is found in Fig. 8.

It can be seen for the constant heat flux case that changing the film thickness

by a factor of four has a pronounced effect on T_I/T_{∞}. However the influence

of the nature of the surface heat flux is smaller, as can be seen from

the curves for $\psi = 0.1$ for the two heat flux cases at a film thickness of

1000 A^O. Thus it is seen that precise knowledge of the film thickness is

more important in determining cf in Eq. (59) by Eq. (60) than is knowledge of

the nature of the surface heat flux.

Coating over a very thin platinum film. Another case of interest is

that in which the film thickness approaches zero but the coating thickness

is not zero. This would correspond to a coating over a very thin film.
In this case the film senses the temperature a distance δ_C below the
surface, not the true substrate surface temperature. Curves in Fig. 7
permit analysis of this case also. Assuming that the coating has the same
thermal properties as pyrex, the modulus $\psi = \sqrt{(k\rho c)_s / (k\rho c)_F} = 1$. The
interface temperature change T_I is then given as a function of the modulus
$\bar{\theta}_F$ ($\bar{\theta}_F = \propto_C t / \delta_C^2$ in this case) by the $\psi = 1$ curves in Fig. 7. Fig. 8 also
presents T_I/T_∞ vs time for coating thicknesses of 250 and 1000 A^o
for the two cases of surface heat flux. Since the film senses the interface
temperature, $T(0,t)$ for the case of a coating over a very thin film can be
computed from Eq. (59) in which c_f would be T_I/T_∞ obtained from curves like those
in Fig. 8 with $\psi = 1$, plotted for the given coating thickness and the approxi-
mate surface heat flux variation with time. The curves in Fig. 8 for $\psi = 1$
again indicate that knowledge of the coating thickness is more important than
precise knowledge of nature of the surface heat flux. After obtaining $T(0,t)$
in this manner the heat flux can then be evaluated by Eq. (58).

Determination of Heat Flux from Surface Temperature Variation

Given $T(0,t)$, the semi-infinite solid surface temperature variation with
time, it is next of concern to determine the surface heat flux $q(0,t)$ by inte-
gration of Eq. (58), the integration of which is complicated by the fact that
$T(0,t)$ cannot usually be described by a simple mathematical expression. As a
result it is necessary to resort to a numerical integration method. A method
for numerically integrating Eq. (58) has been developed (Refs. 19-21) that yields
accurate results with a minimum number of divisions of the time axis. This
method approximates $T(0,t)$ by a piecewise linear function which is introduced

into Eq. (58). When integration is performed the following expression is obtained:

$$q_n(0, t_m) = \frac{2\sqrt{(k\rho c)_s}}{\sqrt{\pi}} \sum_{I=1}^{m} \left[\frac{T(0, t_I) - T(0, t_{I-1})}{(t_m - t_I)^{\frac{1}{2}} + (t_m - t_{I-1})^{\frac{1}{2}}} \right] \tag{61}$$

where t_I is the time at the end of the Ith of m time intervals which are not necessarily equal. The thermal parameter $\sqrt{(k\rho c)_s}$ here applies to the substrate material. Due to diffusion of the film material into the substrate during the film deposition process the thermal properties of the substrate may be significantly changed. (See Refs. 22 to 24 for example.) Bogdan[24] investigated the variation of $\sqrt{(k\rho c)_s}$ for platinum films on code 7740 pyrex and determined the quantity to be 0.0737 Btu/ft^2°F sec$^{\frac{1}{2}}$ with a standard deviation from the mean of 0.0012. It is concluded that the mean value is sufficiently accurate for most purposes. Thus when $T(0,t)$ is determined, discrete values $T(0, t_I)$ at time t_I can be determined and introduced into Eq. (61) to numerically determine the heat flux.

Influence of various factors on heat flux evaluation.- In order to illustrate the influence of various factors on the determination of the surface heat flux it is convenient to assume a gage response curve. Fig. 9(a) presents such a curve which represents a function that has an asymtotic rise to a unit change in temperature.

Time interval size: The first factor to be considered is the influence of the time interval size on the accuracy of the heat flux computed using Eq. (61). For this consideration it is assumed that the coating and film thicknesses approach zero. Thus the gage temperature response curve is the true surface temperature change $T(0,t)$. The symbols in Fig. 9(a) indicate heat flux

values computed from the assumed temperature response using Eq. (61) and

the time increments sizes noted in the figure for a period of about 21 μsec.

The heat flux is presented in terms of the quantity $q\sqrt{t} / \sqrt{(k\rho c)}_s$ since it is

of interest to compare the heat flux for the assumed gage response curve

with that for a true step in surface temperature. Exact integration of

Eq. (58) for a true unit step in surface temperature yeilds $q\sqrt{t} / \sqrt{(K\rho c)}_s = 1/\pi^{1/2}$,

which is noted on the figure. It is observed that the computed heat transfer

values vs time are essentially the same for computations made using the two

smaller time increments, indicating that a sufficient number of points have

been used to accurately compute the heat flux for the assumed curve. At

early times the computation of heat flux values using the 2.1 μsec time in-

crement differ considerably from those computed using smaller time increments.

By about 20 μsec results for all three time increment sizes agree well, and

approach the theoretical value for a unit step in temperature as time increases,

i.e., as the influence of the asymtotic rise of the assumed gage response curve

diminishes. The results in Fig. 9(a) indicate that with sufficiently small

time intervals accurate heat flux values can be computed using Eq. (61).

An additional indication of the number of points required to compute heat

flux within a prescribed percentage using Eq. (61) can be obtained by examining

Fig. 10 which is taken from Ref. 19. This figure presents for the two boundary

conditions noted the percent difference between the heat flux computed using

Eq. (61) and the corresponding exact heat flux (determined from exact integration

of Eq. (58)) as a function of the number of equal time intervals. It is noted that

the boundary condition has an influence on the accuracy of Eq. (61). It is noted

in Ref. 19 that the error in computing heat flux using Eq. (61) can be reduced

by using unequal time intervals in such a manner that the boundary condition

T(0,t) is accurately described by a piecewise linear function. Thus in practice it is best to imagine a given T(0,t) curve as being approximated by a piecewise function and to choose the discrete values of $T(0,t_I)$ and t_I in such a manner that the curve is described as accurately as possible by straight-line segments. The errors for equal time intervals in Fig. 10 can be viewed as the approximate upper bounds for the respective cases noted therein that would be encountered using Eq. (61).

Finite film thickness: Another influence of interest is that of a finite thickness platinum film. For this case, only the condition $\delta_C = 0$, as previously analyzed, will be considered. A film thickness of 500 A° is assumed. This value represents the maximum thickness expected for the films used in the experimental phase of this investigation and was estimated from film thickness measurements of platinum films on pyrex made by McCaa, ref. 22. Due to the finite film thickness, the assumed gage response in Fig. 9(a) must be introduced into Eq. (59) in order to obtain T(0,t) and, in turn, discrete values $T(0,t_I)$ and t_I for computation of heat flux by Eq. (61). The factor cf = T_I/T_∞ in Eq. (59) was obtained from a curve T_I/T_∞ vs t (like those in Fig. 8) plotted for $\psi = 0.1$, $\delta_F = 500$ A°, and $q(t)^{\frac{1}{2}}$ = const. The ratio of the heat flux obtained for a film thickness of 500 A° (denoted as $q(0,t)_c$) to that obtained with no correction for film thickness (denoted as $q(0,t)_{gr}$) was computed for the assumed gage response curve in Fig. 9(a). This ratio is shown in Fig. 9(b). It is noted that the difference between the two heat flux values is not large except at early times and that the difference is less than 2% after about 5 μsec.

Finite coating thickness: Another influence on heat flux evaluation from gage response is that of a coating over a platinum film. Again only the case previously considered, that of a coating over a very thin film, will be

analyzed. In this case the gage response curve, Fig. 9(a), is that for a very thin film placed between the coating of thickness δ_c and the substrate. A coating thickness of 1000 A° is assumed, and as previously noted, the surface temperature $T(0,t)$ can be determined from Eq. (59) where cf for this case is approximated by the radio T_1/T_∞ for the 1000 A° coating, $\psi = 1$, $q(t)^{1/2}$ = const in Fig. 8. Heat flux values for the corrected and uncorrected gage response curve, Fig. 9(a), were computed. The curve for the ratio of these two quantities is presented in Fig. 9(b). It is noted that the heat flux ratio for this case is about the same as that for the case of an uncoated 500 A° platinum film on pyrex. However, thicker coatings yield larger values for the heat flux ratio.

Variation of substrate properties with temperature: An assumption in the analysis leading to Eq. (58) and then to Eq. (61) was that the substrate properties are constant. Since the substrate does undergo a change in temperature during testing, the accompanying change in substrate property variation could have an influence. This assumption has been examined and results are reported in Refs. 19 and 21. Fig. 11 summarizes the results for a platinum film on pyrex for two boundary conditions in terms of the ratio q_v, the heat flux computed using variable substrate properties, to q_p, the heat flux computed assuming constant substrate properties. The boundary conditions noted in Fig. 11 are approximately those for $\dot{q}(0,t)$ = const (boundary condition (a)) and heat flux prescribed by $q(0,t)\sqrt{t}$ = const (boundary condition (b)). The gage substrate surface temperature change encountered in shock tube flows over surfaces parallel to the flow direction such as that over a flat plate can be of the order of tens of degrees Centigrade. It can be seen from Fig. 11

that the variation of substrate properties should not be neglected. In general incorporation of variable substrate properties into a numerical procedure as was done in the preparation of the curves for Fig. 11 is a complex matter (see Refs. 19 and 21). Therefore it is desirable to have at hand a simple means for dealing with variable properties. A simple but accurate means of incorporating variable properties into the determination of heat flux involves use of Eq. (61), the results in Fig. 11, the temperature function $\tilde{Q}$, and a fictitious variation of substrate thermal conductivity k with temperature. Assuming a linear variation of k with T, $\tilde{Q}$ becomes

$$\tilde{Q}(0,t) = T(0,t) \left[1 + (S/2k_p) \, T(0,t) \right] \tag{61a}$$

where S is the slope of the k vs T curve. S = 0 corresponds to the constant substrate property case yielding $\tilde{Q} = T(0,t)$, which is the temperature variation with time that is used to compute the variation of heat flux with time for the constant properties case using Eq. (61). However, if $S/2k_p$ is taken as 0.0020/°C and if the temperature $\tilde{Q}(0,t)$ determined from Eq. (61a) is substituted for T(0,t) in Eq. (61), the resulting heat flux values when divided by the corresponding values computed assuming constant substrate properties will yield a curve q_v/q_p that is approximately an average of curves (a) and (b) in Fig. 11. Hence by use of the fictitious surface temperature change $\tilde{Q}(0,t)$ in Eq. (61), the effects of variable substrate properties on heat flux determination can be reasonably accounted for.

Summary of factors influencing heat flux determination.--Since several
factors have a bearing on evaluation of heat flux from gage response it is
of interest to present a summary with comments on the relative importance
of each.

¶ Definition of response curve: First and foremost it is essential that
the gage response be recorded and displayed in such a manner that the
response be clearly defined. The horizontal and vertical sensitivi-
ties of the oscilloscope should be selected to obtain as large a
trace as possible, consistent with the usable range of the oscillo-
-scope. Also the Polaroid photo of the trace and the oscilloscope grid
should be carefully taken. If early as well as late time evaluation
of the heat flux is to be made two oscilloscopes in parallel should be
used to display the gage response, one with a faster sweep time to
accurately define the early time portion of the response curve. Two
methods are available that work well for determining discrete values
from the response curve for heat flux evaluation. Use of an optical
reader which enlarges the trace and permits coordinates to be read
works well when available. A second satisfactory method consists
of making a transparent copy of the Polaroid photo of the gage
response and forming an enlarged image of the photo on graph paper
by means of a projector. The trace and grid are then transferred to
the graph paper and values that define the response curve are read
from the graph paper.

¶ Calibration: Calibration quantities related to the gage are Γ in
Eq. (57) and $\sqrt{(k\rho c)_s}$ in Eq. (61). Accurate determination of
these quantities is important since the heat flux is inversely propor-
tional and proportional respectively to these quantities. Experience

has shown that it is necessary to determine Γ for each individual gage. This is done by measuring resistance vs temperature for the gage using a constant temperature bath. As previously mentioned, the accepted value for $\sqrt{(k \rho c)}_g$ is 0.0737 Btu/ft^2 °F sec$^{\frac{1}{2}}$. Experience has shown that individual calibration of each gage to determine $\sqrt{(k \rho c)}_g$ is unnecessary.

Thin-film and coating thickness: After care has been taken to obtain good trace definition and proper calibration, corrections for film and coating thicknesses should be considered if very early times are of interest or if relative thick coatings or films are used. Although the combined influence of thickness of the film and coating together has not been analyzed, inferences can be made from the analysis of the individual effects. It is noted that the heat flux ratio curve for a platinum film on pyrex in Fig. 9(b) is for a film thickness of 500 A°, which is the approximate upper limit expected for film thickness. Therefore, the correction for platinum film thickness for most gages would be less than those inferred from Fig. 9(b) and would be negligible in practice except at very early times. However, when a coating is used, the coating thickness may not be negligible. This can be noted from the fact that the 1000 A° coating thickness assumed for Fig. 9(b) (pyrex on pyrex) represents the approximate lower limit of coating thickness necessary to protect the platinum film from ionization in the gas; and, as previously noted, coatings with thicknesses greater than 1000 A° yield heat flux ratio curves that are higher than the one in Fig. 9(b). This indicates that

significant errors may be introduced if corrections for the coating thickness (like those made using Fig. 8 for the example of Fig. 9) are not included. When corrections for film or coating thickness are applied, it is more important that the thickness be known than it is to know the nature of the surface heat flux variation with time.

Variable substrate properties: This influence is important only for large changes in surface temperature as noted in Fig. 11. However, as previously noted, the influence of variable substrate properties can readily be incorporated by use of the temperature function $\phi(0,t)$ from Eq. $(61a)$ (with $S/2k_p = 0.0018/^{\circ}C$) in place of $T(0,t)$ in Eq. (61).

An accurate assessment of the overall uncertainty involved in measuring heat transfer rates using thin film gages is difficult to make due to the large number of factors (and the uncertainty within these factors) that influence the results. However, estimates made on the basis of the method Kline and McClintock[25] and experience indicate that with reasonable care heat flux can be measured within $\pm 8\%$.

EXPERIMENTAL INVESTIGATION

Shock Tubes

Three shock tubes were employed in obtaining experimental data in this investigation. The important quantities related to the use of the shock tube in this study are the shock speed U_s and the initial temperature and pressure of the test gas. In all cases the initial test gas temperature was assumed to be room temperature. The following is a brief description of the three shock tubes used.

Iowa State Engineering Research Institute Shock Tube.--This shock tube is cold-gas driven and has a 3 in. x 6 in. rectangular cross section. The test model was located 30 feet from the diaphragm. Shock speeds are measured using microsecond interval counters which are triggered by the amplified output of thin-film transducers mounted flush with the tube side wall and positioned at 1 foot intervals just upstream of the test section. For the data taken in this investigation the initial test-gas pressure was measured using a Veco thermocouple-type vacuum gage which was calibrated using McLeod gages.

Three-Inch Combustion-driven Shock Tube.-- This shock tube is located at the NASA-Ames Research Center. It can be operated in either the cold-gas or combustion driven mode and has a circular cross section three inches in diameter. The test model was located 25 feet from the diaphragm. The shock speed was measured using microsecond interval counters which were triggered by the amplified output of pressure transducers spaced at known distances in the shock tube side wall. The initial test gas pressure p_1 was measured

by means of a Wallace and Tiernan bourdon-type absolute pressure gage in the range of about 5 torr and a McLeod gage for pressures in the range of about one torr.

Six-inch Arc-driven Shock Tube.--This shock tube is also located at the NASA-Ames Research Center. The test model was located 25 ft. from the diaphragm. Shock speeds were measured by means of ionization probes, associated electronics, and a microsecond counter. The probes were spaced 2 feet apart at a distance 1.5 upstream of the model. The desired initial test gas pressure p_1 was obtained using the gas-loading device which is an integral part of the shock tube facility. The gas-loading device was calibrated using a McLeod gage.

Models

Flat plate models were designed to completely span the shock tube except for a small clearance and were mounted in the tube with zero angle of attack with the plate test surface approximately on the tube centerline. Fig. 12 schematically displays the flat plate model design. The plate leading edge angle ω in Fig. 12 was chosen small enough to attach the leading edge shock. The leading edge radius was maintained at approximately 0.002 inches in order to minimize the disturbance of the flow over the plate upper surface caused by leading edge bluntness. The plate length was chosen consistent with the expected hot-flow testing times and the desire to obtain data over a wide range of the distance-time variable α. The important features of the plate models are listed in Table I.

Thin-film heat flux gages (see section on Heat Transfer Measurement) were positioned at two or more x locations, x_g, on the plate. These gages were in most cases prepared using substrate elements approximately 1/2" x 1" x 1/8" thick. Platinum films were applied by the painting and firing technique using Hanovia 05-x Platinum Bright. Three coats of Platinum Bright were applied to each gage. Table II lists the gages that were used to obtain the heat transfer rates presented in this report. Care was taken to mount the gages flush with the plate test surface in the manner noted in Fig. 12. Potting materials were used to fill any major surface imperfections in the region bordering the gages. In some tests heat flux gages were also mounted flush with the shock tube side wall to measure the heat flux through the side-wall boundary layer. This measurement was made to provide additional comparative data to verify plate heat transfer measurements in the region of the flat plate boundary layer (the M region) that is identical to that on the side wall.

TABLE I. FLAT PLATE MODELS

Plate No.	Width x Length	Gage Locations, x_g	ω, Fig 12(b)	Shock Tube	Plate Mounting Method
1	3 in. x 6 in.	35.5, 60.5, 86.5 mm	14°	NASA 3 in. I.S.U.	cantilevered from end wall
2	3 in. x 6 in.	52,77 mm	14°	NASA 3 in.	cantilevered from end wall
3	6 in. x 8 in.	Set A; 14.7 28.4, 75.4 mm Set B; 15.1 58.6, 89.9 mm	25°	NASA 6 in.	anchored by pins through side wall

TABLE II.   THIN FILM HEAT FLUX GAGES

Gage No.	Resistance R_0 ohms at $74^\circ F$	Γ, Eq.(57), $^\circ R^{-1}$	Coating	Use
2	56.3	0.00141	None	Plate 2, x_g = 52 mm
3	74.6	0.00142	None	Plate 2, x_g = 77 mm
15	111.6	0.00124	None	Plate 1, x_g = 35.5 mm
16	97.9	0.00131	None	Plate 1, x_g = 60.5 mm
17	116.8	0.00125	None	Plate 1, x_g = 86.5 mm
25	90.1	0.00125	SiO, $600 A^\circ$	Sidewall, ISU Shock Tube
40	124.8	0.00122	None	Sidewall, ISU Shock Tube
M4	106.2	0.00135	[a]SiO, $2000 A^\circ$	Plate 3, x_g = 14.7 mm
N3	203.9	0.00134	[a]SiO, $4000 A^\circ$	Plate 3, x_g = 58.6 mm
N4	157.2	0.00137	[a]SiO, $4000 A^\circ$	Plate 3, x_g = 88.9 mm
T3	142.0	0.00130	[c]Sapphire	Plate 3, x_g = 28.4 mm
T9	191.6	0.00135	[a]SiO, $2000 A^\circ$	Plate 3, x_g = 74.5 mm
V9	143.4	0.00133	[a]SiO, $4000 A^\circ$	Plate 3, x_g = 15.1 mm
02	106.3	0.00140	[b]SiO, $900 A^\circ$	Plate 1, x_g = 35.5 mm
V7	160.0	0.00135	[c]Sapphire	Plate 1, x_g = 35.5 mm
V8	155.0	0.00135	[c]Sapphire	Plate 1, x_g = 60.5 mm

[a]Placed in oven for 16 hrs. at $900^\circ F$ to oxidize SiO to SiO_2.

[b]Placed in oven for 6 hrs. at $900^\circ F$ to oxidize SiO to SiO_2.

[c]Thickness unknown.

Data Analysis

For a given shock tube test the following data were obtained:

1. The initial pressure and temperature, p_1 and T_1, for the test gas.

2. The shock speed U_s.

3. Oscilloscope records of the response of each thin-film heat-flux gage.

Using these data and appropriate calibration quantities, experimental values of Q_x vs α were computed in order to make comparisons with the corresponding theoretical values of Q_x vs α (Fig. 3) determined for the particular shock tube test. Experimental values of Q_x vs α were computed by Eq. (53) which may be written as

$$Q_x(\alpha) = \frac{q_w \sqrt{x}\ \sigma_w}{\sqrt{\left(\frac{\rho_o}{\rho_1}\right)\rho_1\ \left(\frac{\mu_o}{\mu_1}\right)\mu_1\ u_o}\ \left(\frac{h_o}{h_1}\right)h_1}$$

or

$$Q_x(\alpha) = \frac{q_w \sqrt{x}\ \sigma_w}{\sqrt{\frac{P_1}{RT_1}\ \frac{\mu_1\ u_o}{C_w}}\ \left(\frac{h_o}{h_1}\right)h_1} \tag{62}$$

The sources of the various quantities in Eq. (62) are discussed below.

Heat transfer rates $q_w = q_w(t')$ at each gage location $x = x_g$ were determined from gage response recorded by oscilloscopes using the numerical method of Eq. (61) and the response curve definition techniques described under Definition of response curves in the section of this report dealing with heat flux measurement. Note that t in Eq. (61) must be interpreted as t', where t' is zero when the shock arrives at the gage. The resistance-temperature quantity Γ in Eq. (57) was determined for each heat flux gage

using measured values of gage resistance vs temperature. The variation in gage substrate properties was accounted for using the previously-described method embodied in Eq. (61a).

Corrections for the platinum film thickness were not made to gage response curves since as previously noted the error involved in ignoring the film thickness appears to be quite small. However, as noted in the discussion of Fig. 9b, neglecting the presence of the coatings might lead to larger errors. Therefore the presence of the coating was not neglected. The influence of the coatings on gage response could not be accounted for in an exact manner for two reasons. First, only the approximate thickness of the coatings (as indicated by the thickness monitor on the vacuum deposition apparatus) were known. A profilometer was not available to measure the coating thickness. Second, the nature of most of the coatings used was not known with certainty. As noted in Table II, two materials were used in coating the gages: SiO and sapphire. Most of the results presented in this report where coated gages were used were obtained using gages coated with SiO. Although sapphire has desirable thermal characteristics and appears to offer good protection against ionization effects in the flow, it was not used extensively due to difficulties encountered in obtaining bonding of the sapphire coatings to the gage. The gages with SiO coatings were placed in an oven to oxidize the SiO to SiO_2. Evidence exists (Ref. 26) that SiO coatings in excess of 1000 A^o in thickness never completely oxidize due to the formation of a crust of SiO_2 that inhibits oxidization of the remainder of the coating. Therefore due to the uncertainties in both thick-nesses and the nature of the SiO coatings and the absence of other information the following assumptions were made: the thicknesses listed in Table II

were correct, and the thermal properties of the coatings were those of

pyrex. Corrections for the sapphire coatings were not made in the two

instances where such coatings were used, because, due to the desirable

thermal characteristics of the sapphire, corrections appear to be unnecessary.

With these assumptions, values for the coating correction factor cf for Eq. (59)

were determined from curves with $\psi = 1$ and $q\sqrt{t}$ = const (like those in Fig. 8)

plotted for the given coating thickness. This correction coupled with the

correction associated with variable properties for pyrex constituted

the two corrections that were incorporated into the determination of heat

transfer rates. A further assessment of the influence of these corrections

on experimental results is made later in this report.

The values p_1 and T_1 in Eq. (62) are the measured values for the initial

pressure and temperature of the test gas and $u_o = U_s/A$, where $A = (\frac{\rho_o}{\rho_1})/(\frac{\rho_o}{\rho_1} - 1)$.

The quantity $C_w = \rho_w \mu_w / \rho_o \mu_o$ was determined from real-gas

thermodynamic and transport property relations for the test gas. The ratio

h_o/h_1 is the enthalpy ratio across the shock and is determined from the

appropriate real gas normal shock chart using the measured values for U_s, p_1

and T_1. μ_1 is the viscosity of the test gas evaluated at T_1, and σ_w is

the Prandtl number at $T_w = T_1$. ρ_o/ρ_1 was also determined from the

appropriate normal shock chart.

Values of α corresponding to the Q_x values determined from Eq. (62) are

$$\alpha = \frac{x}{u_o t} = \frac{x_g A}{U_s(t' + x_g/U_s)} = \frac{x_g A}{U_s t' + x_g} \tag{63}$$

Thus Eqs. (62) and (63) yield Q_x and corresponding α values at each gage

location that can be compared with theoretical predictions for Q_x vs α.

As noted previously, the theory for the boundary layer under consideration

predicts a single curve Q_x vs α for all x locations on the plate. Therefore the gages located at several x_g values provide data for verification of this key aspect of the theory.

RESULTS AND DISCUSSION

Shock tube experiments were carried out in this investigation that produced experimental heat transfer data for gas flows induced by shocks with speeds ranging from 1.695 to 7.34 km/sec. Air and nitrogen were used as test gases. Experiments with air were carried out for shock speeds ranging from 1.695 to 2.83 km/sec. All heat transfer measurements made in air were made with uncoated thin-film heat-flux gages. At shock speeds greater than about 3 km/sec in air or nitrogen, ionization of the test gas induces spurious gage response signals when uncoated gages are used. Experiments with nitrogen as the test gas were carried out using coated gages for shock speeds ranging from 3.16 to 7.34 km/sec. The results obtained for each test gas will be presented and discussed separately.

Experiments in Air (Uncoated Heat-flux Gages)

The results of the experiments with air as the test gas are compared with theoretical predictions in Figs. 13 to 22. These tests were made using the Iowa State shock tube and the NASA 3 inch shock tube. The theoretical curves for Q_x vs α in these figures were determined using the ratios from Fig. 4 and Eqs. (54) and (55). The steady state Q_x value, Eq. (32), and Q_x at $\alpha = 1$ for Eq. (34) were determined from Fig. 5 for shock speeds below 2 km/sec. For higher shock speeds these quantities were obtained by solving Eqs. (22) and (23) for each case using the Prandtl number variation from Ref. 8 and the $\rho\mu$ variation from Ref. 9. This was necessary because the pressure behind the shock at the higher shock speeds differed considerably from the pressure of one atmosphere to which Fig. 5 is limited.

The theoretical curves Q_x vs α in Figs. 13 to 22 are strictly applicable only for the condition $U_s t \leqq L$, i.e., the flow-initiating shock wave (Fig. 1a)

remains on the plate. For a given heat flux gage, the value of t' at which
the shock reaches the trailing edge of the plate is $t_L^i = (L - x_g)/U_s$. (See
Fig. 12) The corresponding value α_L can be found from Eq. (63). The
condition $U_s t = L$ is denoted by the half-filled symbol in Figs. 13 to 22.

A heat flux gage response record for the tests made in air is shown in
Fig. 23a. This record, which was obtained in Run C 142 for gage 15 (Fig. 22)
at a shock speed of 2.83 km/sec, is typical of those obtained for the air
tests and shows no significant influence from ionization in the flow.
For runs made at appreciably higher shock speeds, ionization of the
air rendered the gage response signals useless. The region 2 testing times
as determined by examining the gage response records were in most cases
appreciably longer than t_L^i for the gage nearest the leading edge of the
plate.

Fig. 13 presents results for a shock speed of 1.695 km/sec. The extended
theoretical steady state and M region solutions are shown for purposes
of comparison with the theoretical interaction region solution. The experi-
mental results generally agree well with the theory at lower values of α,
but tend to disagree with the theory at larger values of α. Fig. 14(a) shows
a similar behavior for comparison of experimental results and theory for a
case with $U_s = 1.966$ km/sec. Examination of Eq. (63) indicates that for a
given case, small values of t' correspond to large values of α. Thus the
region of disagreement in Figs. 13 and 14(a) corresponds to small t'. It is
therefore of interest to examine the heat transfer results in terms of t'.
Fig. 14(b) presents dimensional heat transfer results for Run N010, Fig. 14(a),
as a function of t'. Simultaneous to measurement of the plate heat

transfer presented in Fig. 14(a), the side wall heat flux was measured in
Run N 010. As indicated by Eq. (30), $q_W(t')^{1/2}$ = const for the side wall
boundary layer. The theoretical value of $q_W(t')^{1/2}$ for Run N 010 is indicated
in Fig. 14(b). Also shown are experimental values of $q_W(t')^{1/2}$ determined from
the response of thin film heat flux gage 40 which was mounted flush with the
side wall of the shock tube. Agreement of these values with theory is very good
after the first few microseconds. Experimental values of $q_W(t')^{1/2}$ as indicated
by plate gages 15 and 16 for Run N 010 are also shown in Fig. 14(b). These
values are of interest because, according to theory, the heat flux measured
by the plate gages should be identical to that for the side wall boundary
layer for small values of time after the shock passes over the plate gages, i.e.,
small values of t'. At $t' = (x_g/U_s)/(A-1)$, i.e., at $\alpha = 1$, the side wall region
(the M region) terminates and the interaction region begins. For somewhat larger
values of t' (values of α less than unity) the theoretical solution is
essentially that for the extended M region boundary layer. With still larger
values of t' (smaller α) the solution for the heat flux should depart from the
value of $q_W(t')^{1/2}$ for the side wall. This behavior is exhibited for t'
greater than about 15 μsec in Fig. 14(b) by the experimental heat transfer
rates indicated by plate gages 15 and 16. For a short time interval after
the first few microseconds the two plate gages indicate values of $q_W(t')^{1/2}$
that are in very good agreement with the side wall theory. With increasing
t', $q_W(t')^{1/2}$ values from gage 15 (the gage nearest the plate leading edge)
depart as expected from the side wall theory and are followed by those
indicated by gage 16.

Values of t' at which the M region terminates are indicated in Fig. 14(b) for both plate gages. It is seen from both Figs. 14(a) and 14(b) that the M regions terminate prior to the time t' at which experimental and theoretical M region values for $q_w(t')^{\frac{1}{2}}$ agree. For small values of t' (less than about 10 μsec), the experimental values of $q_w(t')^{\frac{1}{2}}$ indicated by the three gages are in good agreement but are larger than the theory predicts. The reason for this behavior is related in part to early time errors in the numerical method of Eq. (61) and to difficulties encountered in defining both the zero for t' and the shape of the gage response trace at small values of t'. It should be noted that errors of this nature tend to rapidly diminish as time increases and therefore do not significantly influence the experimental results at larger values of time.

Fig. 14(b) also presents for Run N 010 a comparison of the theoretical steady state value for $q_w(x)^{\frac{1}{2}}$, which according to Eq. (53) is constant, and experimental values for $q_w(x)^{\frac{1}{2}}$ determined from the heat flux indicated by gages 15 and 16. The experimental results for both gages approach the steady state theoretical value of $q_w(x)^{\frac{1}{2}}$ as time increases and the experimental values agree well with the theory at steady state. This comparison of results as steady state is approached is interesting but not as universal as the comparison in terms of Q_x and α in Fig. 14(a).

Figs. 15(a) and 15(b) present results for a shock speed of 2.35 km/sec in a manner similar to those in Fig. 14(a) and 14(b). The results as presented in Fig. 15(a) are in good agreement with the theory. As noted in Fig. 15(b),

a side wall gage was employed to measure the side wall heat flux. Again, except for the first few microseconds, good agreement exists between the theoretical M region value for $q_w(t')^{\frac{1}{2}}$ and the experimental values for that quantity indicated by each of the three gages. For the time interval shown in Fig. 15(b) only the heat flux quantity for plate gage 15, the gage nearest the leading edge, indicates an influence of the interaction region.

Figures 16 to 22 present results for the remainder of the shock speed range covered in this investigation using air as the test gas. In these figures experimental results are presented only for values of α corresponding to t' values larger than the times at which experimental values of $q_w(t')^{1/2}$ constant with t'. With the exception of Fig. 16, 18(a) and 20, the experimental results are observed to be in good agreement with the theory. In Figs. 16, 18(a) and 20 the experimental results generally fall somewhat above the theoretical curves. It is believed that this disagreement is due to errors associated with the experimental phase of the investigation rather than a failure of the theory to properly predict variation of Q_x with α. Possible sources of experimental error are numerous, but those believed to be involved here are errors in voltage measurement and those involved with measuring the initial pressure p_1 of the test gas. The initial pressure of the test gas appears as $1/(p_1)^{\frac{1}{2}}$ in Eq. (62) which was used to compute experimental values of Q_x. Vertical scale calibration of the oscilloscope affects the voltage quantitites in Eq. (57) that relate to the determination of the gage substrate surface temperature change T(0,t), which in turn is used in the computation of heat flux by Eq. (61). Errors

in voltage measurement are directly related to errors in heat flux, i.e., a 10% error in voltage measurement results in a corresponding 10% error in heat flux. Evidence that a fixed experimental error is involved with the disagreement in Figs. 16, 18(a), and 20 is obtained from the results for Run C 137, Fig. 18(a), as presented in Fig. 18(b). The results in this figure were obtained by multiplying the corresponding experimental Q_x quantities in Fig. 18(a) by the ratio of the theoretical to experimental Q_x, the ratio being determined at low values of α for each gage. This results in good agreement of experimental results with theory at larger values of α as can be seen in Fig. 18(b). The results in Figs. 16 and 20 exhibit the same trends as those in Fig. 18(a) and when modified in a manner similar to those in Fig. 18(b) also show good agreement with theory thereby providing additional evidence that fixed experimental errors are involved in the results of Figs. 16, 18(a), and 20.

The comparison of results for shock speeds ranging from 2.35 to 2.83 km/sec in Figs. 15 to 22 are for higher shock speeds than those obtained by Felderman[5,6] using air as the test gas.

Experiments in Nitrogen (Coated Heat-flux Gages)

The results of experiments performed with nitrogen as the test gas are compared with theoretical heat transfer predictions in Figs. 24 to 32. These experiments cover a range of shock speed from 3.16 to 7.34 km/sec, and were carried out using two shock tubes, the 3 inch NASA shock tube (combustion driven) and the NASA 6 inch arc-driven shock tube. Figures 24 and 25 present results obtained using the 3 inch shock tube while Figs. 26 to 32 report the results obtained for the 6 inch shock tube. In two instances more than one run was made at essentially the same shock speed. These cases are reported in Figs. 30(a) and (b) and in Figs. 31(a), (b) and (c). Results in the form $q(x)^{\frac{1}{2}}$ vs t' are shown for two selected cases in Figs. 28(b) and 32(b).

The theoretical curves Q_x vs α in Figs. 24 to 32 were obtained in a manner similar to that previously discussed for air in Figs. 13 to 22. The steady state and M region values for Q_x (Eqs. (32) and (34) respectively) were first obtained by numerically solving Eqs. (22) and (23) for both the steady state and M regions. The property ratios across the incident shock and the variation of properties with enthalpy for nitrogen required for these solutions were determined at the appropriate pressure from the charts and tables for equilibrium nitrogen presented by Ahtye and Peng, Ref. 27. A given curve Q_x vs α was then constructed using the method related to Fig. 3 and Eqs. (54) and (55). The ratios R_{ss} and R_M were obtained from Fig. 4. Fig. 4 is strictly applicable only to air at $p_o = 1$ atm. However, the results obtained using this figure for nitrogen should be acceptable first, because the denominators of Eqs. (54) and (55) were accurately determined for nitrogen, and second, due to the similarities between nitrogen and air, the ratios R_{ss} and R_M for nitrogen would not be expected to differ significantly from those

for air. Use of Fig. 4 for nitrogen eliminated the lengthy and expensive procedure required to solve the governing equations for the unsteady interaction region, Eqs. (49) and (50), which lead to Eq. (52).

Figures 23b to 23f show representative heat flux gage response records for the tests in nitrogen. Gage coatings for the gages noted are described in Table II. All records in this group except Fig. 22b show some influence of ionization of the nitrogen on the gage signal. This influence is evident in two respects. First, precursory ionization influences the signal prior to arrival of the shock at the gage as evidenced by the down-going portion of the trace prior to shock arrival in Figs. 23 d, e, and f to a smaller extent in Fig. 23c. Second, there is some influence of ionization immediately after shock arrival, and to a lesser extent at later times. These effects are particularly evident in Fig. 23f in which the effects of precursory ionization prior to shock arrival and the somewhat eratic signal after shock arrival both exist to a significant extent.

Figures 23b to 23f illustrate the degree to which various oxidized SiO coatings provide protection against ionization. The coating for gage 02 (900 A^o SiO oxidized 6 hrs. at 900°F) provided excellent protection at the flow conditions noted in Fig. 23b. However, at appreciably higher shock speeds eratic signals resulted from gage 02. Gage V9, 4000 A^o SiO coatings oxidized 16 hrs. at 900°F, gave relatively noise-free response (Figs. 23 c, d, and e) as compared to the response of gage M4, Fig. 23f, which was prepared in a similar manner except the thickness of the SiO was 2000 A^o. The flows related to Figs. 23e and 23f involved about the same level of ionization since the shock speed and pressure level was about the same. The response curves of gage V9 are typical of the response curves of the gages that were used to obtain most of the heat flux data for nitrogen flows. Due to the ionization

effects on gage response in the immediate vicinity of the shock, heat transfer results at very early times after shock arrival at the gage were not considered to be reliable.

Termination of region 2 shock tube flow is in many cases evident from the response of heat flux gages. Figures 23d, e, and f clearly show this. The eratic signal recorded just prior to the smooth declining segment of the response curve is interpreted to be due to the arrival of the contact front that forms between the test and driver gases. In view of the relatively short testing times associated with high shock speeds, a comparison of the region 2 testing time with the time required for the shock to reach the trailing edge of the plate is of interest. Figure 33 presents such a comparison for the range of shock speeds covered in tests with Plate 3 (see Table II) mounted in the 6 inch arc-driven shock tube. The testing times were taken as the time between shock arrival and interface arrival at the front gage on the plate. Values of $t_L' = (L-x_g)/U_s$ for the front gage ($x_g = 15.1$ mm) are also shown in the Figure. Since the testing time is somewhat greater than t_L' for the full range of shock speed shown it was concluded that region 2 was of greater length than the plate and that times up to at least t_L' for each gage involved region 2 flow over the whole plate.

With a few exceptions the experimental heat transfer results presented in Figs. 24 to 32 exhibit good agreement with theoretical predictions for the range of α shown. Results are not presented in some cases for values of corresponding to t' values less than about 5 μsec because of uncertainty regarding the gage response configuration at early times due to ionization effects in the vicinity of shock wave arrival. Small values of t' correspond to large values of α (see Eq. (63)). Accordingly, this eliminated some data at large values of α for each gage location. Of the twelve comparisons

of Q_x vs α, Figs. 26, 30(a), and 32(a) tend to exhibit experimental

results somewhat above the theory, while in Figs. 31(a), (b), and (c) the

results tend to fall below the theory. In the remaining six figures the

experimental results generally agree well with the theory. Agreement between

the results indicated by different gages varies from quite good in Fig. 28(a)

to fair in Fig. 31(b). In Figs. 26 to 32 Gage V9 (the front gage) tends to

yield results a few percent below the other two gages. Figure 34 presents a

comparison of experimental steady state values of Q_x with theoretical steady

state Q_x values for the range of shock speeds covered using nitrogen as the

test gas. In this figure only experimental results for those gages

indicating a steady heat flux with time are shown. These results agree with

theory within about $\pm$ 10%.

As previously noted the theoretical curves Q_x vs α are strictly

applicable only as long as the shock remains on the plate, i.e., $t \leq L/U_s$,

and correspondingly, $t' \leq (L - x_g)/U_s$. The half-filled symbols for the experi-

mental results for nitrogen in Figs. 24 to 32 and for air in Figs. 13 to 22

indicate the condition $t \approx L/U_s$. In many of these figures this condition

occurs at values of α in the unsteady interaction region. Experimental

results at values of α smaller than those corresponding to the half-filled sym-

bols are then related to conditions that exist after the shock has reached the

end of the plate. Experimental results at these lower values of α are shown

in the figures down to values of α at which a significant departure from

the trend of the results occurred. In many cases this departure corresponded

to the termination of the available test time. Thus the theory for the

unsteady laminar boundary layer presented here continues to predict the plate

heat transfer for times significantly longer than $t \approx L/U_s$.

Figures 28b and 32b present results in the form $q_w \sqrt{x}$ vs t' for two

typical shock speeds; one at an intermediate speed of 4.59 km/sec (fig. 28b)

and the other at the highest shock speed investigated, 7.34 km/sec (Fig. 32b).

Experimental results are shown only for those heat flux gages which indicated

steady state heat flux values. The apparent "noise" is due mostly to the

date reduction technique. Typical influence of the two corrections applied

in reducing the thin film gage response data is illustrated in these figures

for gage V9. The correction for the coating has the largest influence at

small values of t', while the variable substrate properties correction is

related to temperature through t' and increases with t' since surface tempera-

ture increases with t'. Both corrections are of the order of a few percent

in Fig. 28b. Ignoring the corrections would lower the results by 8 to 10

percent. In Fig. 32b the variable substrate properties correction is larger

due to the larger change in substrate surface temperature accompanying the

higher heat flux encountered for the higher shock speed. Ignoring the

corrections here would yield results about 15% lower. Although both of the

corrections made are approximate, they seem to be justified by the experimental

results.

CONCLUDING REMARKS

The comparisons of theoretical and experimental heat transfer rates made for the range of shock speeds covered in this study generally verify the theory of the shock-induced unsteady laminar boundary layer on a flat plate as presented here and in Ref. 1. In particular, the results confirm the self similarity that is revealed by the theoretical analysis, namely that the wall heat transfer and other boundary layer quantities can be formulated in terms of the time-position variable α alone. The theory might be expected to predict the boundary layer behavior only for the time interval during which incident shock remains on the plate. However, the experimental results indicate that the theory continues to predict the boundary layer behavior for significantly longer intervals of time.

Although some difficulties were encountered in measuring heat transfer rates at values of α in the vicinity of unity, the heat transfer measurement technique employed was generally satisfactory. In the cases where measured heat transfer rates differed to a pronounced degree with the theory, there is evidence that the difference was due to some fixed error in an experimentally measured quantity rather than in a gross failure of the theory to predict the heat transfer rates. Some refinements are needed in the heat transfer measurement technique, particularly in those related to measurement of heat flux at higher shock speeds where test gas ionization influences the performance of thin-film heat flux gages. Development of gage coatings to provide protection against high levels of ionization and interpretation of coated gage response to determine heat transfer rates should be the subject of further investigation.

Finally, the experimental results of this investigation confirm that under certain conditions steady flow can readily be attained over models

mounted in shock tubes, even for short-duration flows generated by high speed shocks. This fact coupled with the technique described here for measuring time dependent heat flux makes feasible experimental heat transfer studies for both laminar and turbulent boundary layer flows over models under conditions of high wall cooling and low supersonic free-stream Mach numbers.

REFERENCES

1. Cook, William J. and Chapman, Gary T., "Characteristics of the Unsteady Shock-Induced Laminar Boundary Layer on a Flat Plate," to be published in The Physics of Fluids, December, 1972.

2. Lam, S. H., "Shock Induced Unsteady Laminar Compressible Boundary Layer on a Semi-Infinite Flat Plate," Ph.D. thesis, 1958, Dept. of Aeronautical Engineering, Princeton University, Princeton, New Jersey.

3. Lam, S. H. and Crocco, L., "Note on the Shock-Induced Unsteady Laminar Boundary Layer on a Semi-Infinite Flat Plate," Journal of Aero-Space Sciences, Vol. 26, 1959, pp. 54-56.

4. Lam, S. H., "Numerical Solutions of Shock-Induced Unsteady Boundary Layers," Princeton University Report, No. 480, August, 1959, Princeton, New Jersey.

5. Felderman, E. J., "Heat Transfer and Shear Stress in the Shock-Induced Unsteady Boundary Layer on a Flat Plate," AIAA Journal, Vol. 6, No. 3, 1968, pp. 408-412.

6. Felderman, E. J., "Heat Transfer in the Shock-Induced Unsteady Boundary Layer on a Flat Plate," Ph.D. thesis, 1966, Iowa State University, Ames, Iowa.

7. Cook, W. J., Tu, D., and Felderman, E. J. "Solution of Certain Laminar Boundary Equations for Dissociated and Ionized Gas Flows by the Crocco Method," Unpublished paper, Dept. of Mechanical Engineering, Iowa State University, ca. 1970.

8. Hansen, C. Frederick, "Approximations for the Thermodynamic and Transport Properties of High Temperature Air," NACA TR R-50, 1959.

9. Mirels, H., "Laminar Boundary Layer Behind a Strong Shock Moving into Air," NASA TN D-291, 1961.

10. Viegas, John R. and Howe, John T., "Thermodynamic and Transport Property Correlation Formulas for Equilibrium Air from $1,000^\circ$ K to $15,000^\circ$ K," NASA TN D-1429, 1962.

11. Unpublished Normal Shock Charts for Equilibrium Air, NASA Ames Research Center, Moffett Field, California.

12. Feldman, S., "Hypersonic Gas Dynamic Charts for Equilibrium Air," Avco Report No. 40, Avco Research Laboratory, Everett, Mass. 1957.

13. Laird, J. D. and Heron, K., "Shock Tube Gas Dynamic Charts, Part I: Equilibrium Argon-Free Air from 3000 to $40,000^\circ$ K," Avco/RAD TM 64-12, April 10, 1964.

14. Vidal, R. J., "Model Instrumentation Techniques for Heat Transfer and Force Measurements in a Hypersonic Wind Tunnel," Rept. AD-917-A-1, WADC TN 56-315, Feb. 1956, Cornell Aeronautical Lab, Inc., Cornell University, Buffalo, N. Y.

15. Marrone, P. V., and Hartunian, R. A., "Thin Film Thermometer Measurements in Partially Ionized Shock-Tube Flows," Physics of Fluids, Vol. 2, No. 6, Nov.-Dec., 1959.

16. Carslaw, H. S. and Jaeger, J. C., Conduction of Heat in Solids, 2nd ed., Oxford University Press, London, 1959.

17. Kurzrock, John W., "Selection of Surface Thermometers for Measuring Heat Flux," Cornell Aeronautical Lab. Report CAL - 124, February, 1963.

18. Camac, M. and Feinberg, R., "High Speed Infrared Bolometer," Avco-Everett Research Labs, Research Report 120, March, 1962.

19. Cook, W. J., "Unsteady Heat Transfer to a Semi-Infinite Solid with Arbitrary Surface Temperature History and Variable Thermal Properties, TR ISU-ERI-Ames 67500, 1970, Engineering Research Institute, Iowa State University, Ames, Iowa.

20. Cook, W. J. and Felderman, E. J., "Reduction of Data from Thin-Film Heat-Transfer Gages; A Concise Numerical Technique," AIAA Journal, Vol. 4, No. 3, March 1966, pp. 561-562.

21. Cook, W. J., "Determination of Heat Transfer Rates from Transient Surface Temperature Measurements," AIAA Journal Vol. 8, No. 7, July 1970, pp. 1366-1368.

22. McCaa, D. J., "Measurement of Film Thickness of Thin-Film Resistance Thermometers," AIAA Journal, Vol. 6, No. 4, April 1968, p. 747.

23. Hartunian, R. A. and Varwig, R. L., "On Thin-Film Heat-Transfer Measurements in Shock Tubes and Shock Tunnels," Physics of Fluids, Vol. 5, 1962, pp. 169-174.

24. Bogdan, Leonard, "High-Temperature Thin-Film Resistance Thermometers for Heat Transfer Measurement," NASA CR-26, 1964.

25. Kline, S. J. and McClintock, F., "Describing Uncertainties in Single Sample Experiments," Mechanical Engineering, Vol. 75, pp. 3-8, 1953.

26. Holland, L., Vacuum Deposition of Thin Films, John Wiley and Sons, Inc., New York, pp. 483-89.

27. Ahtye, Warren F. and Peng, Tzy-Cheng, "Approximations for the Thermodynamic and Transport Properties of High-Temperature Nitrogen with Shock-Tube Applications," NASA TN D-1303, 1962.
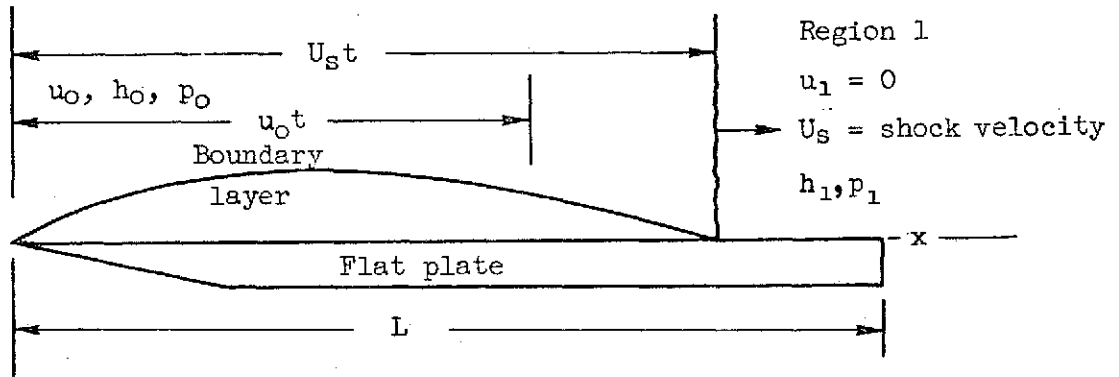
(a) The shock-induced laminar boundary layer on a flat plate.
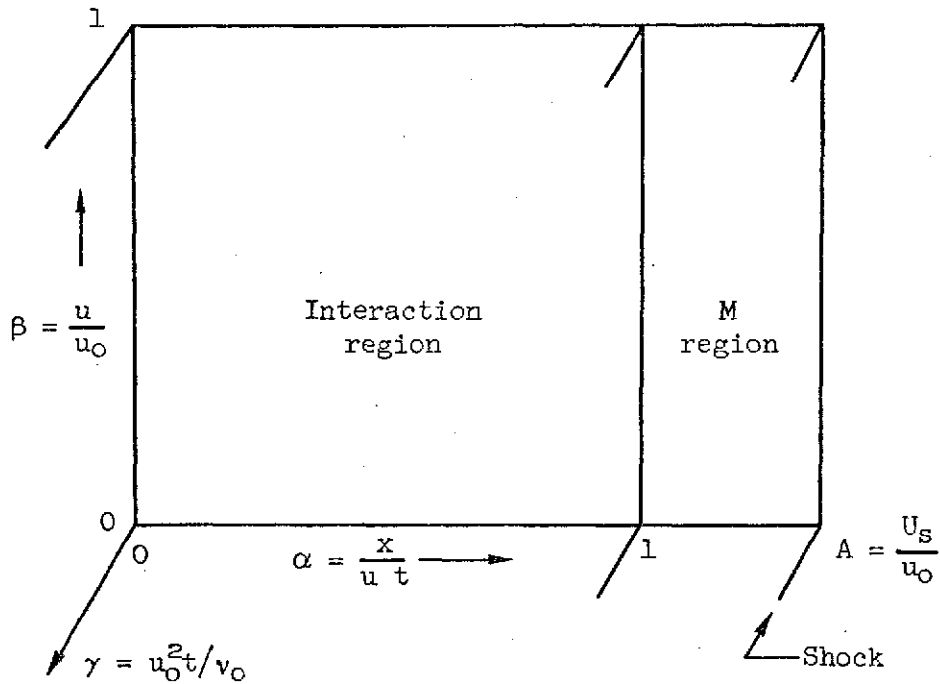
(b) The coordinates of Lam and Crocco for the unsteady shock-induced
laminar boundary layer on a flat plate.

Figure 1.- Nomenclature for the shock-induced laminar boundary layer on
a flat plate.
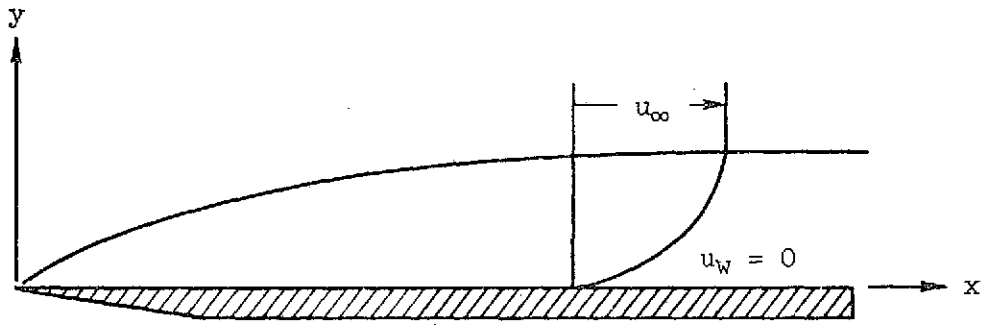
(a) The steady boundary layer on a flat plate.
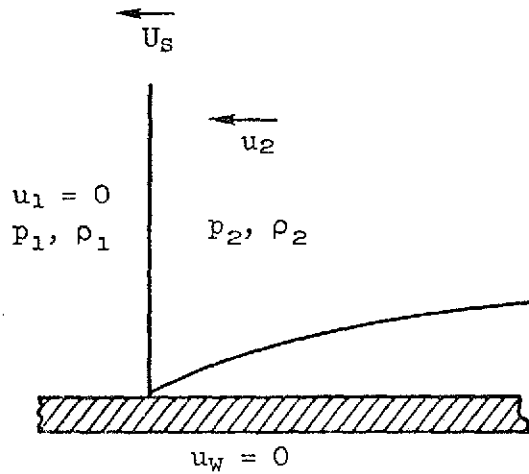
(b) M region boundary layer in wall-fixed coordinates.
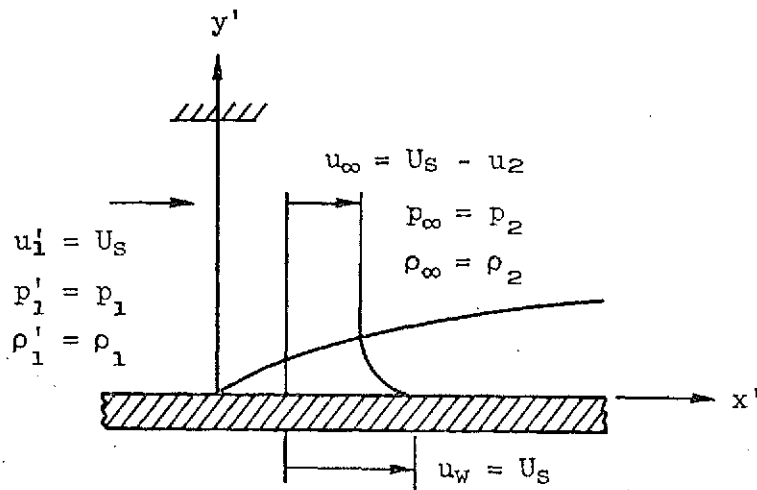
(c) M region boundary layer in shock-fixed coordinates.

Figure 2.- The steady and M region boundary layers.
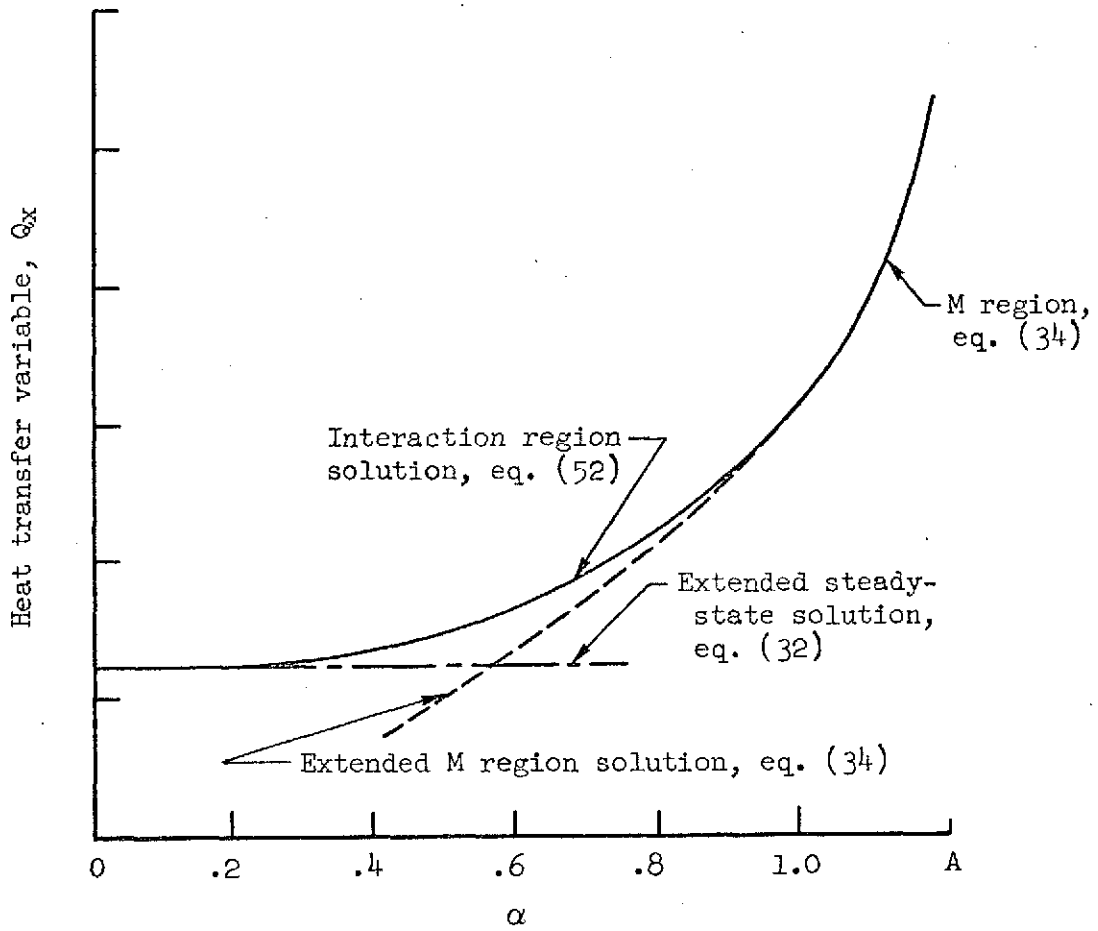
Figure 3.- Typical solution for Q_x vs α.
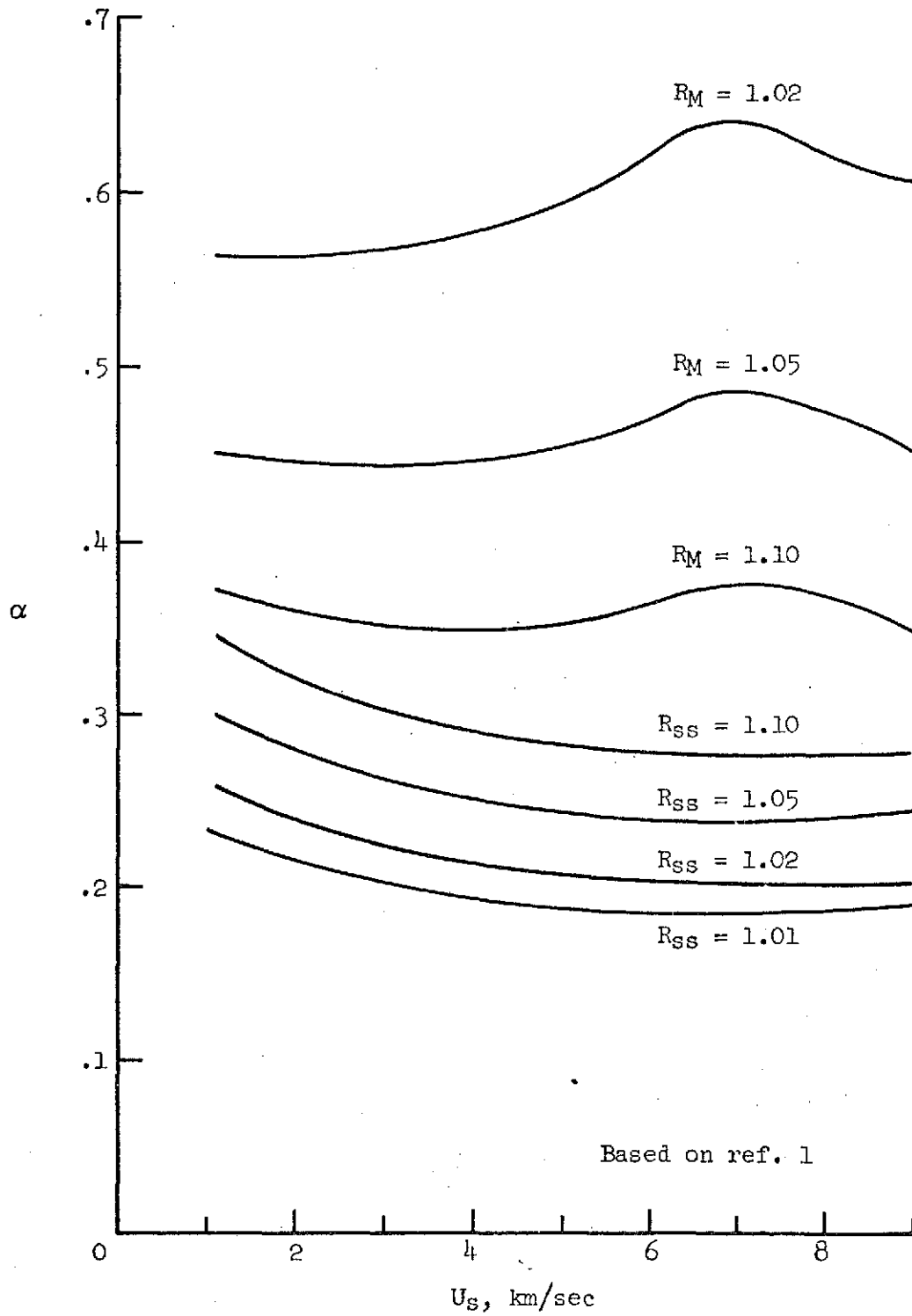
Figure 4.- Ratios R_{SS} and R_M, eqs. (54) and (55), in terms of U_S and α; $p_O = 1$ atm, equilibrium air.
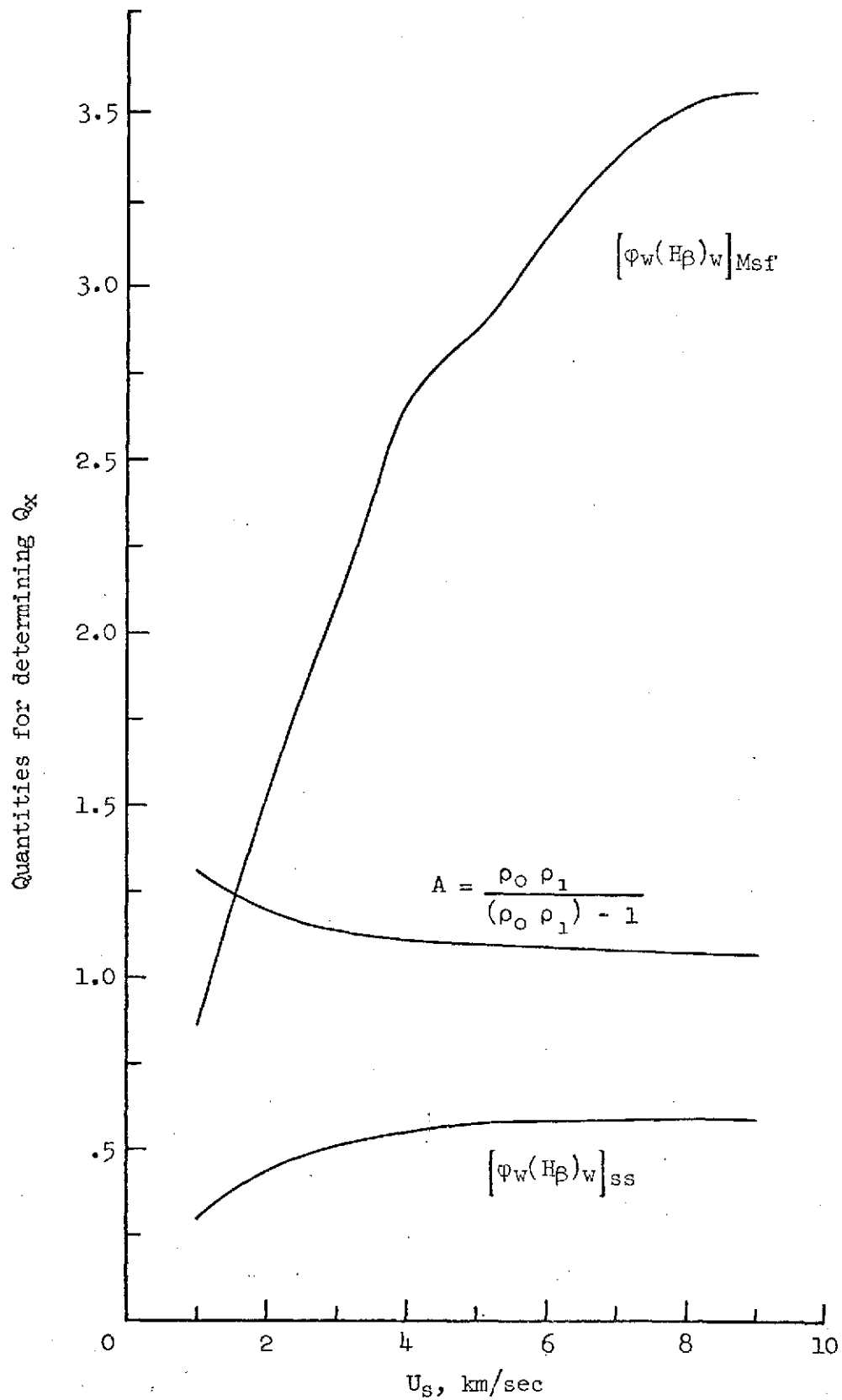
Figure 5.- Quantities for determining Q_x at $p_O = 1$ atm using eqs. (32) and (34); equilibrium air.

Oscilloscope with Polaroid camera

Oscilloscope lead wires

Heat flux

δ_C

A

Coating

Platinum film

A

δ_F

Substrate
(semi-infinite)

x

Lead wires

I_o

Ballast resistor

Battery

Coating

film

W

$(W \gg \delta_F)$

Section A-A
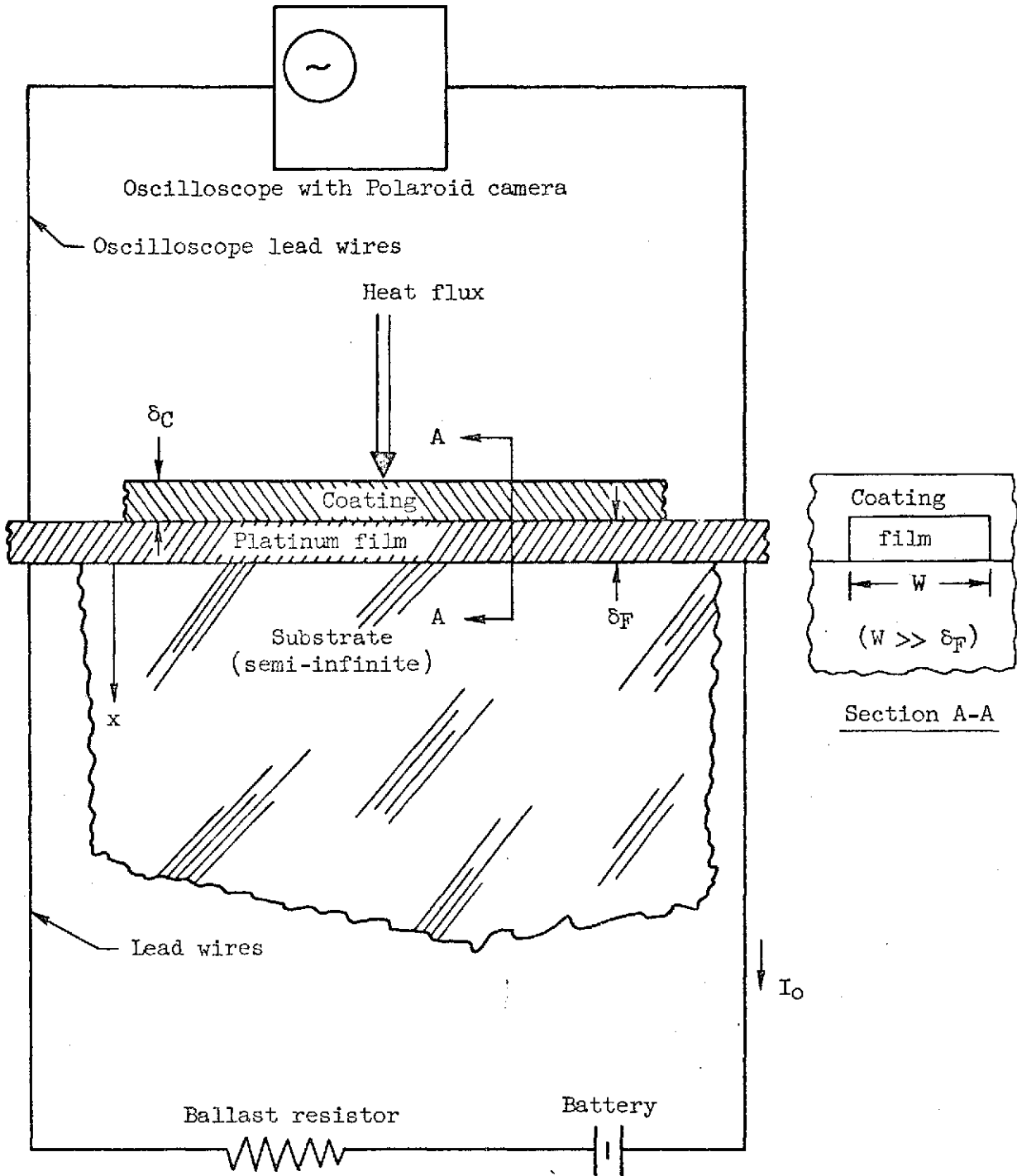
Figure 6.- Schematic diagram of the thin-film heat flux gage.

T_I/T_∞

$\psi = 1.0 \left(\text{pyrex on pyrex}\right)$

$\psi = 0.1 \ (\text{platinum on pyrex})$

———— Constant surface heat flux, ref. 17

– – – – Approximate curves based on appendix A, ref. 18 for surface heat flux $= \text{const}/\sqrt{t}$

$\bar{\theta} = \alpha_F t/\delta_F^2$
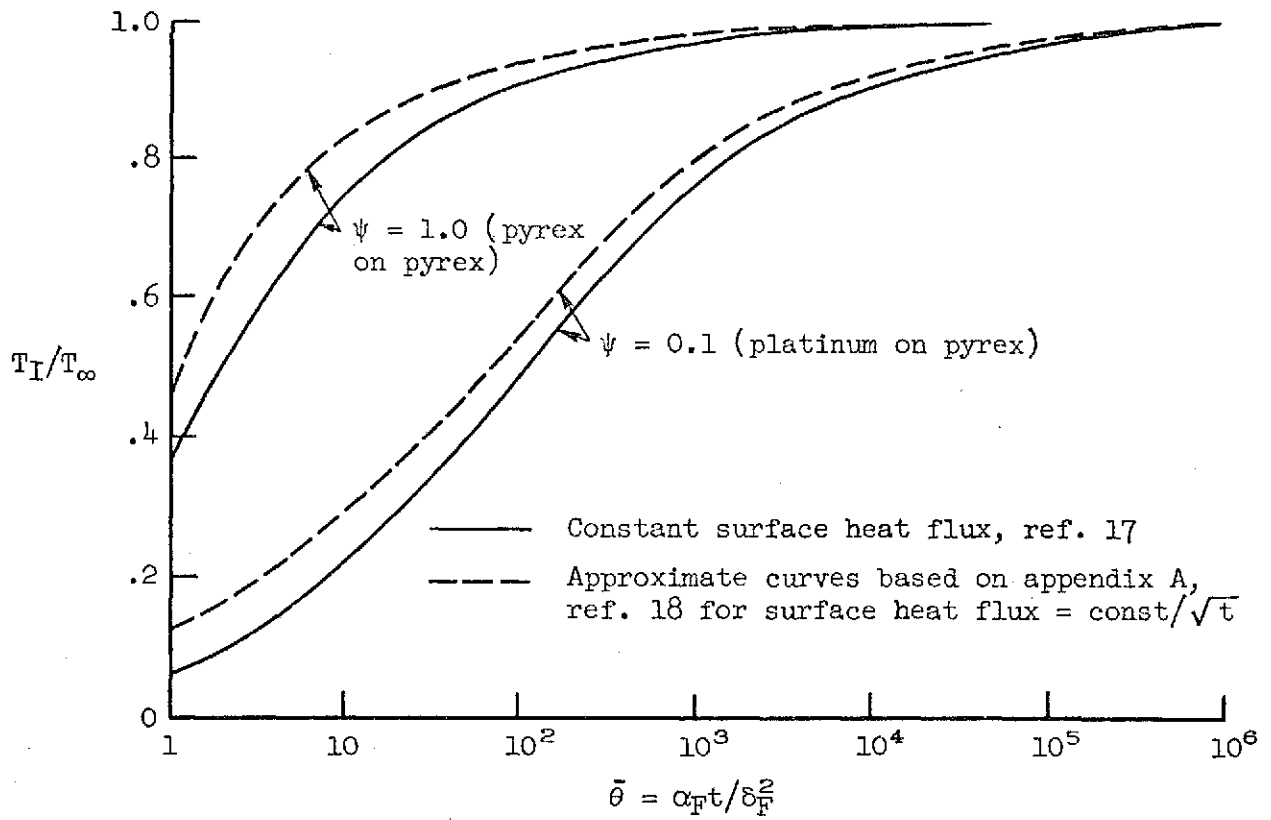
Figure 7.- Dimensionless interface temperature change of a composite semi-infinite solid.
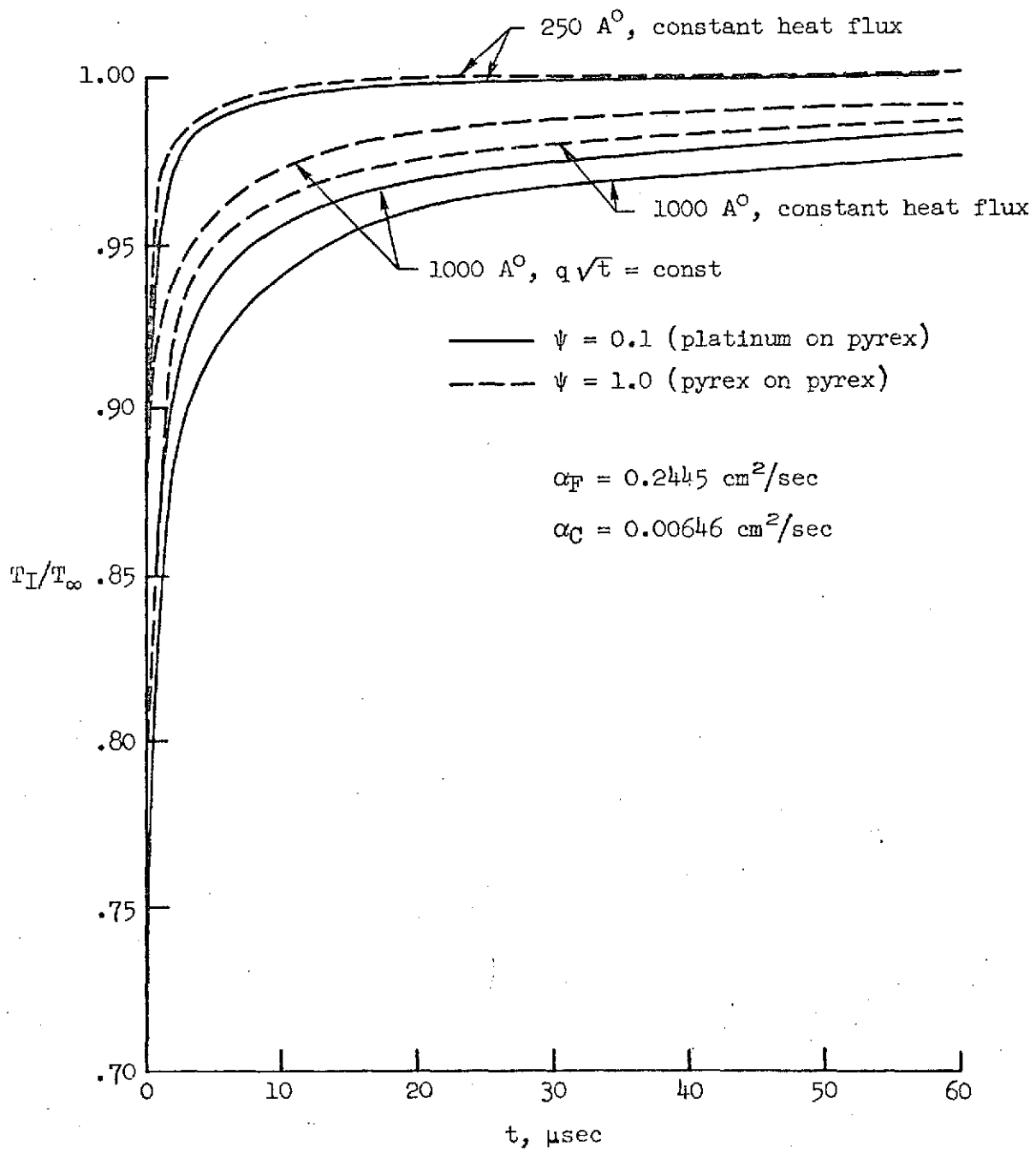
Figure 8.- Dimensionless interface temperature change vs time.
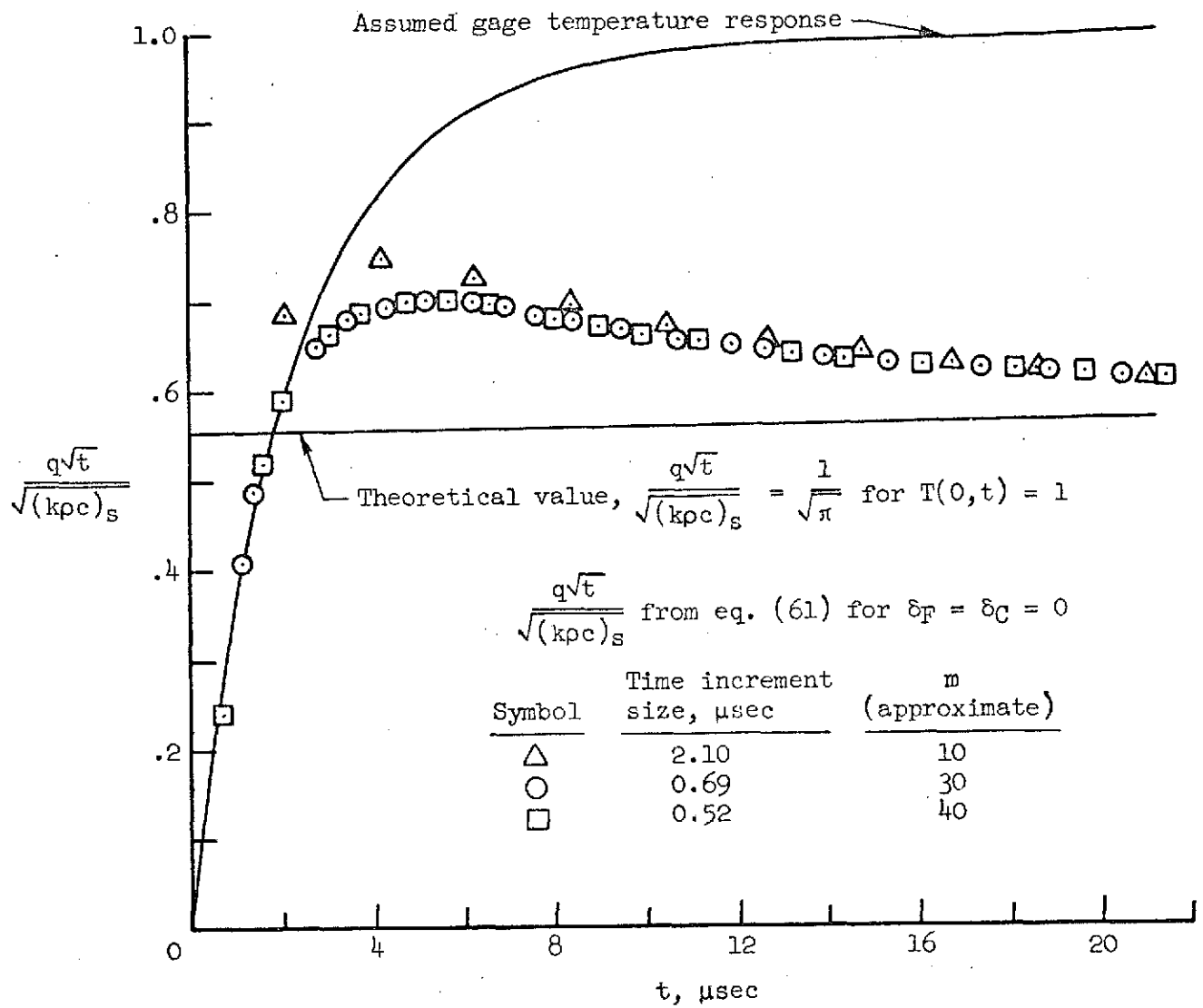
(a) Assumed gage temperature response and corresponding heat flux quantities.
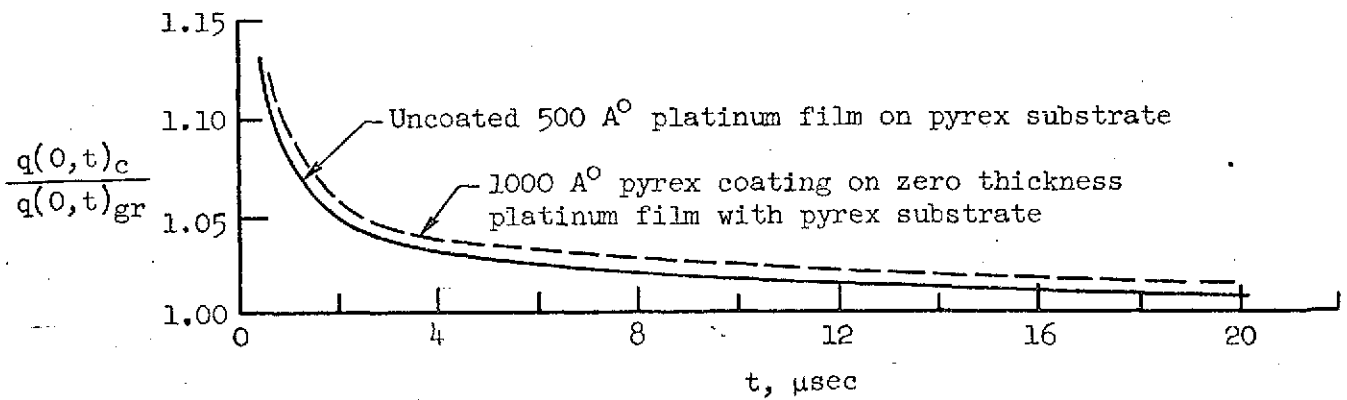
(b) Ratio of corrected to uncorrected heat flux for assumed gage response.

Figure 9.- Assumed gage response curve and computed heat flux quantities.
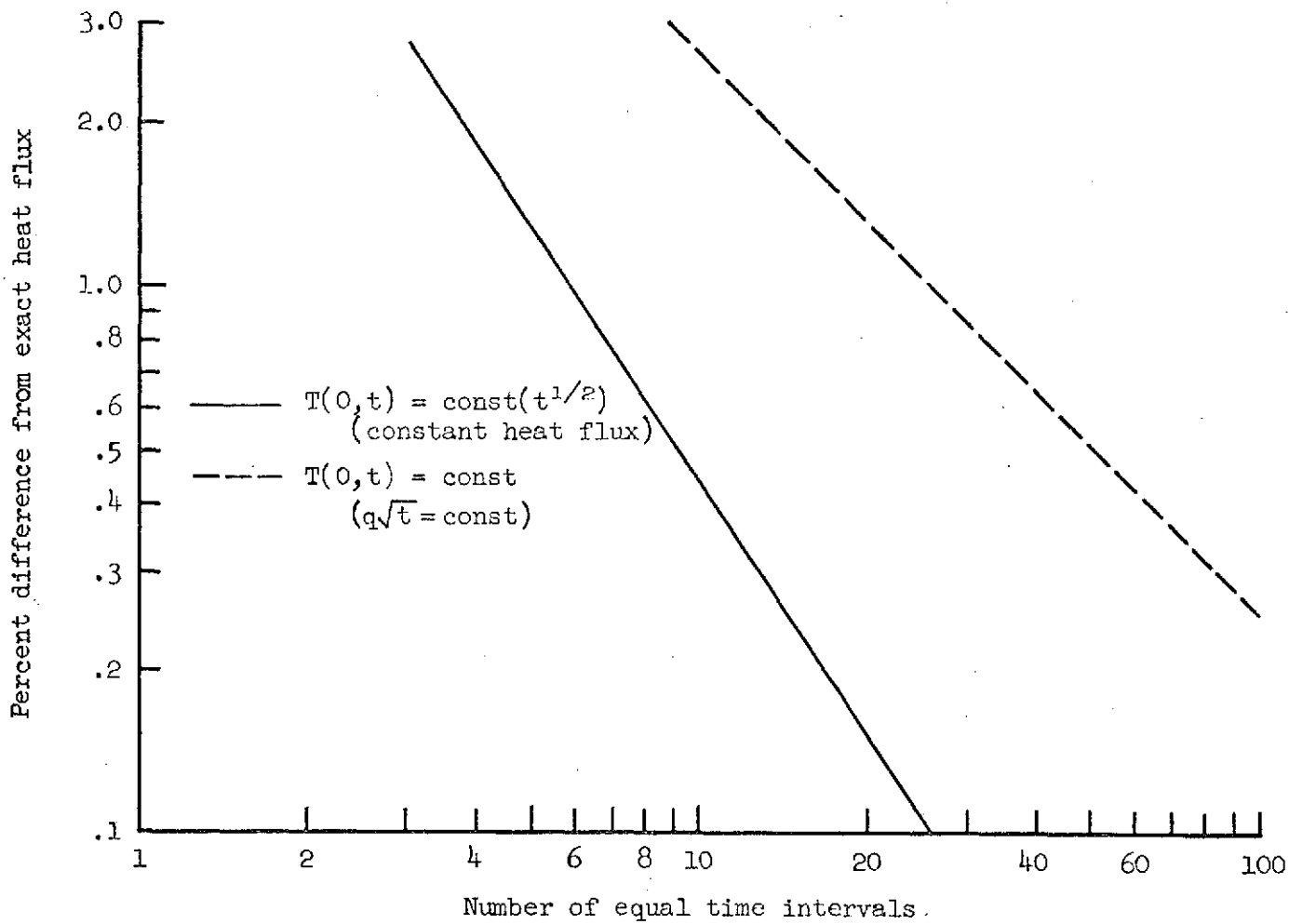
Figure 10.- Percent error in heat flux involved in using eq. (61) vs number of equal time intervals for two boundary conditions, (ref. 19).
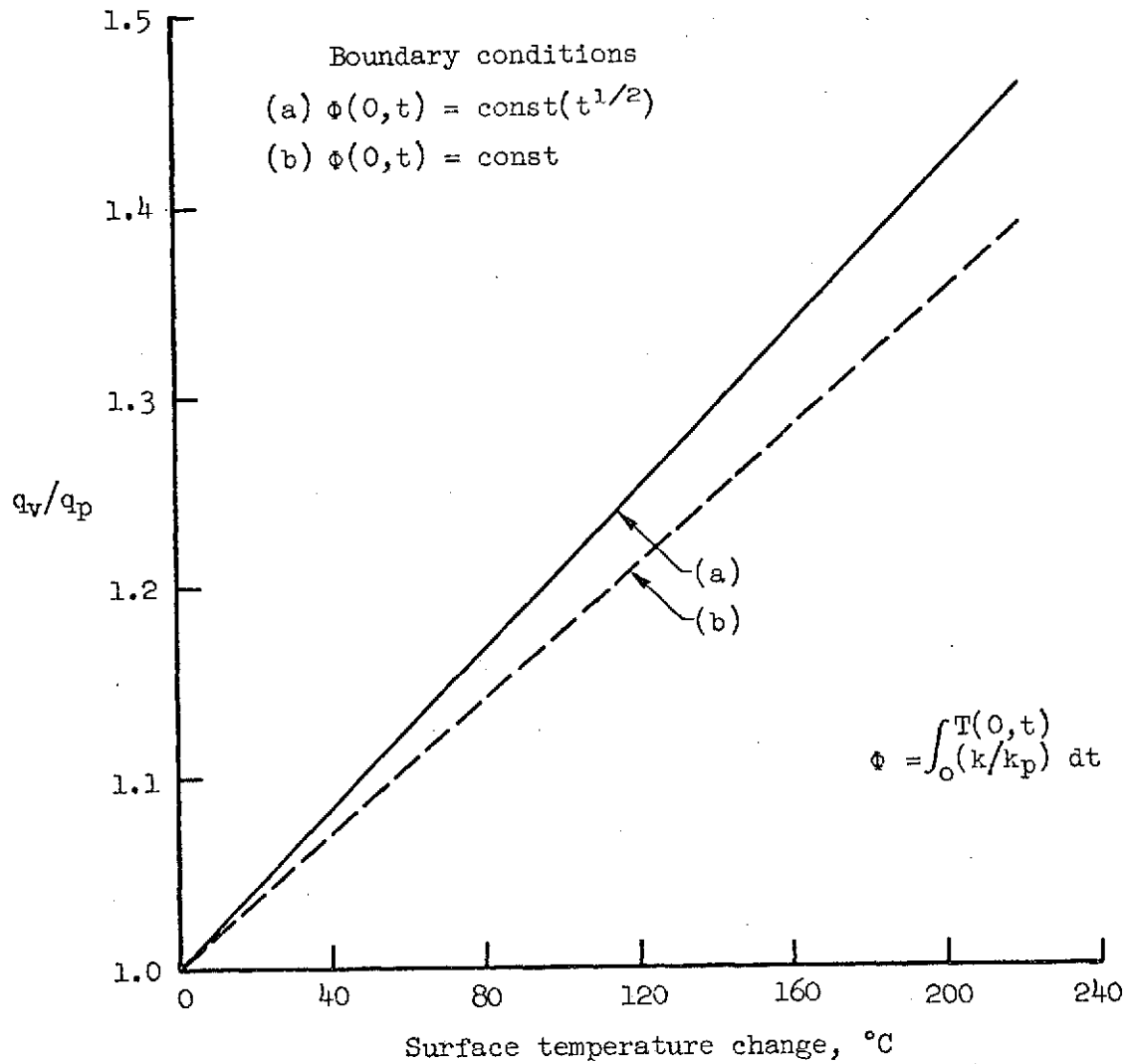
Figure 11.- Ratio of heat flux computed for variable substrate properties to that computed assuming constant substrate properties. Code 7740 pyrex, (ref. 21).
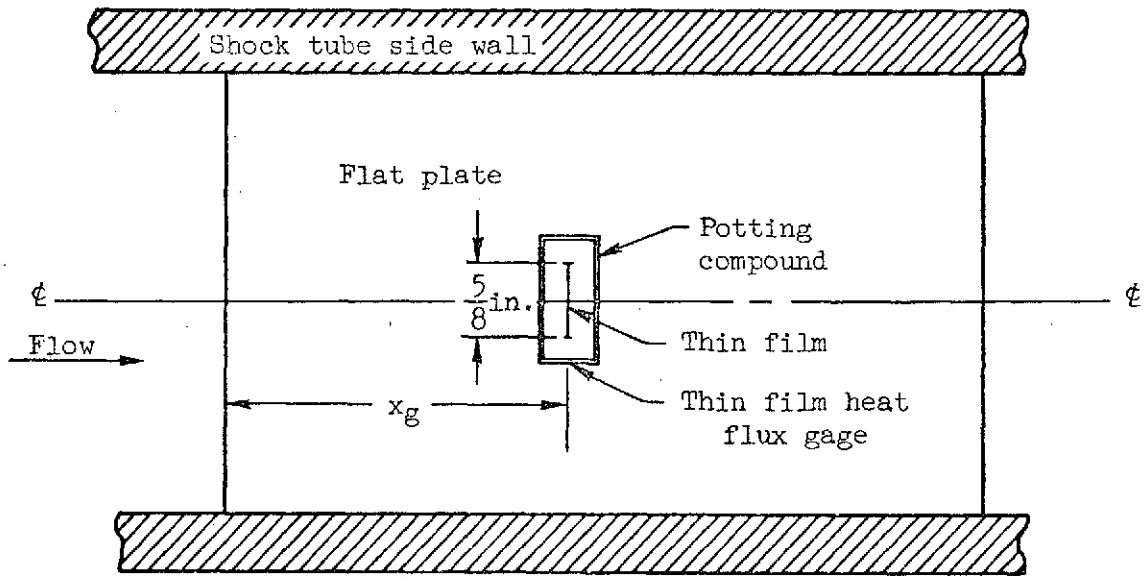
(a) Top view.
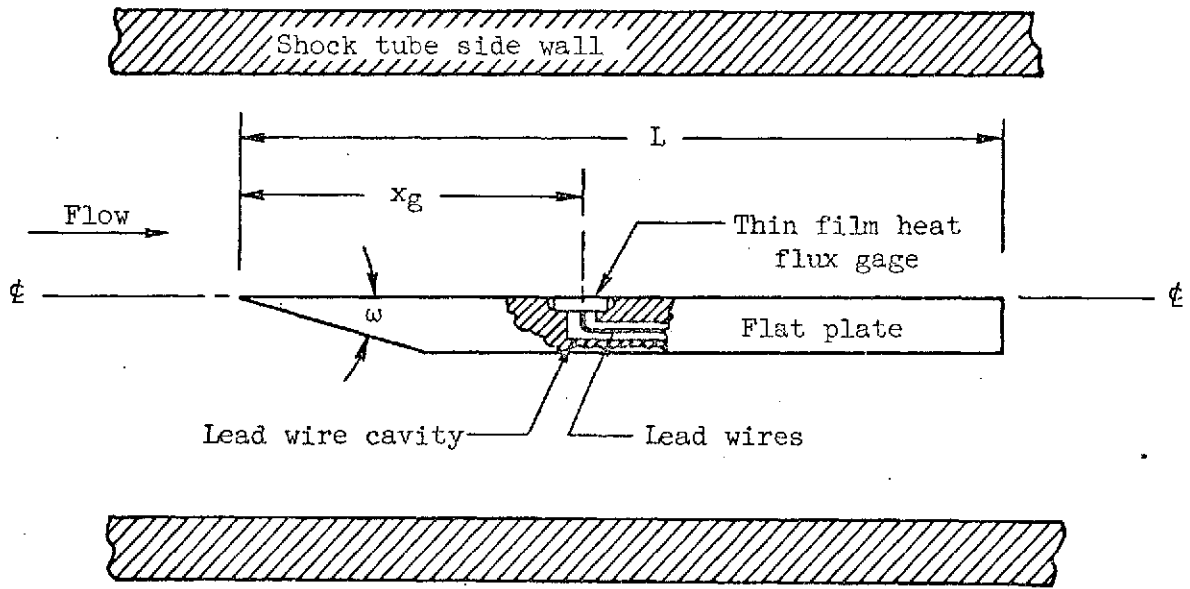
(b) Side view

Figure 12.- Flat plate model showing typical thin-film heat flux gage installation.
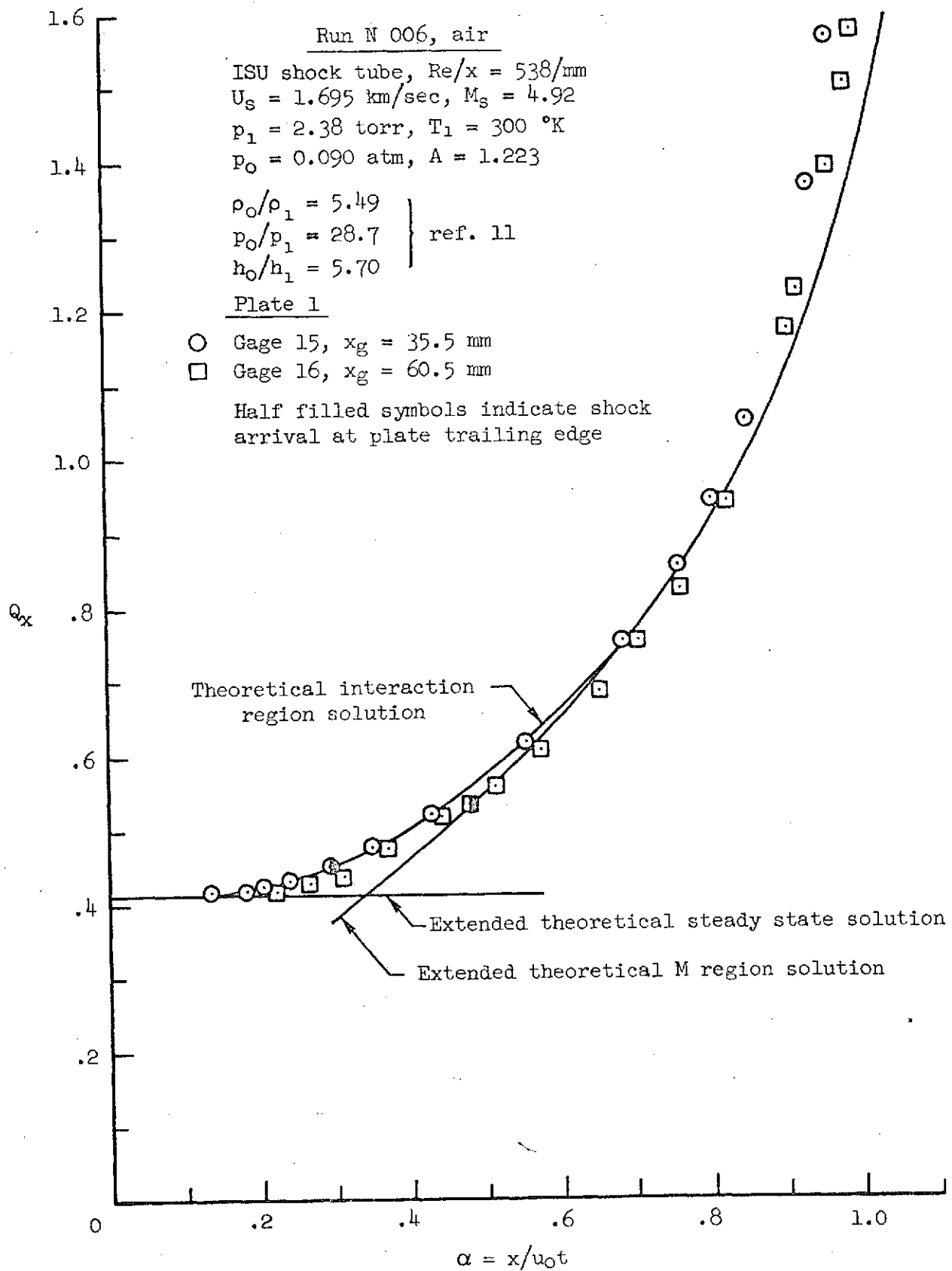
Figure 13.- Comparison of theoretical and experimental heat transfer results, $U_S = 1.695$ km/sec.

Run N 010, air

ISU shock tube, $Re/x = 613/mm$
$U_S = 1.966$ km/sec, $M_S = 5.66$
$p_1 = 2.38$ torr, $T_1 = 300$ °K
$p_0 = 0.12$ atm, $A = 1.202$

$\rho_0/\rho_1 = 5.95$
$p_0/p_1 = 38.4$ } ref. 11
$h_0/h_1 = 7.25$

Plate 1

○   Gage 15, $x_g = 35.5$ mm
□   Gage 16, $x_g = 60.5$ mm
——   Theory

Half filled symbols indicate shock
arrival at plate trailing edge

Q_x

$\alpha = x/u_0t$
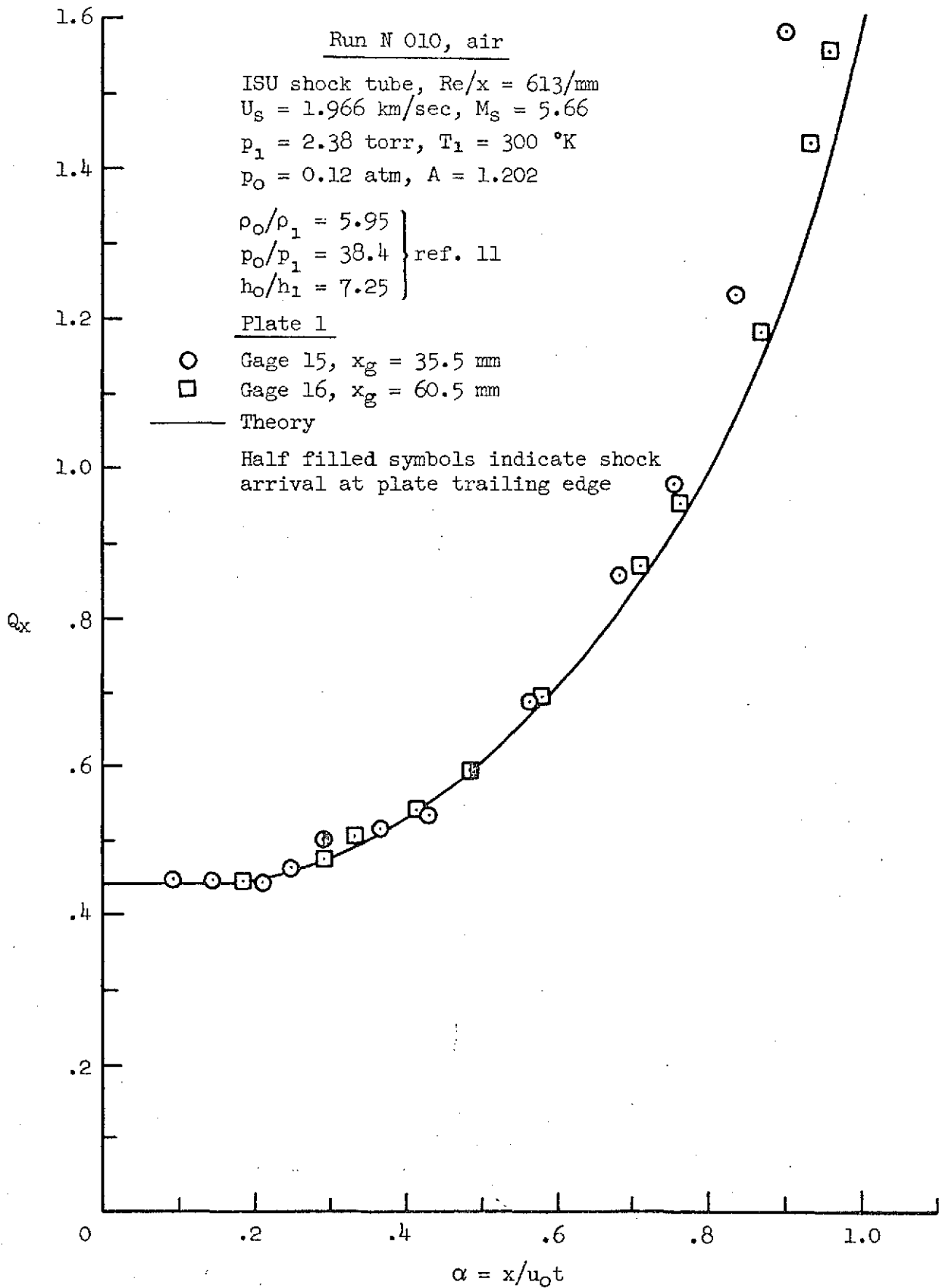
(a) Comparison of theoretical and experimental heat transfer results.

Figure 14.- Data for $U_S = 1.966$ km/sec.
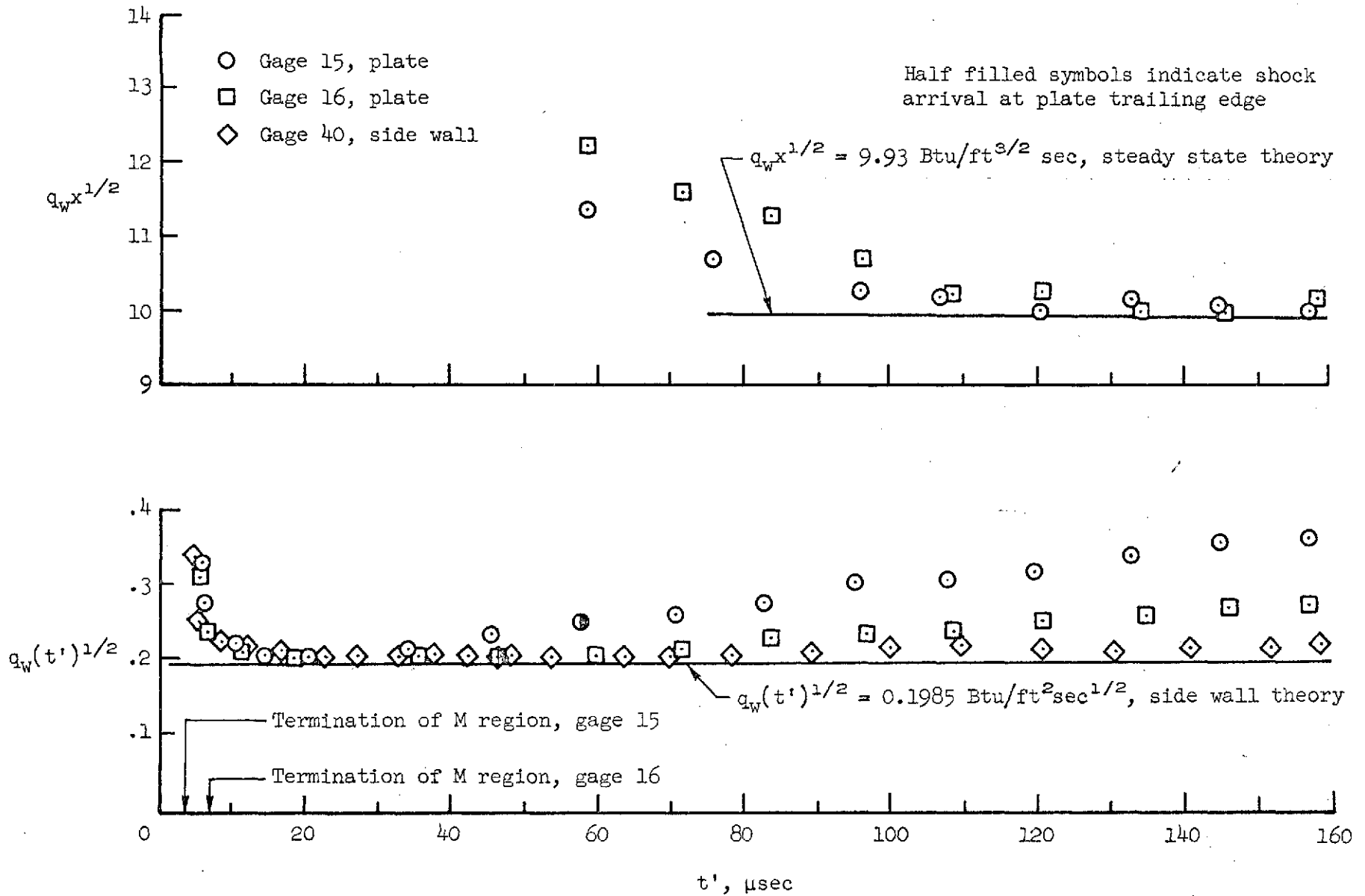
(b) Heat transfer quantities vs t'.

Figure 14.- Concluded.

Run N 012, air

ISU shock tube, Re/x = 202/mm
U_S = 2.35 km/sec, M_S = 6.78

p_1 = 0.63 torr, T_1 = 300 °K
p_0 = 0.0476 atm, A = 1.172

$\left.\begin{array}{l} \rho_0\ \rho_1 = 6.85 \\ p_0/p_1 = 57.3 \\ h_0/h_1 = 10.01 \end{array}\right\}$ ref. 11

Plate 1

O Gage 15, x_g = 35.5 mm
□ Gage 16, x_g = 60.5 mm
——— Theory

Half filled symbols indicate
shock arrival at plate
trailing edge
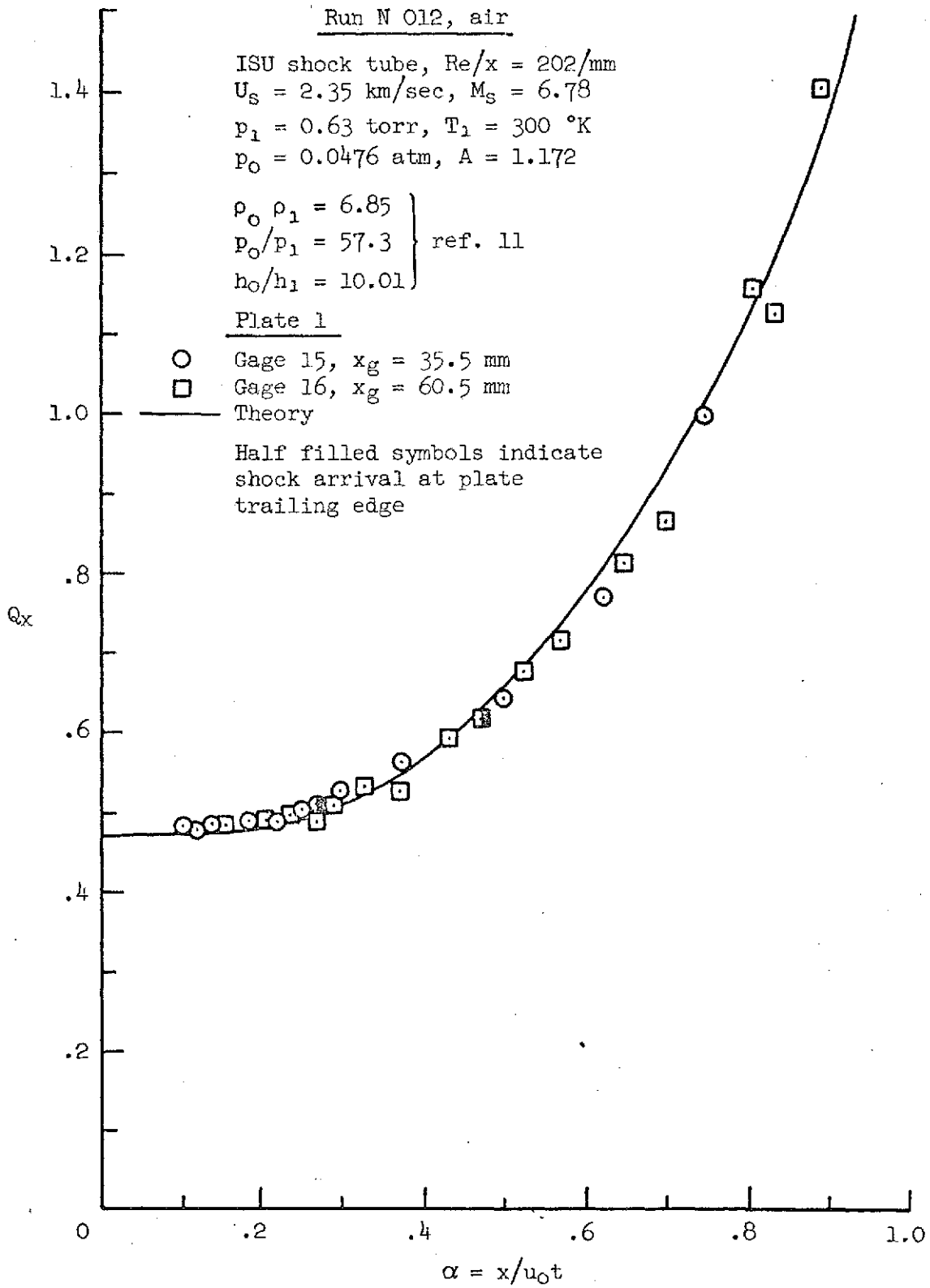
(a) Comparison of theoretical and experimental heat transfer results.

Figure 15.- Data for U_S = 2.35 km/sec.
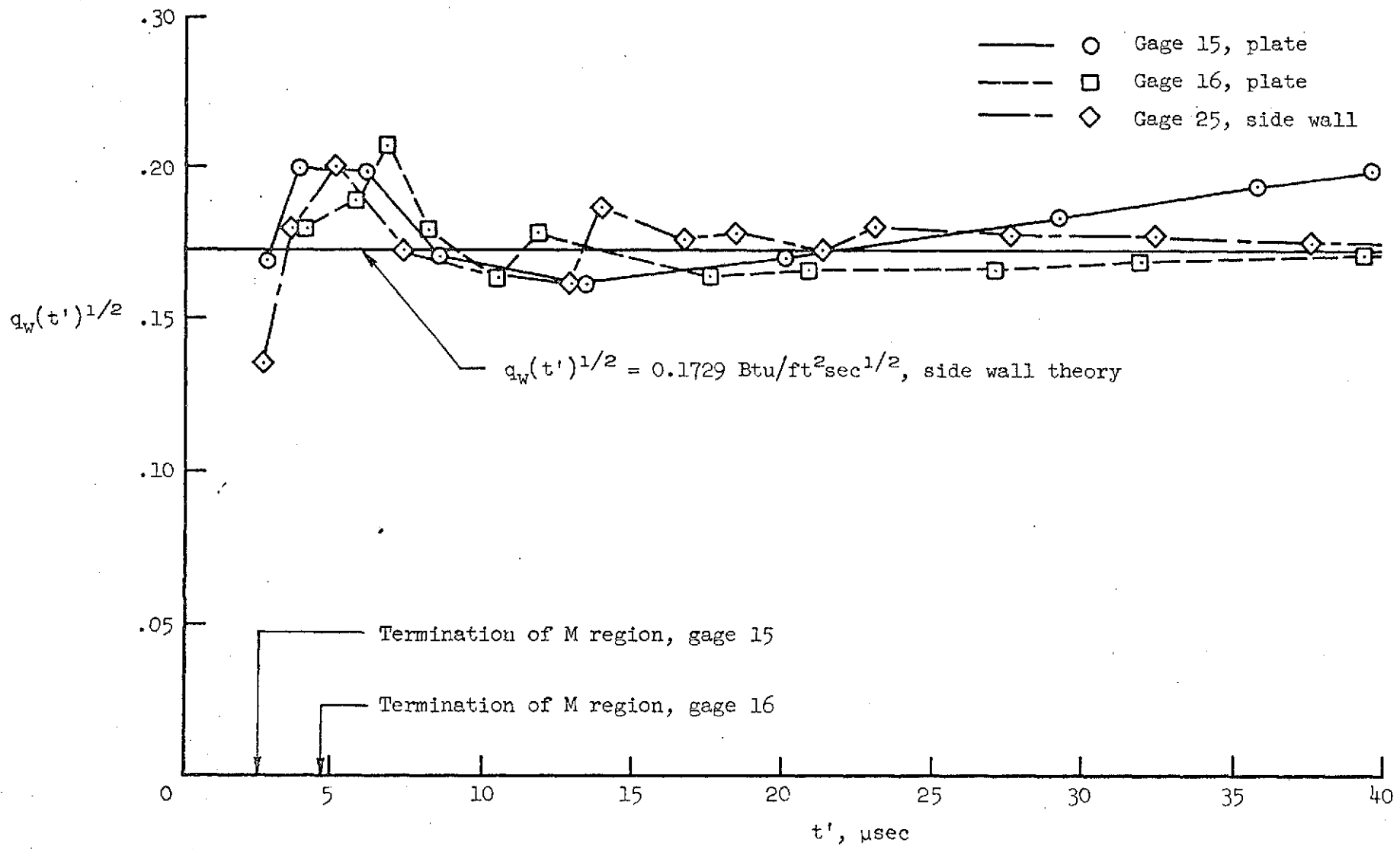
(b) Heat transfer quantities vs t'.

Figure 15.- Concluded.
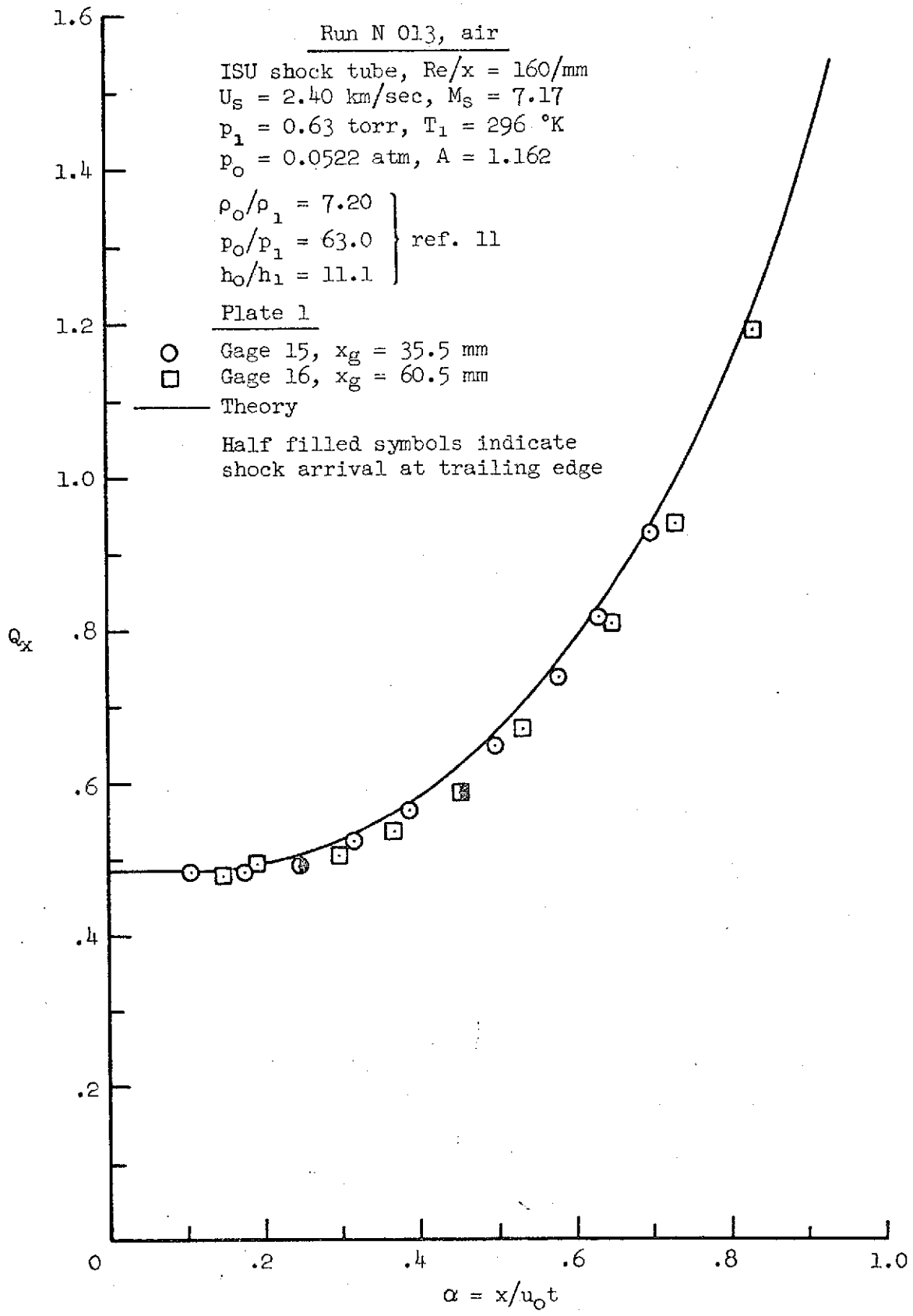
Figure 17.- Comparison of theoretical and experimental heat transfer results, $U_S = 2.48$ km/sec.
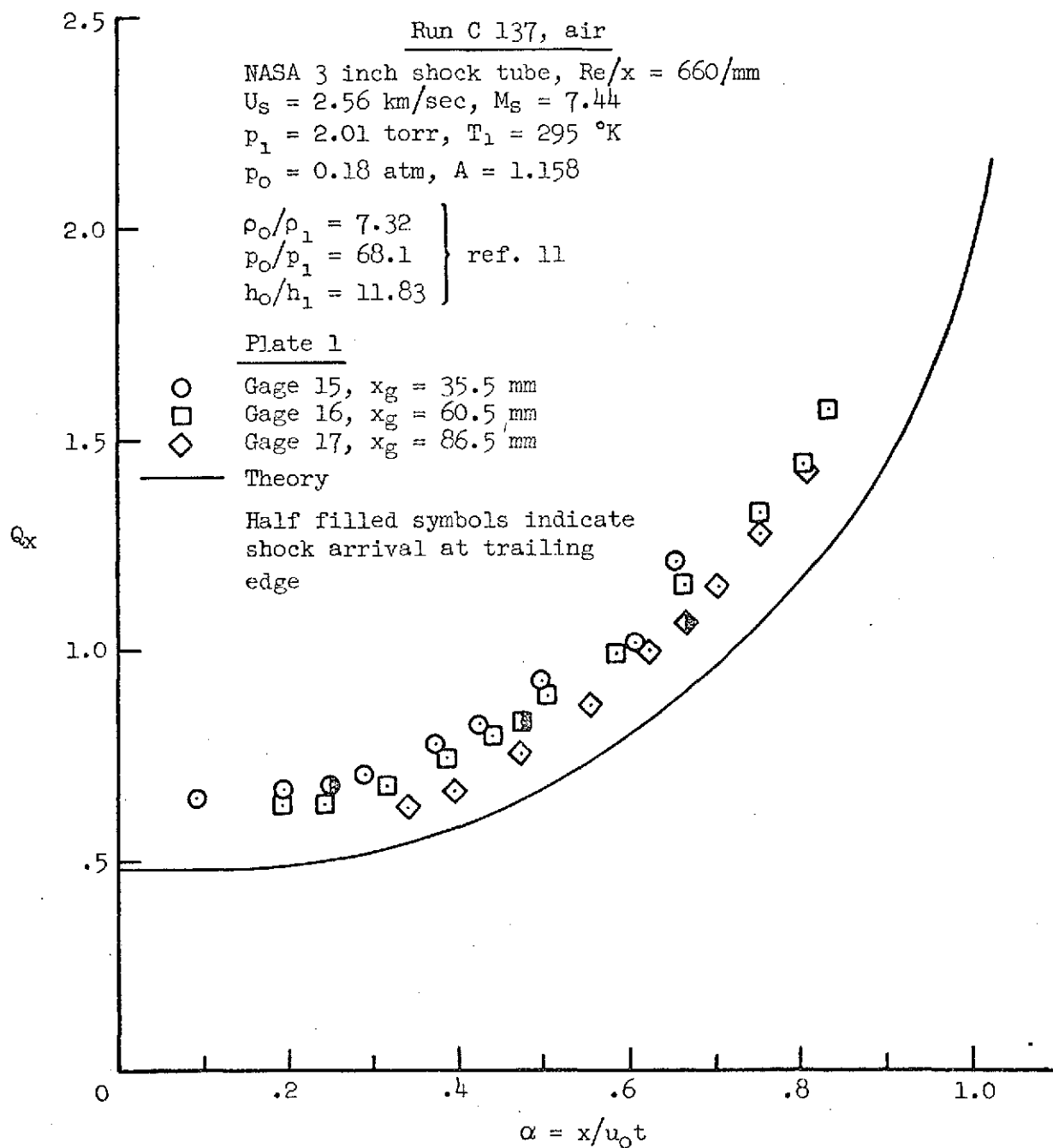
(a) Comparison of theoretical and experimental heat transfer results.

Figure 18.- Data for $U_S = 2.56$ km/sec.
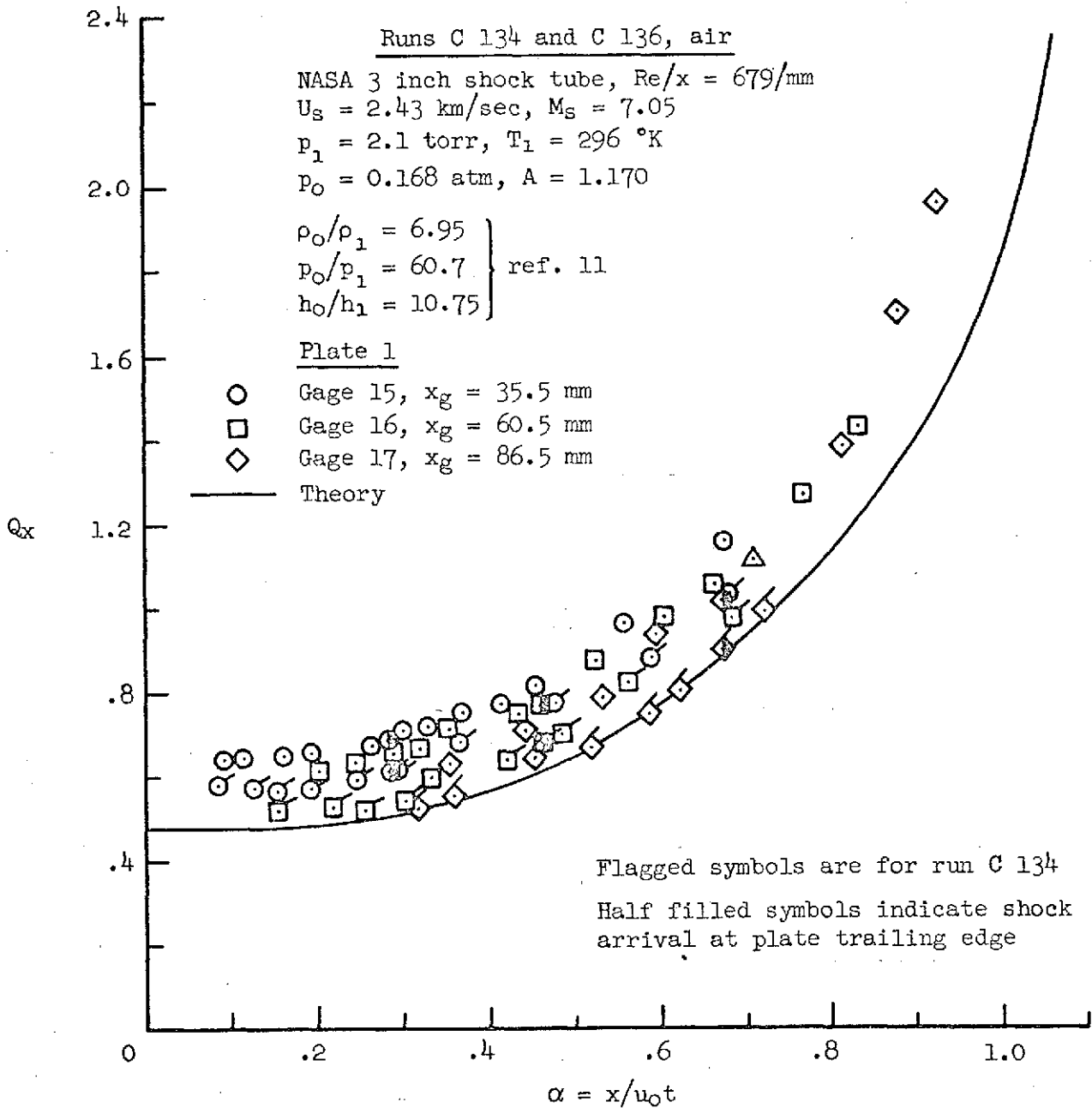
Figure 16.- Comparison of theoretical and experimental heat transfer
results, U_S = 2.43 km/sec.
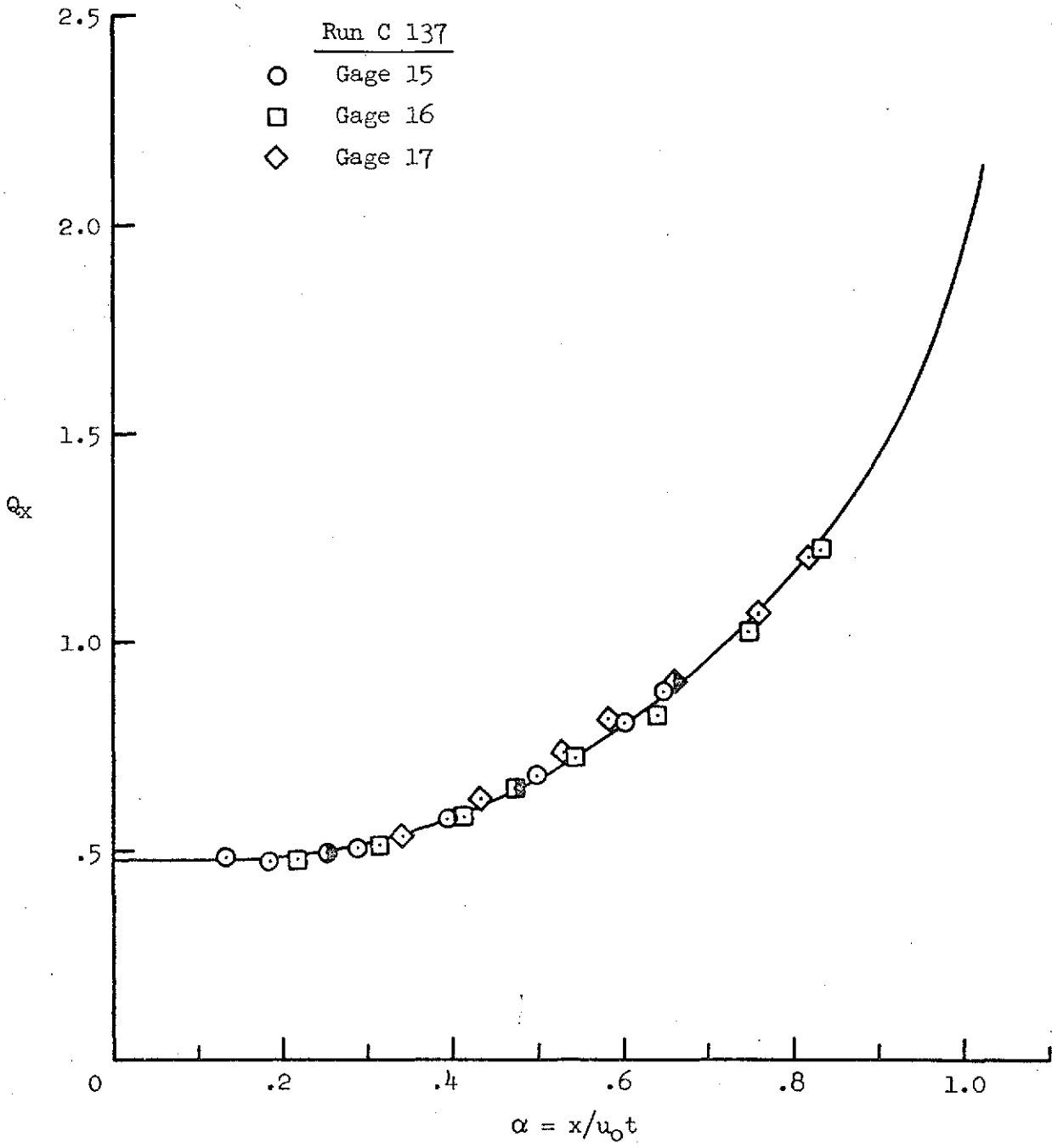
(b) Modified experimental results.

Figure 18.- Concluded.
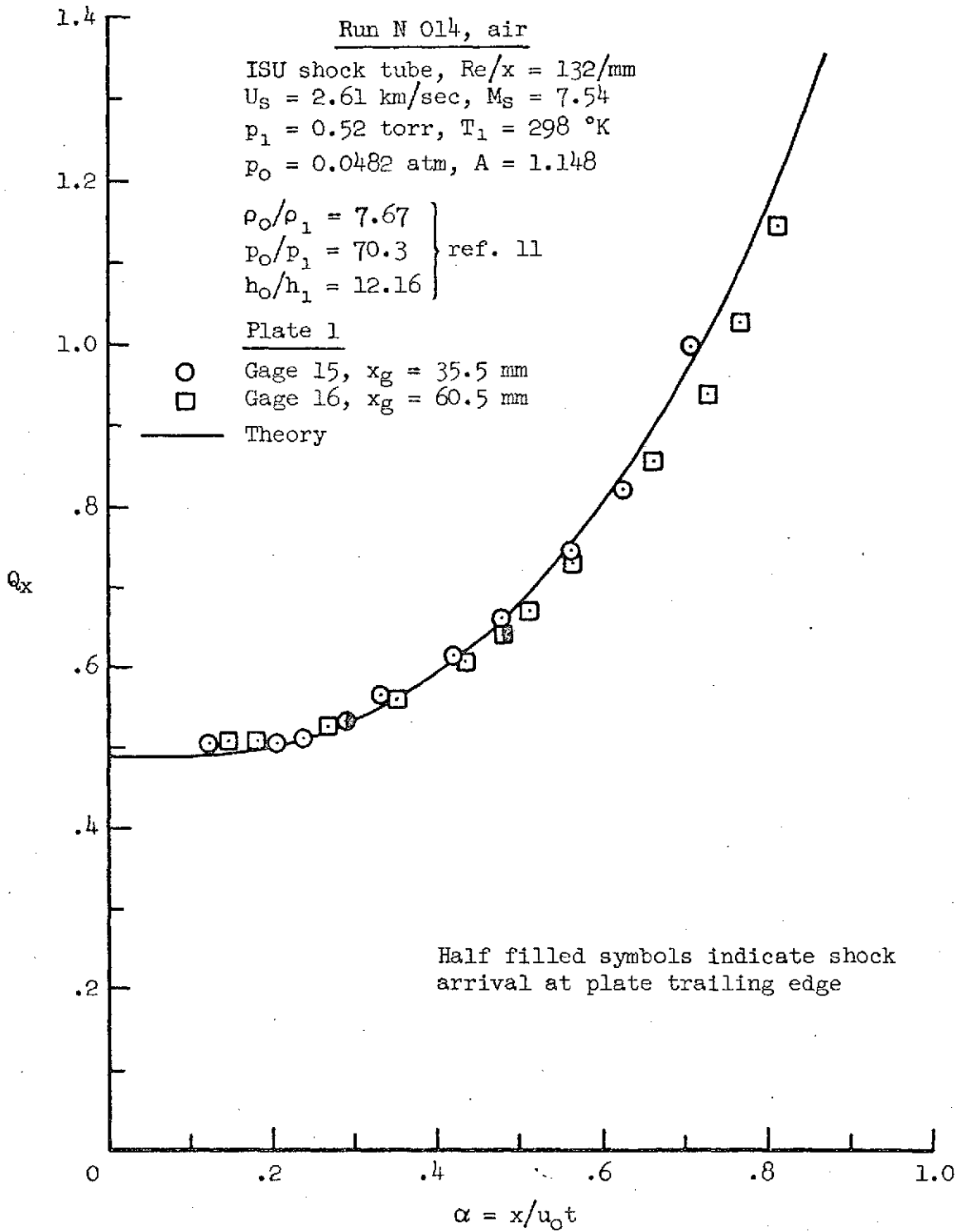
Figure 19.- Comparison of theoretical and experimental heat transfer results, U_S = 2.61 km/sec.
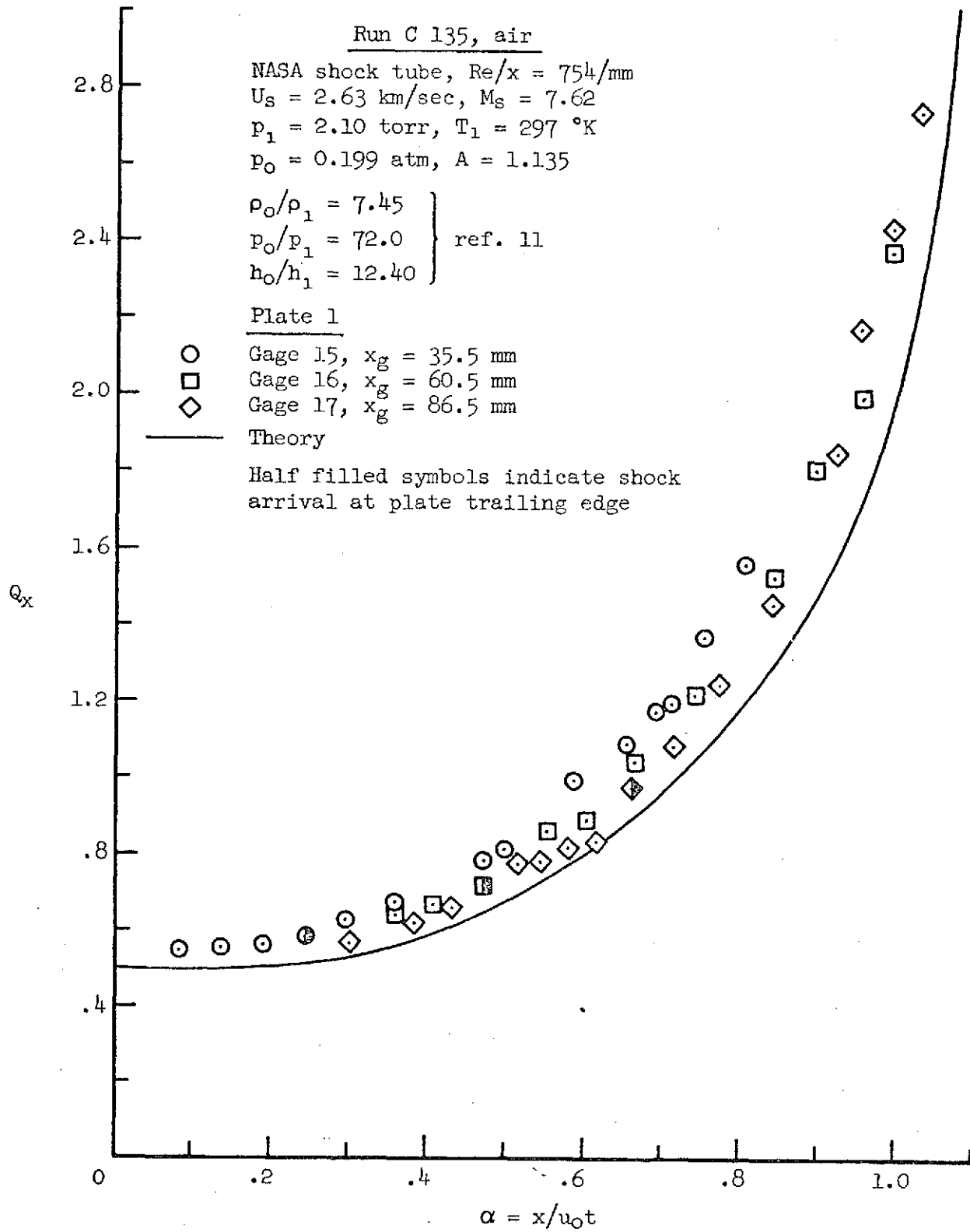
Figure 20.– Comparison of theoretical and experimental heat transfer results, $U_S = 2.63$ km/sec.
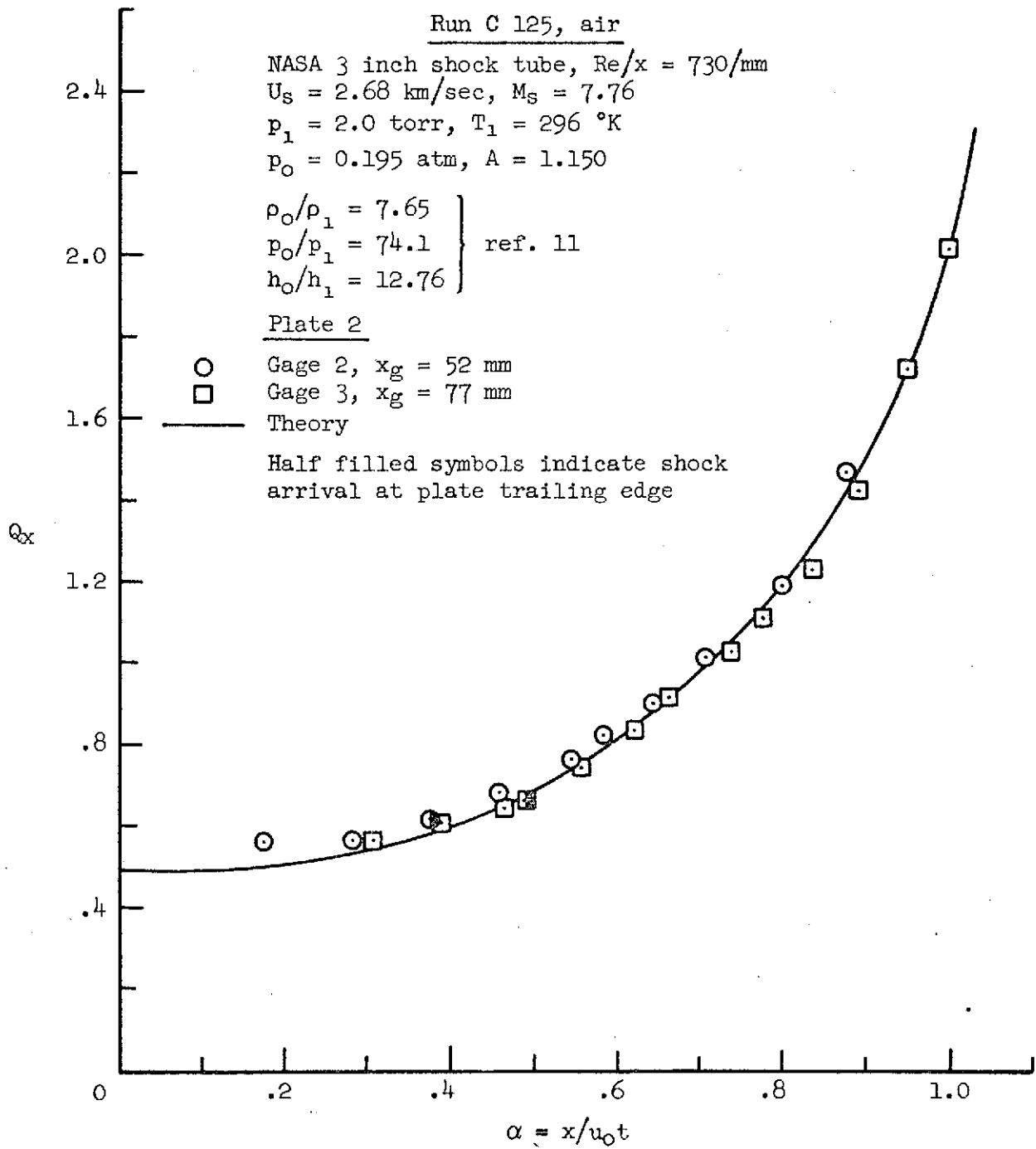
Figure 21.- Comparison of theoretical and experimental heat transfer results, $U_S = 2.68$ km/sec.

Run C 142, air

NASA 3 inch shock tube, $Re/x = 870/mm$
$U_S = 2.83$ km/sec, $M_S = 8.20$
$p_1 = 2.25$ torr, $T_1 = 295$ °K
$p_0 = 0.246$ atm, $A = 1.143$

$\rho_0/\rho_1 = 8.05$
$p_0/p_1 = 83.1$ } ref. 11
$h_0/h_1 = 14.2$

Plate 1

○ Gage 15, scope 1, $x_g = 35.5$ mm
□ Gage 15, scope 2,
◇ Gage 16, $x_g = 60.5$ mm
—— Theory

Half filled symbols indicate shock arrival at plate trailing edge

Q_x

$\alpha = x/u_0 t$
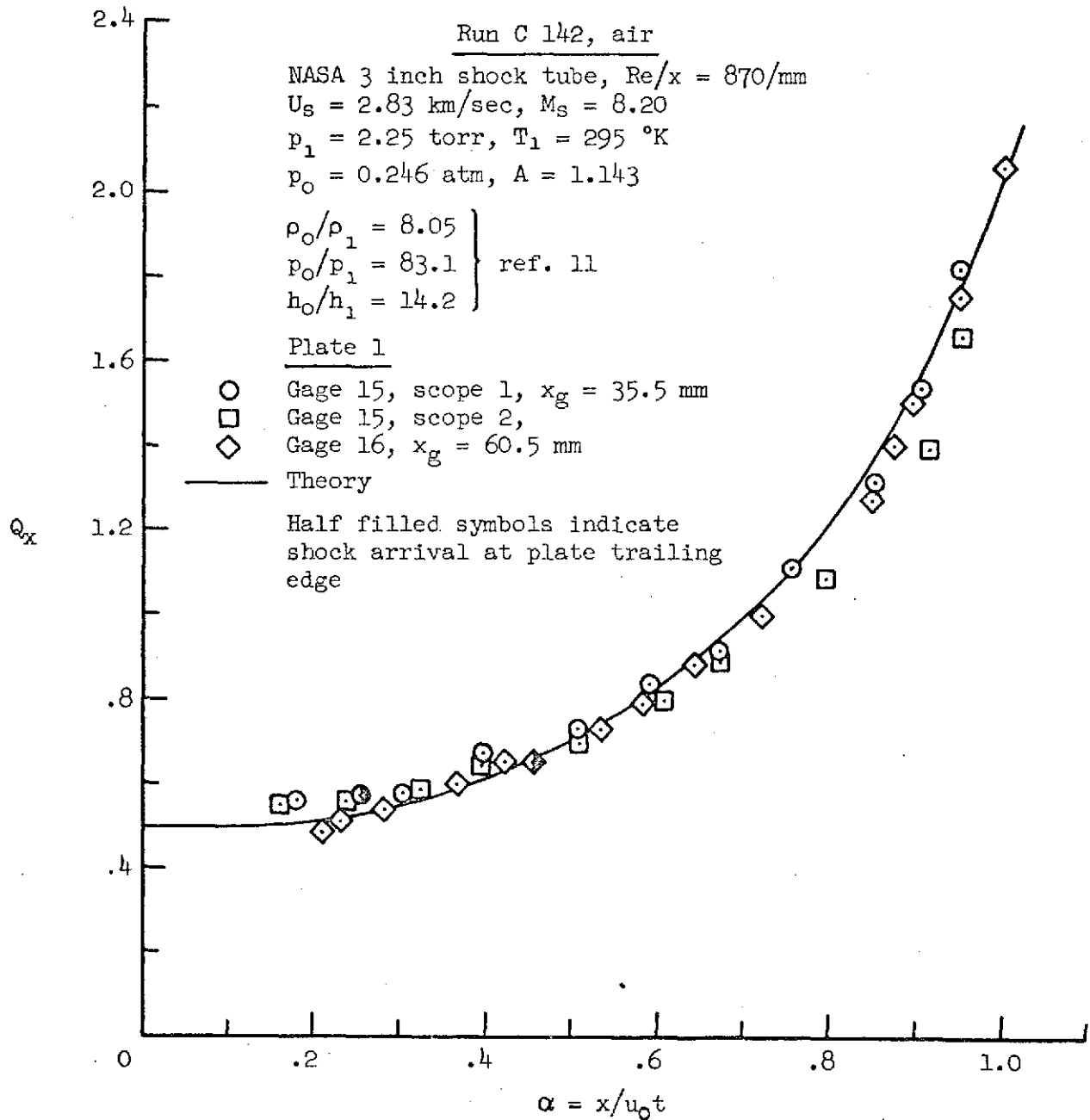
Figure 22.- Comparison of theoretical and experimental heat transfer results, $U_S = 2.83$ km/sec.
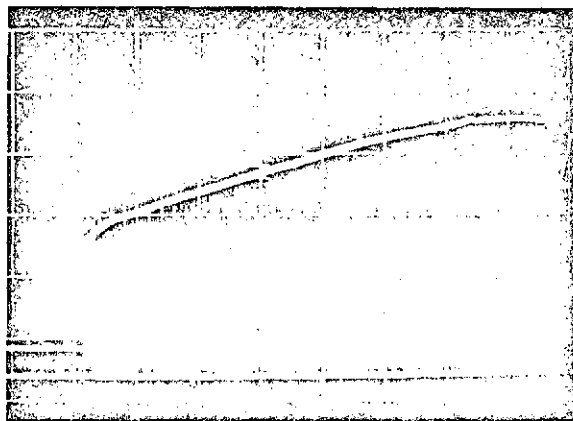
(a) Run C 142 (fig. 22)
     U_S = 2.83 km/sec, gage 15
     Test gas: air
     p_O = 0.246 atm
     Time base: 19.2 μsec/div.
     Vertical: 5.52°C/div.
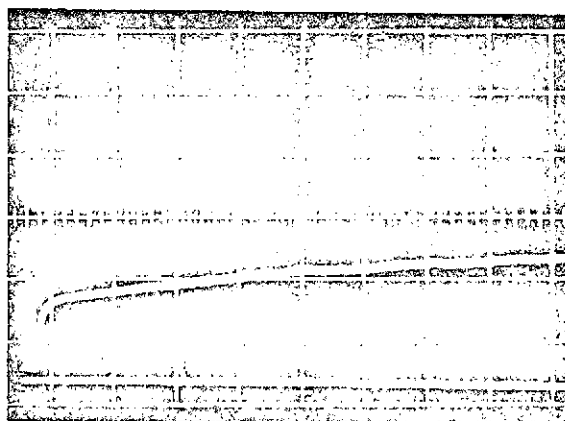
(b) Run C 159 (fig. 24)
     U_S = 3.16 km/sec, gage 02
     Test gas: nitrogen,
     p_O = 0.203 atm
   Time base: 10 μsec/div.
     Vertical: 6.20°C/div.
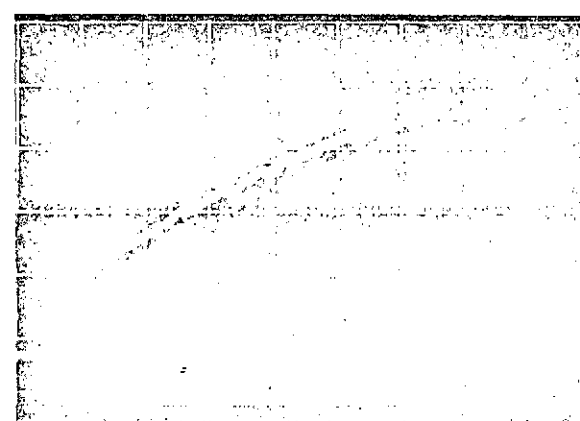
(c) Run S 182 (fig. 28(a), (b))
     U_S = 4.59 km/sec, gage V9
     Test gas: nitrogen,
     p_O = 0.29 atm
   Time base: 20.4 μsec/div.
     Vertical: 9.81°C/div.

Figure 23.- Typical oscilloscope records of thin-film heat flux gage response; all sensitivities
are per major scale division.
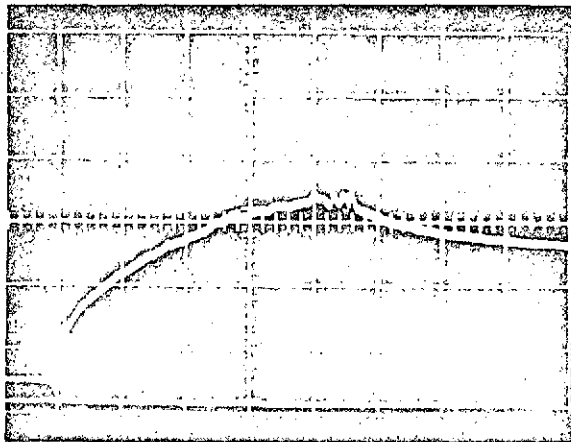
(d) Run S 184 (fig. 30(a))
     U_S = 5.81 km/sec, gage V9
     Test gas: nitrogen,
     p_O = 0.473 atm
     Time base: 20.4 μsec/div.
     Vertical: 24.6°C/div.
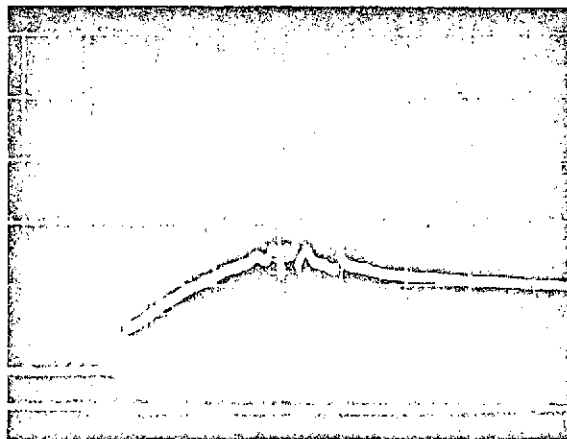
(e) Run S 188 (fig. 31(a))
     U_S = 6.04 km/sec, gage V9
     Test gas: nitrogen,
     p_O = 0.26 atm
     Time base: 20.4 μsec/div.
     Vertical: 24.4°C/div.
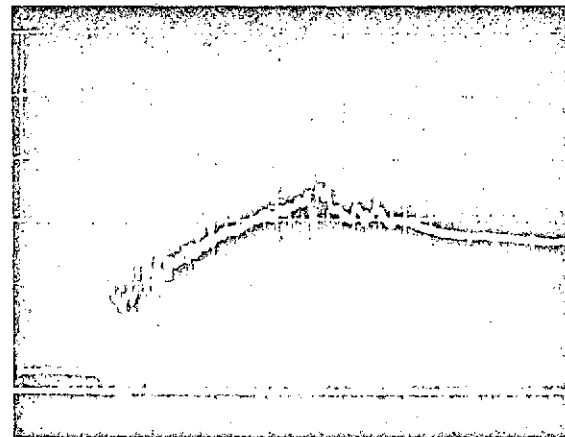
(f) Run S 175 (fig. 31(c))
     U_S = 6.10 km/sec, gage M4
     Test gas: nitrogen,
     p_O = 0.537 atm
     Time base: 20.4 μsec/div.
     Vertical: 26.6°C/div.

Figure 23.- Concluded.
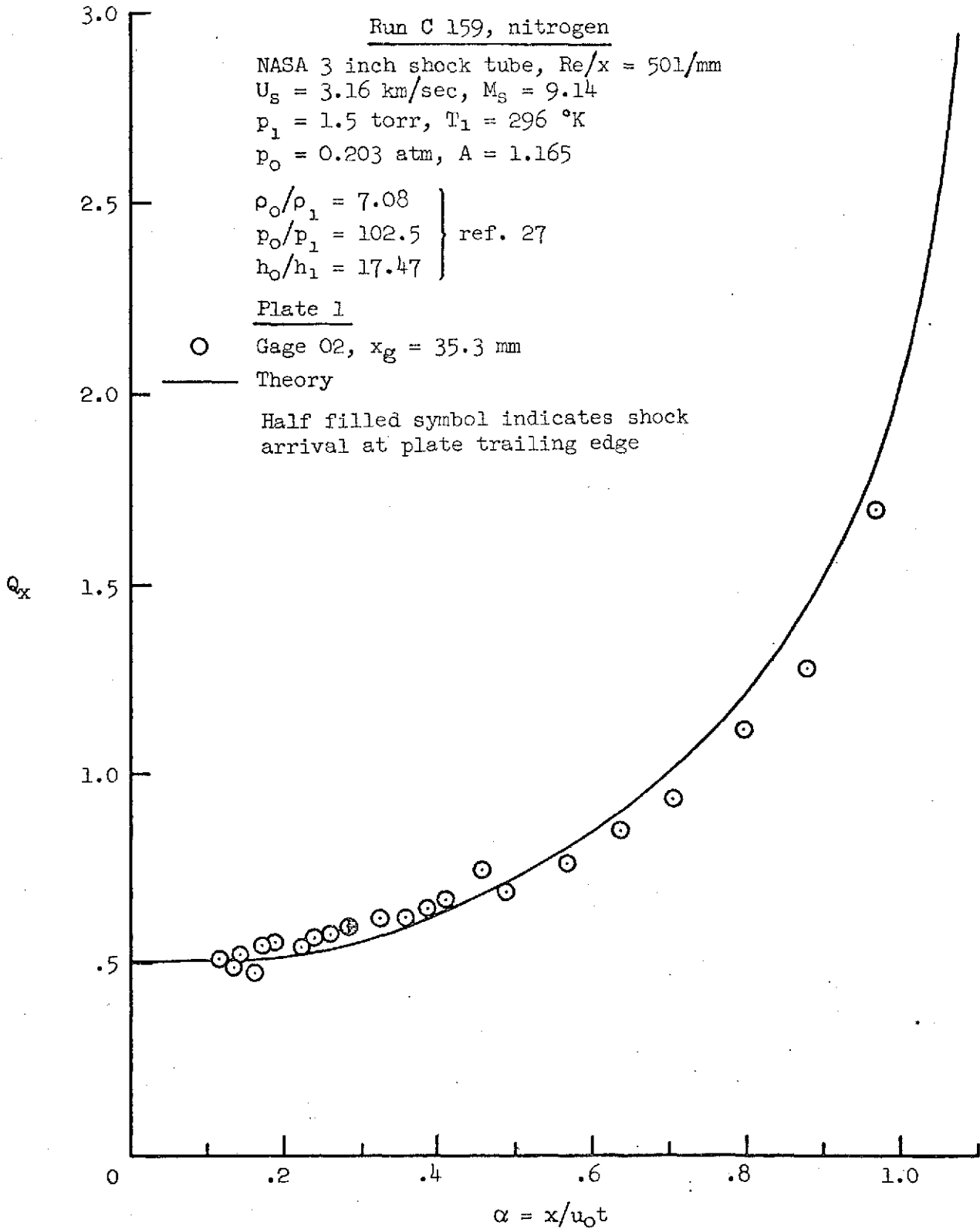
Figure 24.- Comparison of theoretical and experimental heat transfer
results, U_S = 3.16 km/sec.
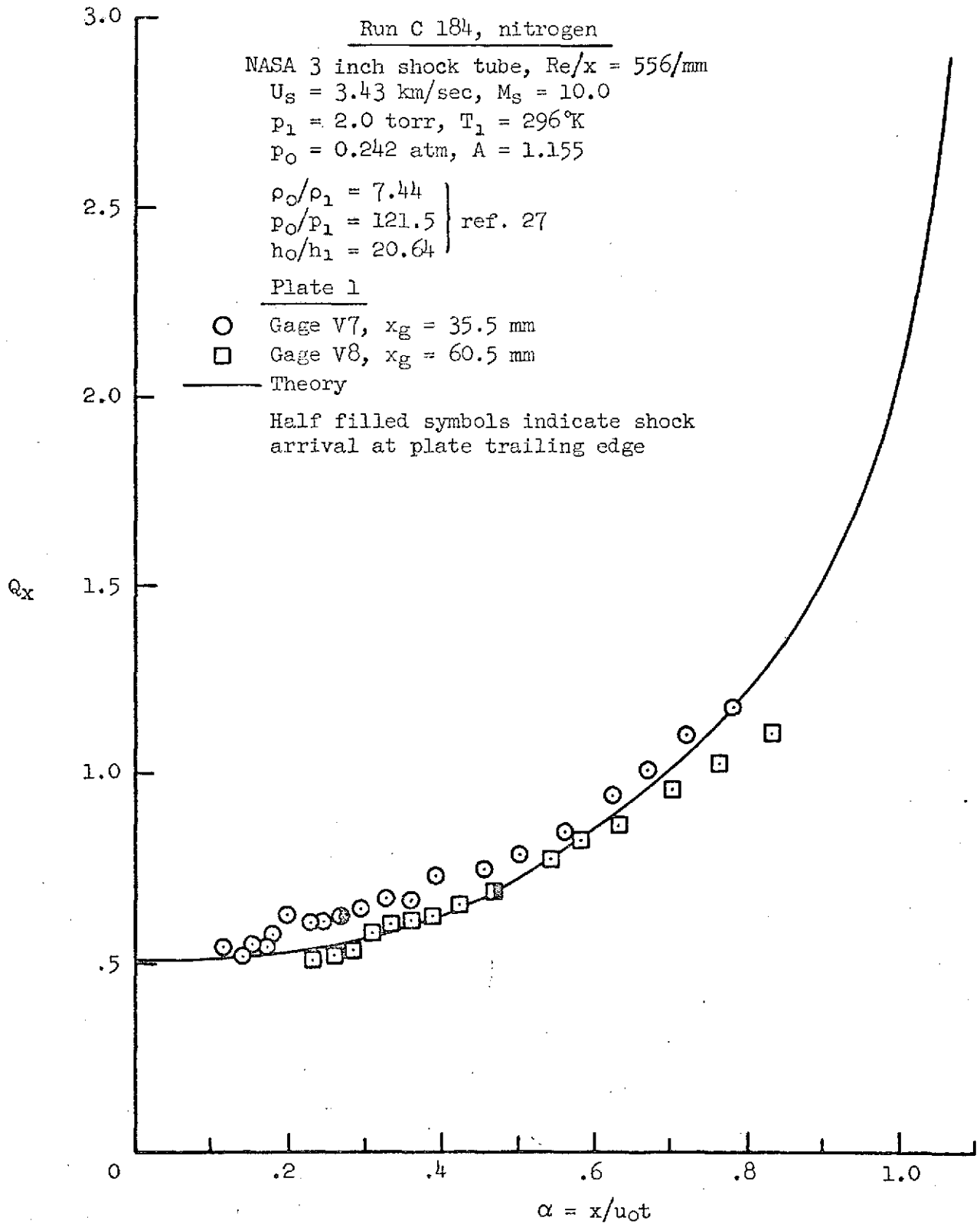
Figure 25.- Comparison of theoretical and experimental heat transfer results, $U_S = 3.43$ km/sec.
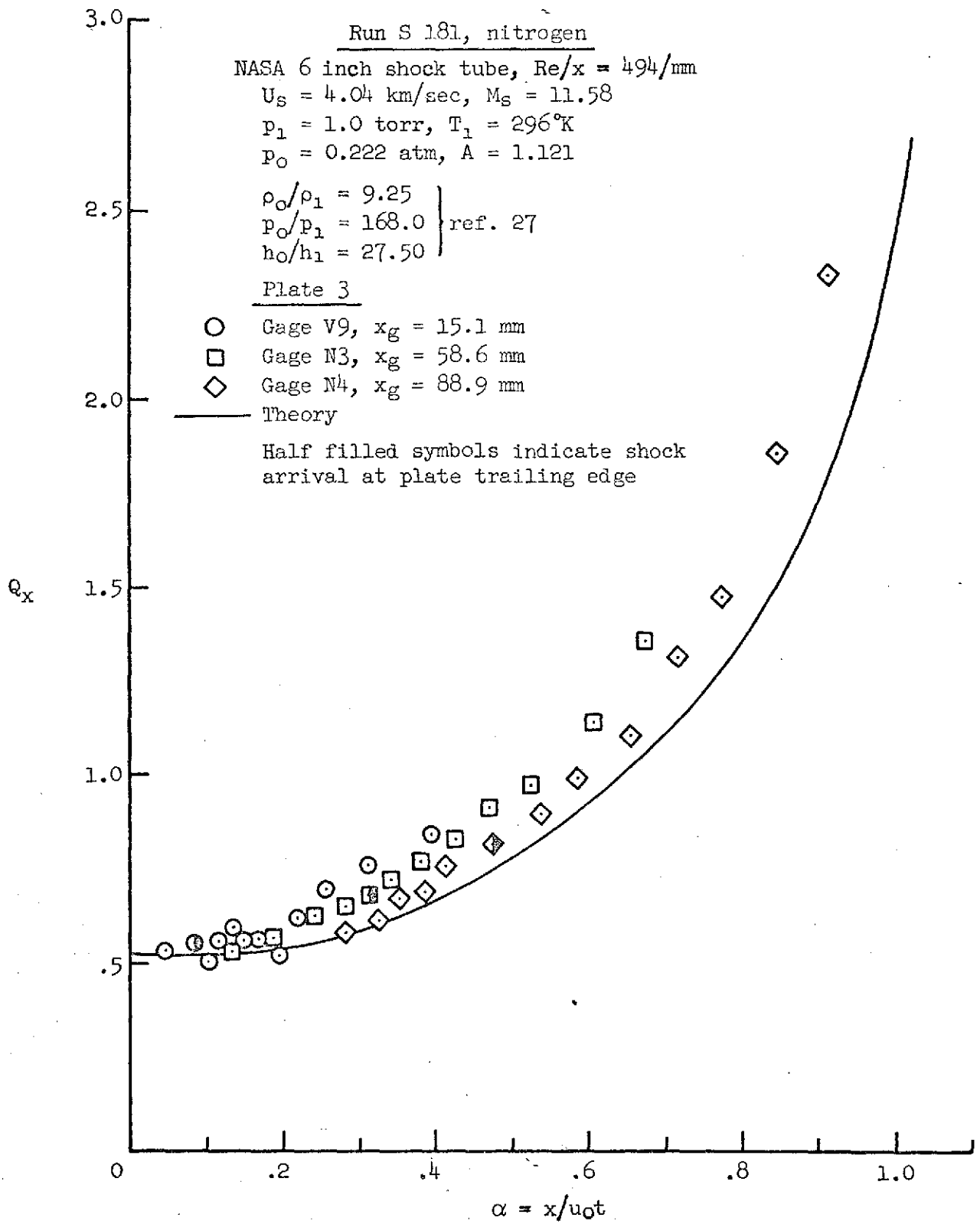
Figure 26.- Comparison of theoretical and experimental heat transfer results, $U_S = 4.04$ km/sec.
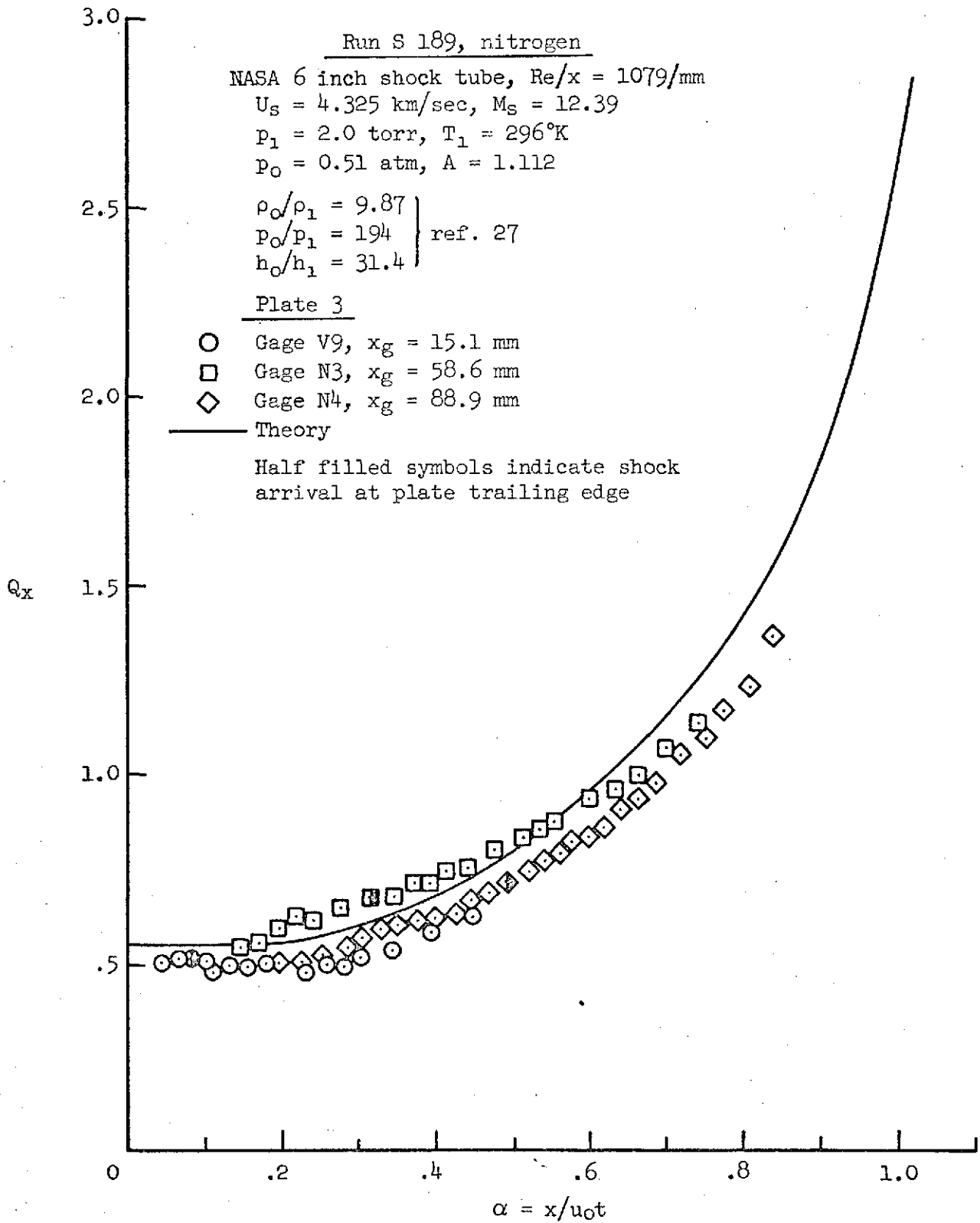
Figure 27.- Comparison of theoretical and experimental heat transfer results, $U_s = 4.325$ km/sec.

$$\text{Run S 182, nitrogen}$$

NASA 6 inch shock tube, $Re/x = 625/mm$
$U_S = 4.59 \text{ km/sec}$, $M_S = 13.15$
$p_1 = 1.0 \text{ torr}$, $T_1 = 296°K$
$p_O = 0.29 \text{ atm}$, $A = 1.106$

$\rho_O/\rho_1 = 10.50$
$p_O/p_1 = 220$ } ref. 27
$h_O/h_1 = 35.25$

$\underline{\text{Plate 3}}$

○ Gage V9, $x_g = 15.1 \text{ mm}$
□ Gage N3, $x_g = 58.6 \text{ mm}$
◇ Gage N4, $x_g = 88.9 \text{ mm}$
——— Theory

Half filled symbols indicate shock
arrival at plate trailing edge

Q_x

$\alpha = x/u_O t$
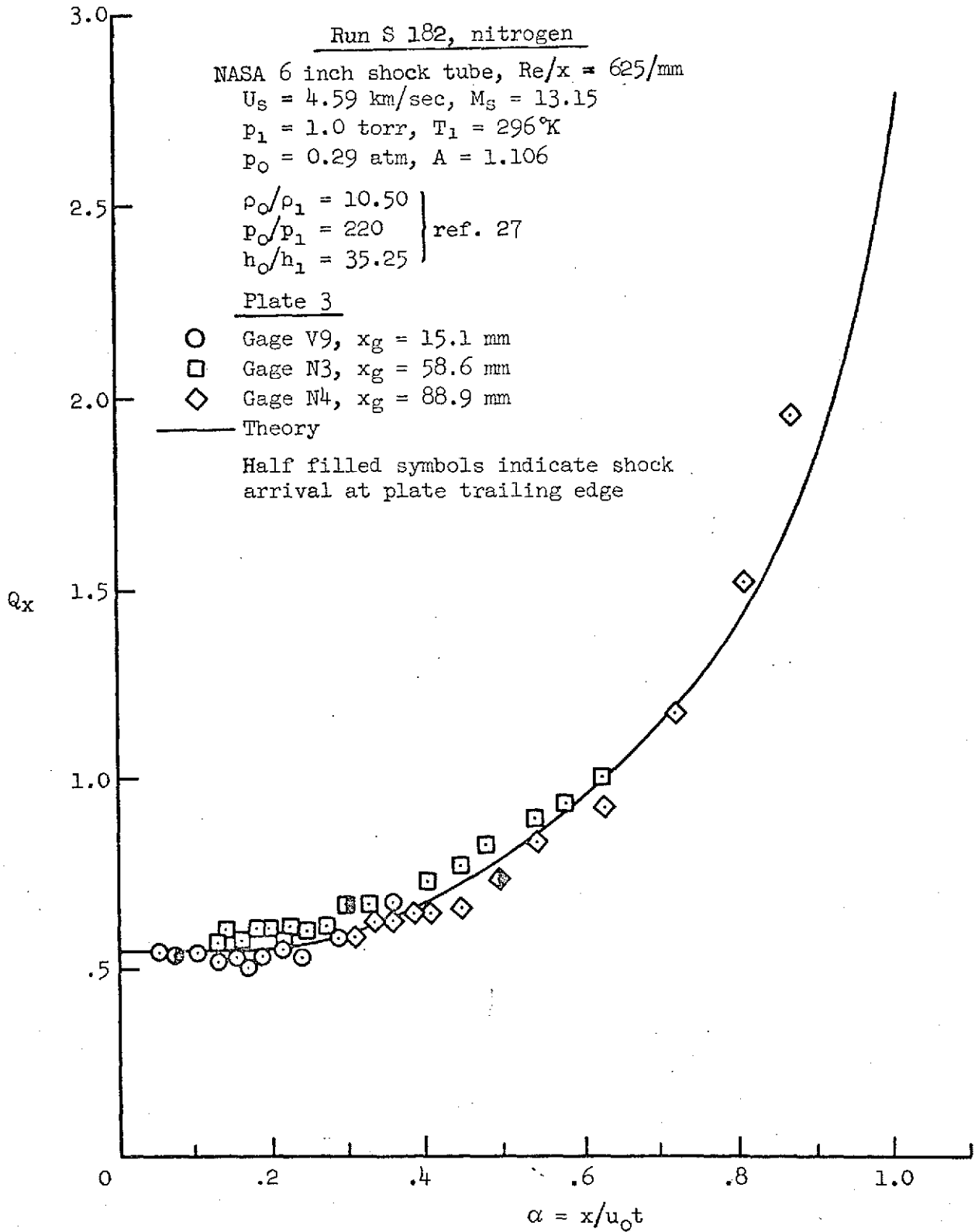
(a) Comparison of theoretical and experimental heat transfer results.

Figure 28.– Data for $U_S = 4.59 \text{ km/sec}$.
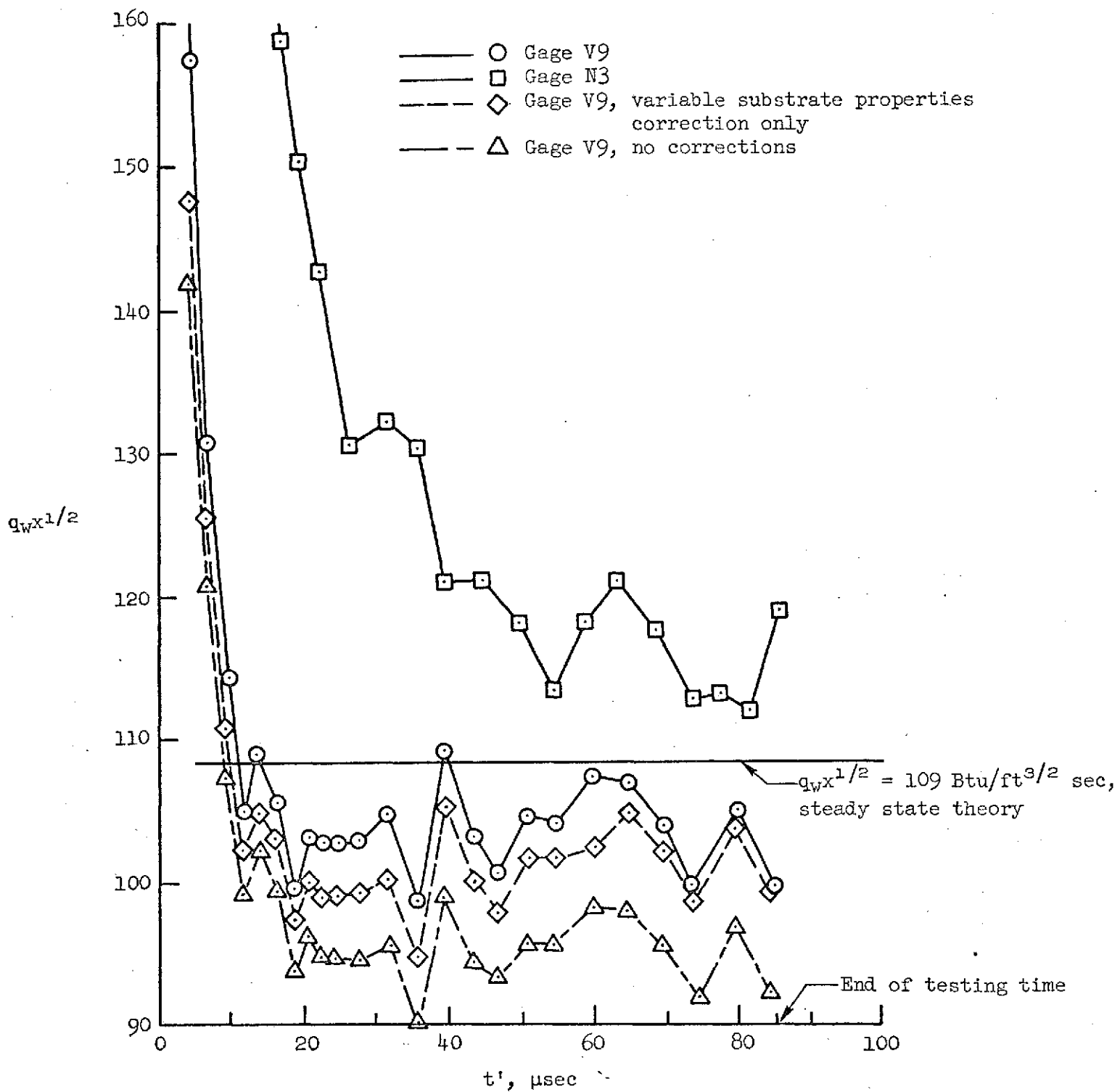
(b) Comparison of $q_w x^{1/2}$ values.

Figure 28.- Concluded.
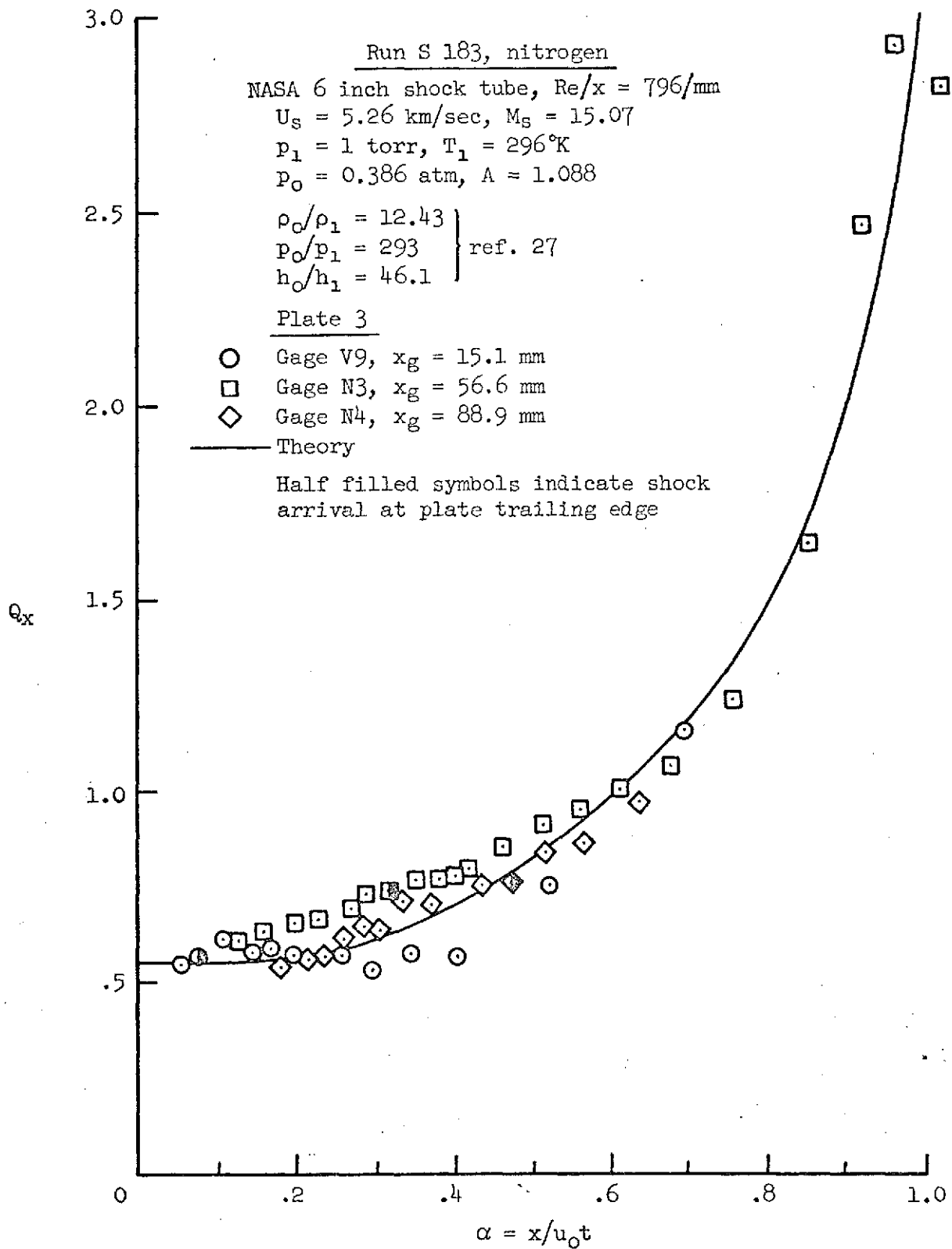
Figure 29.- Comparison of theoretical and experimental heat transfer results, U_S = 5.26 km/sec.

Run S 184, nitrogen

NASA 6 inch shock tube, $Re/x = 929/mm$
$U_S = 5.81$ km/sec, $M_S = 16.65$
$p_1 = 1.0$ torr, $T_1 = 296°K$
$p_0 = 0.473$ atm, $A = 1.080$

$\left.\begin{array}{l} \rho_0/\rho_1 = 13.54 \\ p_0/p_1 = 360 \\ h_0/h_1 = 56.1 \end{array}\right\}$ ref. 27

Plate 3

○ Gage V9, $x_g = 15.1$ mm
□ Gage N3, $x_g = 58.6$ mm
◇ Gage N4, $x_g = 88.9$ mm
── Theory

Half filled symbols indicate shock
arrival at plate trailing edge

$\alpha = x/u_0 t$
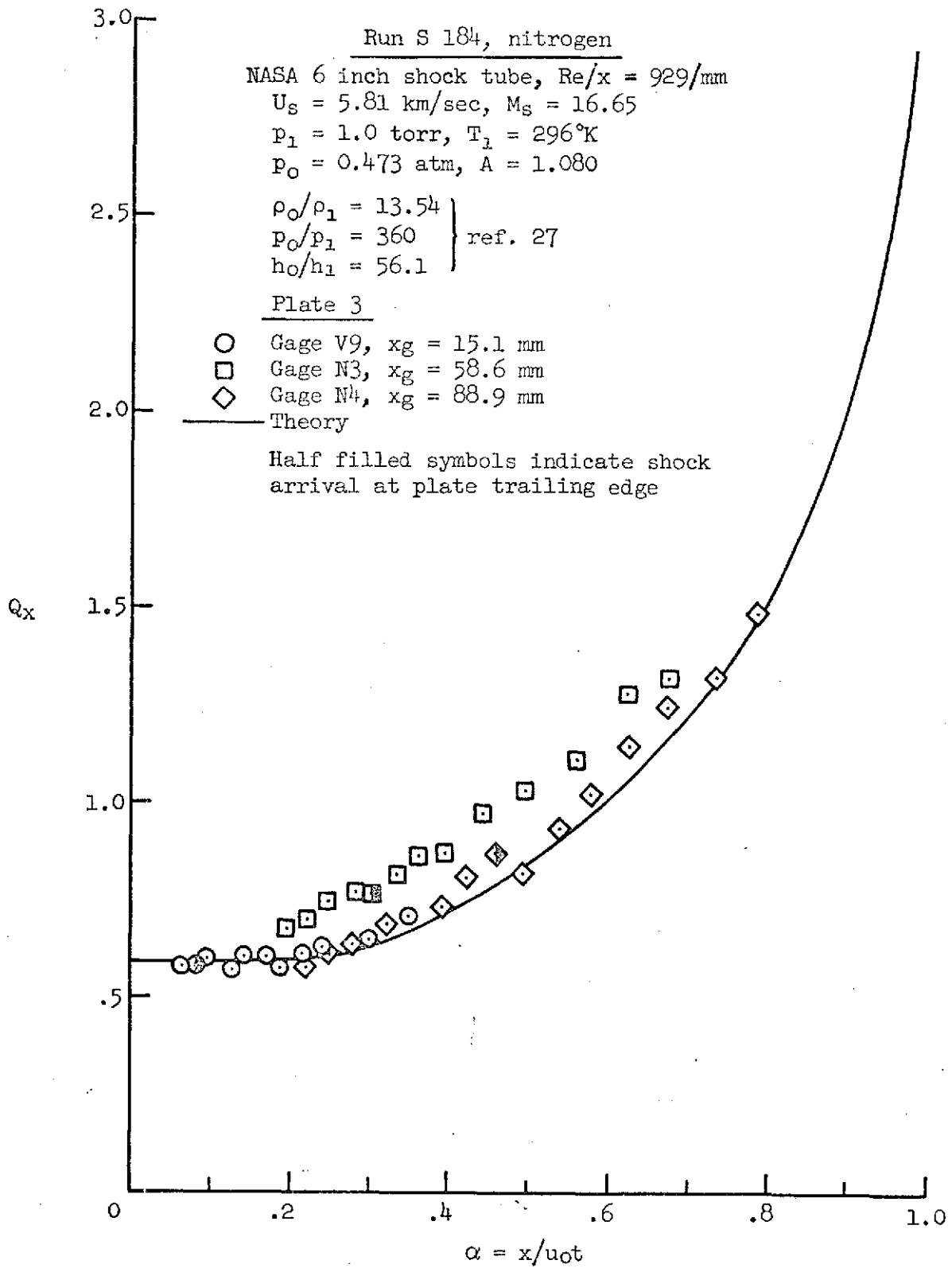
(a) $U_S = 5.81$ km/sec

Figure 30.- Comparison of theoretical and experimental heat transfer results.

Run S 185, nitrogen

NASA 6 inch shock tube, $Re/x = 493/mm$
$U_S = 5.86$ km/sec, $M_S = 16.79$
$p_1 = 0.5$ torr, $T_1 = 296°K$
$p_0 = 0.241$ atm, $A = 1.080$

$\left.\begin{array}{l} \rho_0/\rho_1 = 13.66 \\ p_0/p_1 = 366 \\ h_0/h_1 = 57.1 \end{array}\right\}$ ref. 27

Plate 3

□ Gage N3, $x_g = 58.6$ mm
◇ Gage N4, $x_g = 88.9$ mm
── Theory

Half filled symbols indicate shock
arrival at plate trailing edge
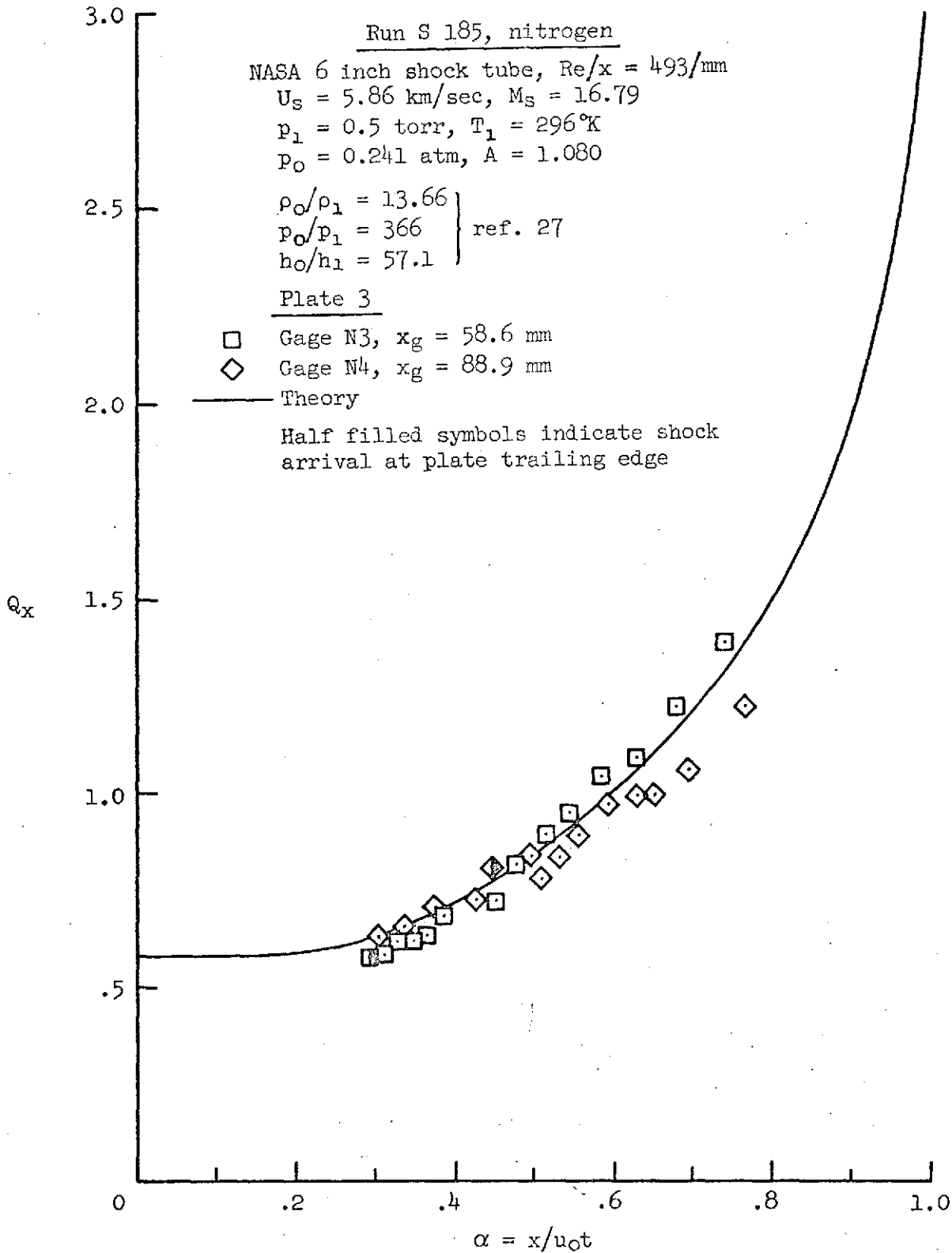
(b) $U_S = 5.86$ km/sec

Figure 30.- Concluded.

Run S 188, nitrogen

NASA 6 inch shock tube, $Re/x = 552/mm$
$U_S = 6.04$ km/sec, $M_S = 17.31$
$p_1 = 0.5$ torr, $T_1 = 296°K$
$p_o = 0.26$ atm, $A = 1.078$

$\left.\begin{array}{l} \rho_o/\rho_1 = 13.8 \\ p_o/p_1 = 395 \\ h_o/h_1 = 60.7 \end{array}\right\}$ ref. 27

Plate 3

○ Gage V9, $x_g = 15.1$ mm
□ Gage N3, $x_g = 58.6$ mm
◇ Gage N4, $x_g = 88.9$ mm
—— Theory

Half filled symbols indicate shock
arrival at plate trailing edge
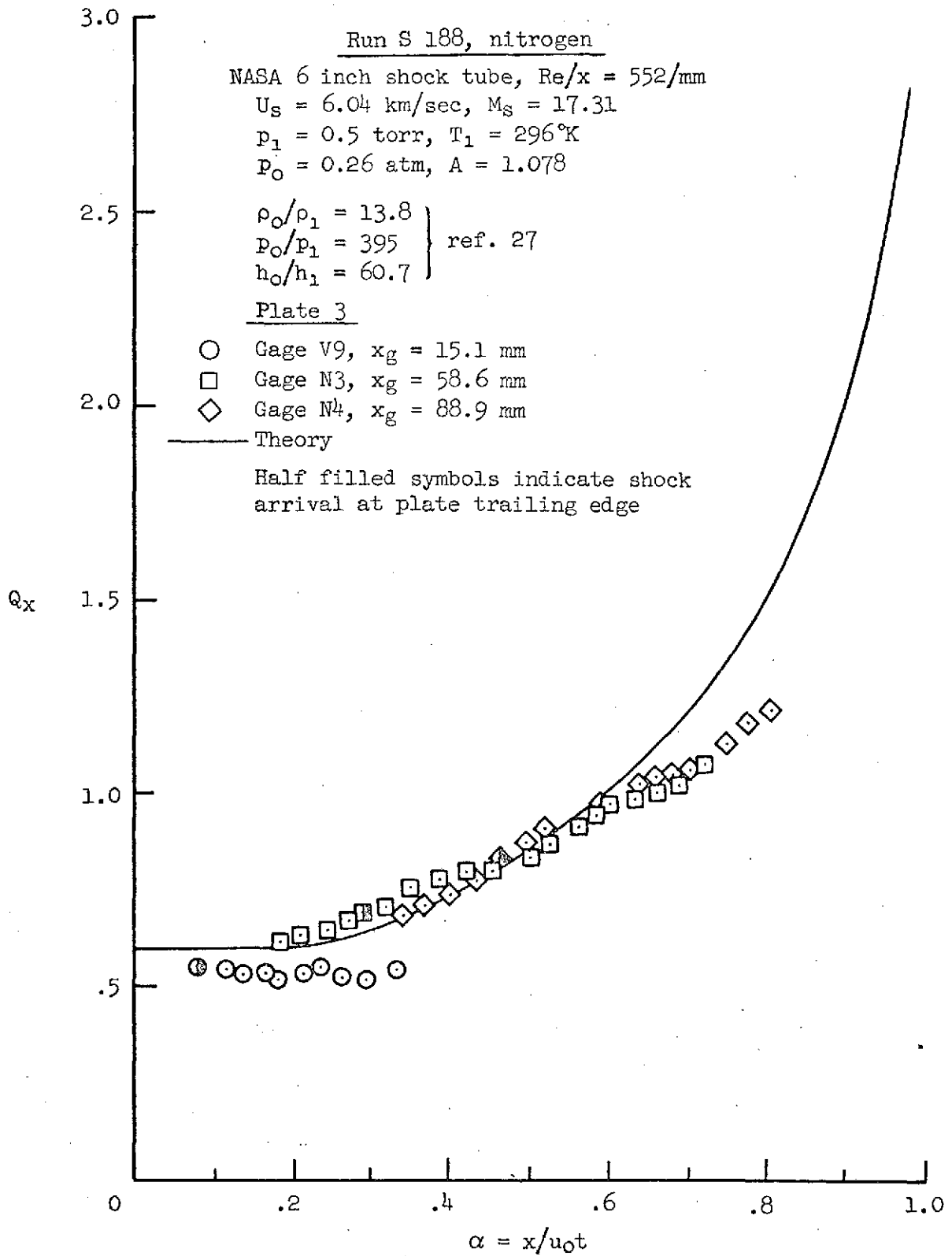
(a) $U_s = 6.04$ km/sec

Figure 31.- Comparison of theoretical and experimental heat transfer results.
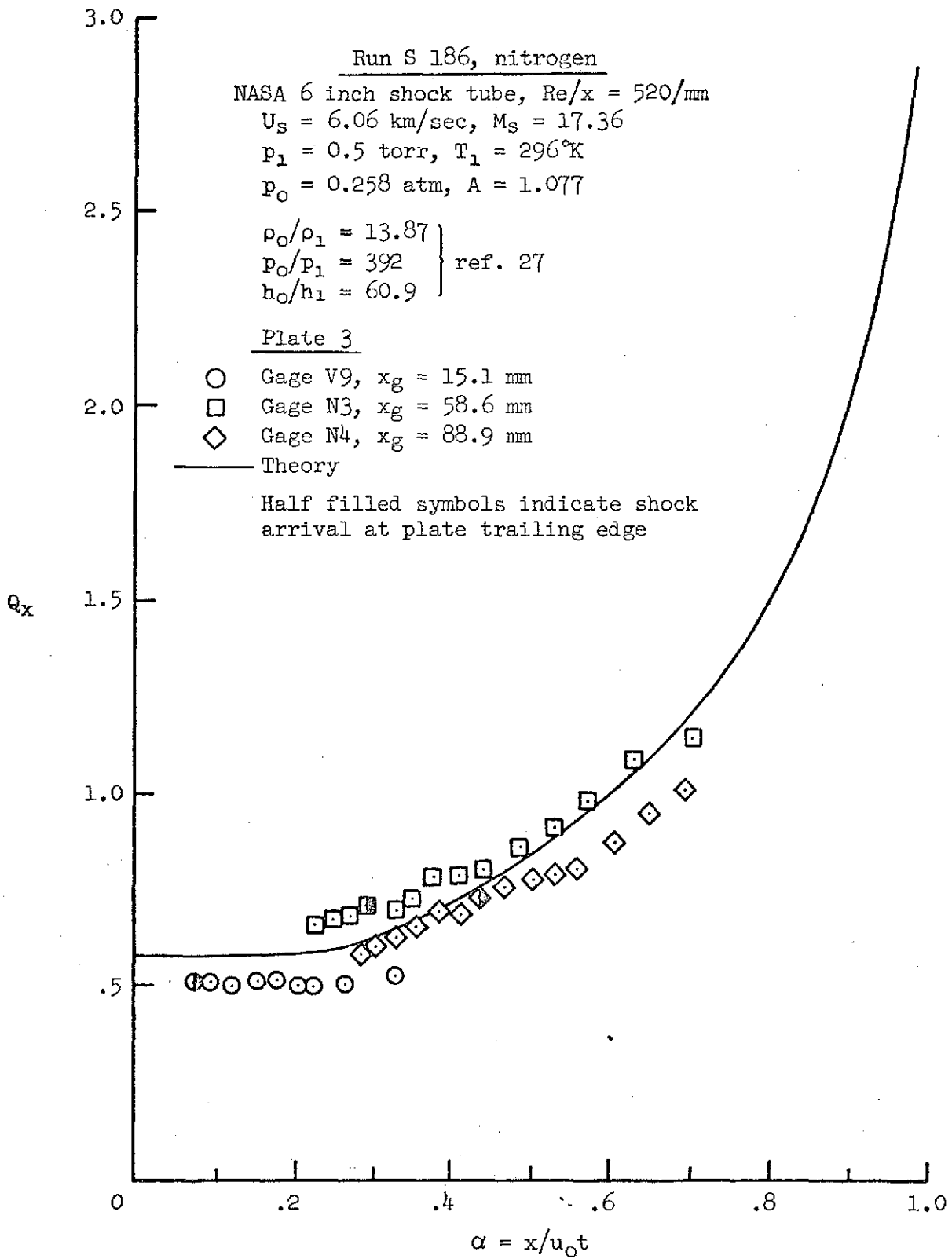
(b) $U_S = 6.06$ km/sec

Figure 31.- Continued.

Run S 175, nitrogen

NASA 6 inch shock tube, $Re/x = 1005/mm$
$U_S = 6.10$ km/sec, $M_S = 17.7$
$p_1 = 1.0$ torr, $T_1 = 296°K$
$p_O = 0.537$ atm, $A = 1.075$

$\left.\begin{array}{l} \rho_O/\rho_1 = 14.3 \\ p_O/p_1 = 409 \\ h_O/h_1 = 63.5 \end{array}\right\}$ ref. 27

Plate 3

◯ Gage M4, $x_g = 14.7$ mm
▢ Gage T3, $x_g = 28.4$ mm
◇ Gage T9, $x_g = 74.5$ mm
——— Theory

Half filled symbols indicate shock
arrival at plate trailing edge

Q_x

$\alpha = x/u_O t$
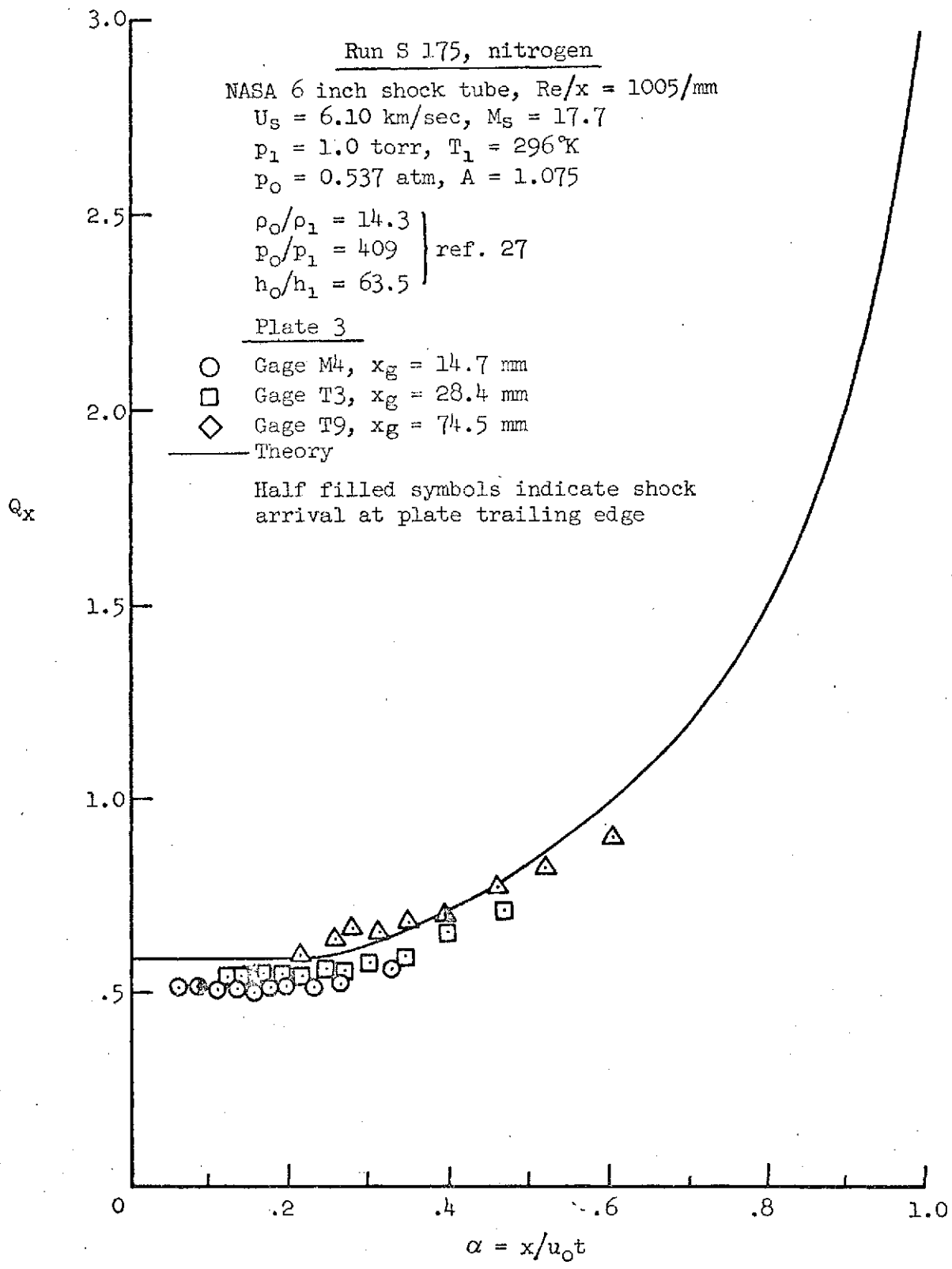
(c) $U_S = 6.10$ km/sec

Figure 31.- Concluded.
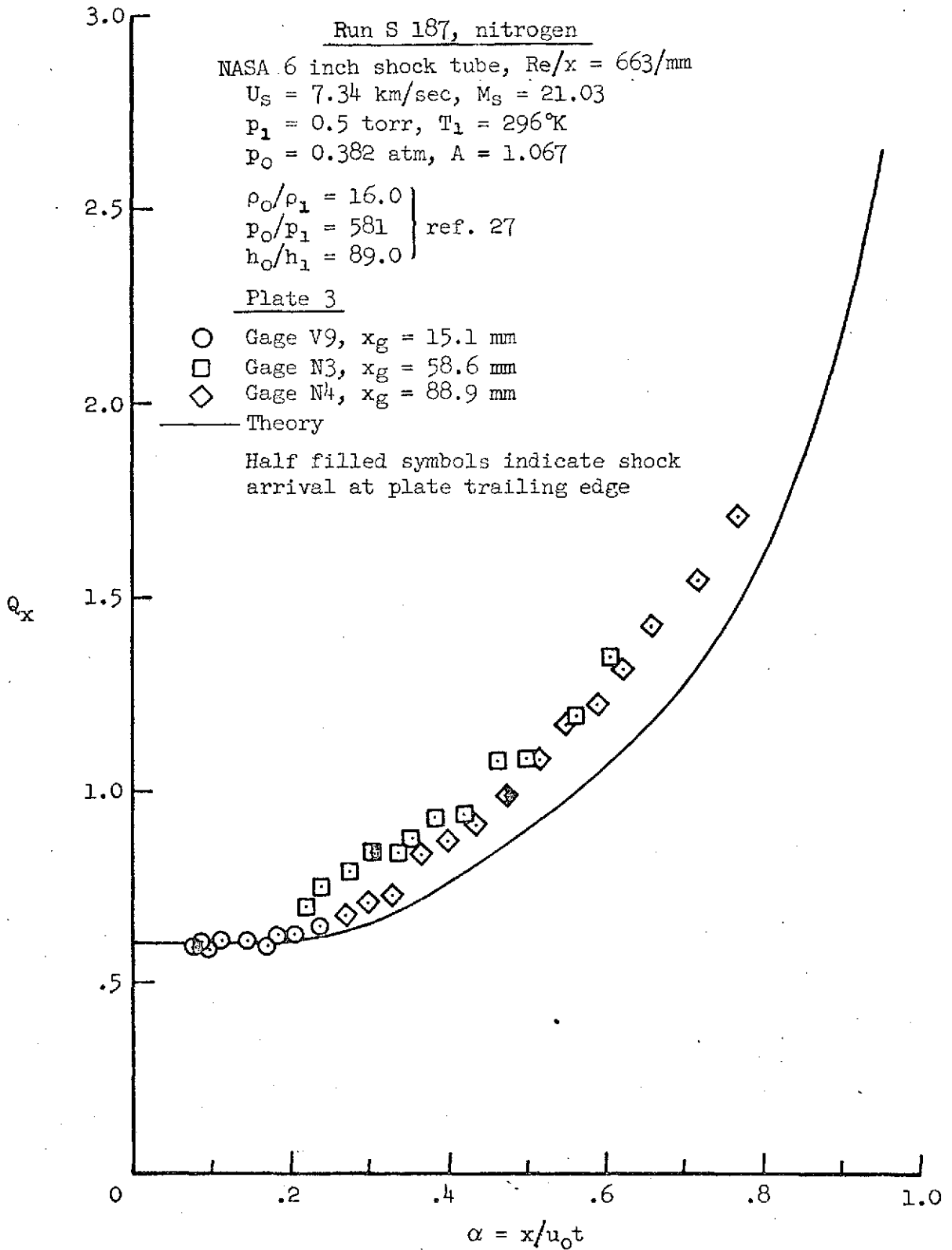
(a) Comparison of theoretical and experimental heat transfer results.

Figure 32.- Data for $U_S = 7.34$ km/sec.
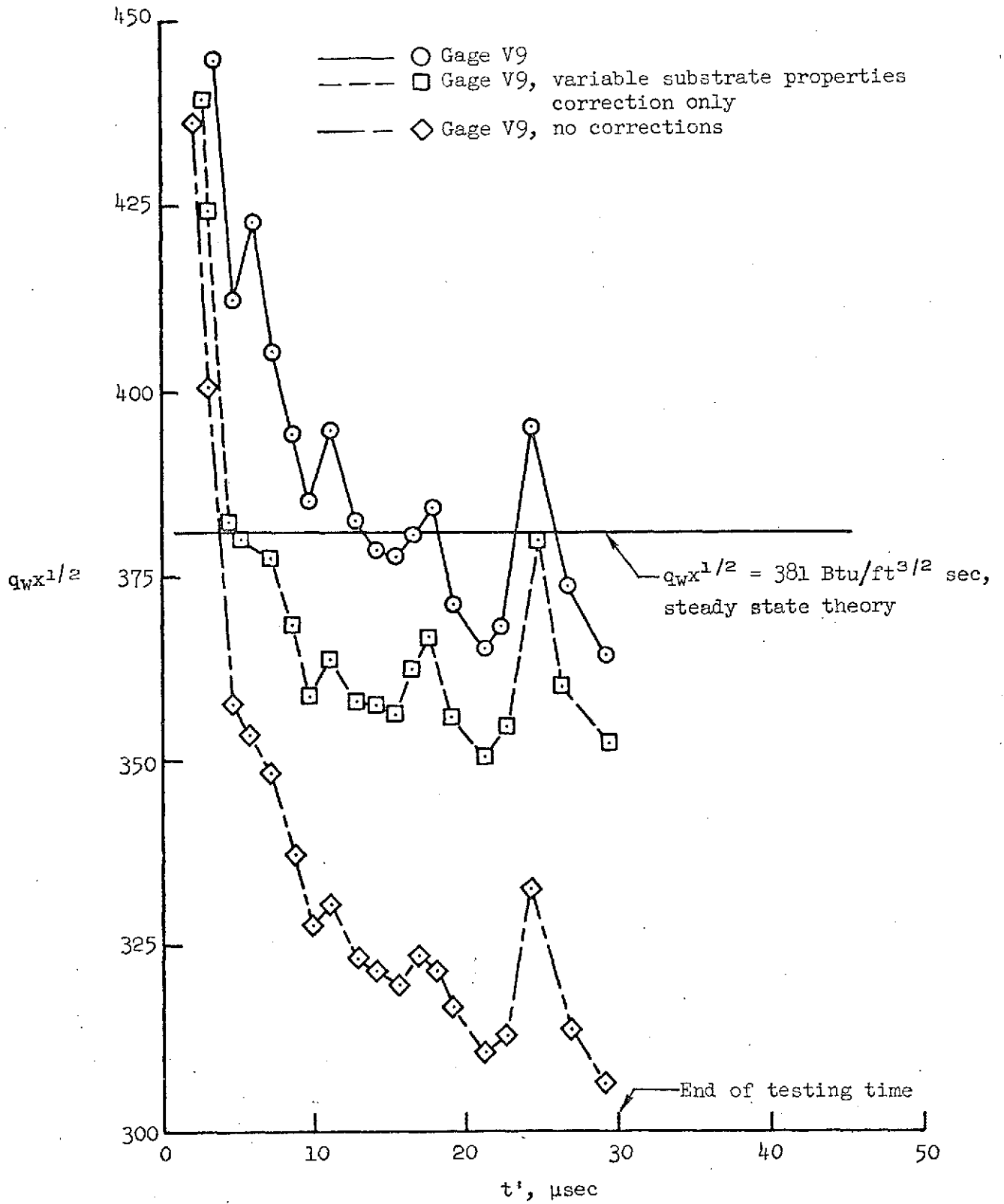
(b) Comparison of $q_w x^{1/2}$ values.

Figure 32.- Concluded.
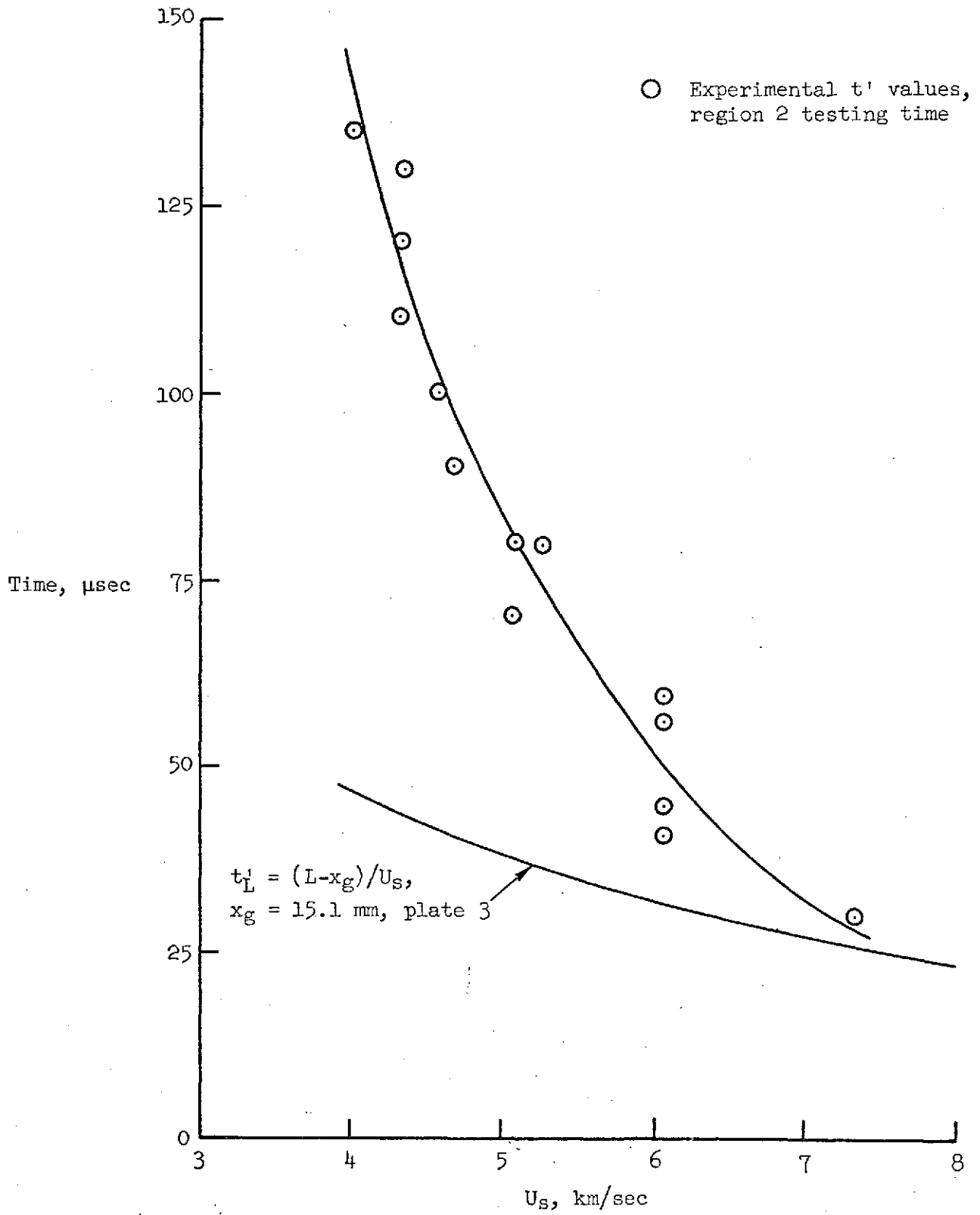
Figure 33.- Comparison of t_L' values and region 2 testing time for plate 3 mounted in the NASA 6 inch arc driven shock tube.
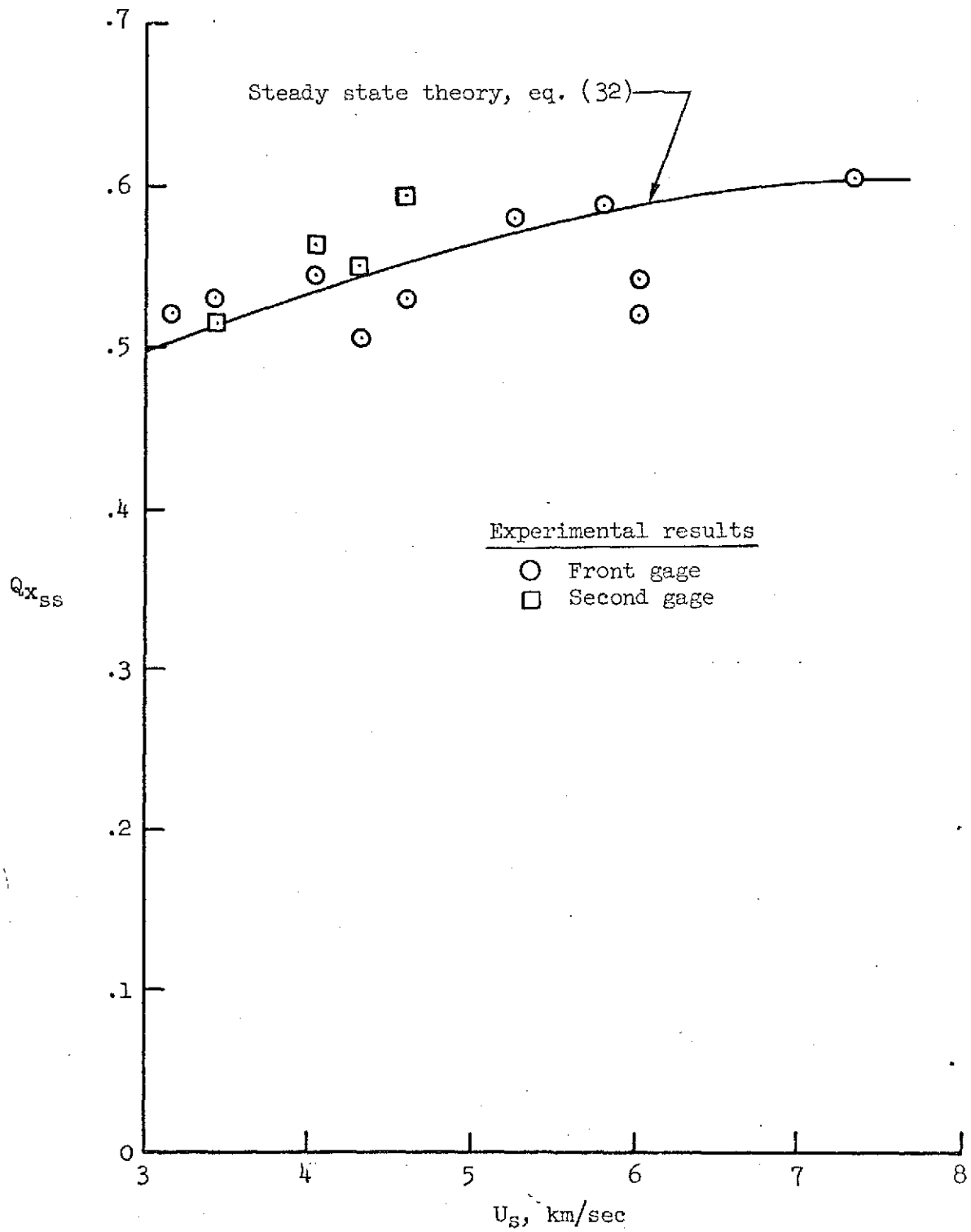
Figure 34.- Comparison of theoretical and experimental steady state heat transfer.